Correlative Pipette Probe Electrochemistry - Electron Microscopy Studies of Platinum Nanoclusters

by

Isabel Mecking Ornelas

A thesis submitted to the University of Birmingham for the degree of

DOCTOR OF PHILOSOPHY

Nanoscale Physics Research Laboratory

School of Physics and Astronomy

University of Birmingham

September 2020

Abstract

This thesis focuses on combining Scanning ElectroChemical Cell Microscopy (SECCM) and aberration-corrected High Angle Annular Dark Field (HAADF) Scanning Transmission Electron Microscopy (STEM) to obtain new insights into the relationship between the structure and electrochemical properties of nanoscale platinum. Carbon-coated Transmission Electron Microscopy (TEM) grids were utilised as substrates for electrochemical experiments, which were performed with SECCM probe tips with diameters of *ca.* 1 μm, forming electrochemical cells with a working electrode areas in the μm^2 scale. The location of the droplet landing areas were identified using *ex situ* STEM, which permitted the visualisation of the whole meniscus-substrate contact area. Micrographs with dimensions of $\approx 10^4$ nm^2 were employed to obtain statistical data about the size and spatial distribution of the Pt NPs, and high magnification images, with subatomic resolution, were utilised to obtain mechanistic information about the studied systems. Two main studies are presented in this thesis. Briefly, the first focuses on the Oxygen Reduction Reaction (ORR), catalysed by mass-selected Pt nanoclusters; the second investigates the nucleation and growth of platinum during electrochemical deposition.

Mass-selected nanoclusters (NCs), with *ca.* 3 nm diameter, were generated in a cluster beam source and deposited onto TEM grid supports, which permitted the preparation of well-defined ensembles of Pt NCs due to the independent control of particle size, density, and impact energy during deposition. These samples were used as model catalyst systems

for ORR, which is vital in energy-related applications, such as fuel cells. The SECCM setup provided a high mass-transport system with a three-phase (gas-liquid-solid) configuration, which mimics fuel cell conditions. Voltammetric studies revealed a loss of electrocatalytic activity with time which was more pronounced when Pt loading was low. Analysis of the samples utilising STEM and X-ray photoelectron spectroscopy (XPS) provided strong evidence that the degradation of the activity of the Pt catalysts was due to poisoning of the platinum surface by carbon/oxygen-containing species, generated by the reaction of reactive oxygen intermediaries of the ORR with the carbon support. Additionally, it was found that whereas Pt NCs deposited with impact energies of 1.6 eV per atom were stable on the substrate, those deposited at 0.54 eV per atom became mobile as a consequence of the ORR and formed characteristic aggregates containing up to 15 or more clusters, with edge-to-edge nearest neighbour distances of *ca.* 1.5 nm.

The electrochemical deposition of platinum onto carbon-coated TEM grids was investigated employing a high-throughput methodology in which the SECCM probe is sequentially brought into contact with the substrate, and where experimental parameters can be systematically varied with each landing. Here, the nucleation and growth of platinum nanostructures was studied by chronoamperometry in a series of experiments where the deposition time was held constant and the applied potential was decreased from 0 V to −0.9 V *vs.* Pt(II)/Pt(0). It was shown that particle density increases and size dispersion decreases with increasing driving force. Furthermore, it was found that single atoms, small clusters and larger particles coexist, independently of the applied potential, supporting a non-classical nucleation and aggregative growth mechanism, and a correlation was established between a structural transition of clusters at $d \approx 2$ nm from amorphous to monocrystalline, and the critical size at which growth by direct addition is impeded.

Acknowledgements

I thank professor Richard Palmer for the chance to work at NPRL. I am grateful to my supervisor, Dr. Andrey Kaplan, for the support and for help with corrections to my thesis. I also thank Dr. Ziyou Li for helpful discussions about STEM.

A special thank you to professor Pat Unwin of the University of Warwick for the opportunity to collaborate with the WEIG, support, and guidance on all electrochemistry work. I would like to thank Dr. Jon Ustarroz, Dr. Guohui Zhang and Dr. Cameron Bentley, with whom I worked closely to complete the projects presented in this thesis, for the patience, motivation, support and interesting discussions.

I am thankful to my fellow colleagues at NPRL, in particular to Dawn, Caroline and Nan for training me on the cluster source and STEM, to Scott for getting me started with Python, and Patrick for interesting discussions about platinum clusters. *Merci beaucoup* to Tibo for his constant support through all the ups and downs. And thank you the group in general for the sanity-preserving lunch breaks, jam sessions and squash games.

I would also like to thank Dr. Ian Stevens for invaluable support when things got difficult.

Last but not least, a huge thank you to my family and (non-UoB) friends for their encouragement and support, and to Callum, for being wonderful.

Author's Publications

The work described in Chapter 3 has been published in:

Jon Ustarroz, Isabel M. Ornelas, Guohui Zhang, David Perry, Minkyung Kang, Cameron L. Bentley, Marc Walker, and Patrick R. Unwin. "Mobility and Poisoning of Mass-Selected Platinum Nanoclusters during the Oxygen Reduction Reaction." In: *ACS Catalysts* 8.8 (Aug. 3, 2018), pp. 6775-6790. DOI: 10.1021/acscatal.8b00553

The work presented in Chapter 4 has been published in:

Isabel M. Ornelas, Patrick R. Unwin, Cameron L. Bentley. "High-Throughput Correlative Electrochemistry-Microscopy at a Transmission Electron Microscopy (TEM) Grid Electrode". In: *Analytica Chemistry* (Nov. 2019). DOI: 10.1021/acs.analchem.9b0428

The author also contributed during her PhD to the following publications, which are not featured in this thesis:

Jian Liu, Nan Jian, Isabel Ornelas, Alexander J. Pattison, Tanja Lahtinen, Kirsi Salorinne, Hannu Käkkinen, and Richard E. Palmer. "Exploring the atomic structure of 1.8 nm monolayer-protected gold clusters with aberration-corrected STEM". In: *Ultramicroscopy*. 176 (May 1, 2017), pp. 146-150. DOI: 10.1016/j.ultramic.2016.11.021

Andrew McInnes, Simon R. Plant, Isabel Mecking Ornelas, Richard E. Palmer, and K. G. Upul Wijayantha. "Enhanced photoelectrochemical water splitting using oxidised mass-selected Ti nanoclusters on metal oxide photoelectrodes". In: *Sustainable Energy & Fuels* 1.2 (2017), pp. 336-344. DOI: 10.1039/C6SE00050A

Y. Xia, P. Harrison, I. M. Ornelas, H. L. Wang, and Z.Y. Li, "Effects of defocus and magnification on HAADF intensity of nanoclusters in STEM images". Submitted for publication.

Table of contents

List of figures

List of tables

Symbols and Abbreviations

ADF	Annular Dark Field
BF	Bright Field
CA	Chronoamperometry / Chronoamperogram
CCTG	Carbon-Covered TEM Grid
CV	Cyclic Voltammetry / Cyclic Voltammogram
Dh	Decahedron / Decasahedral
DPSC	Double Potential Step Chronoamperometry
ECSA	Electrochemically Active Surface Area
FC	Fuel Cell
FCC	Face-Centred Cubic
FEG	Field-Emission Gun
FEM	Finite Element Method
FWHM	Full Width Half Maximum
GC	Glassy Carbon
HAADF	High-Angle Annular Dark-Field
HV	High Vacuum
Ih	Icosahedron / Icosahedral

IPD	InterParticle Distance
LSV	Linear Sweep Voltammetry / Voltammogram
LTOF	Lateral Time of Flight
MA	Mass Activity
N&G	Nucleation and Growth
NND	Nearest Neighbour Distance
Oh	Octahedron / Octahedral
ORR	Oxygen Reduction Reaction
SA	Specific Activity
SECCM	Scanning ElectroChemical Cell Microscopy
SHE	Standard Hydrogen Electrode
SPM	Scanning Probe Microscopy
STEM	Scanning Transmission Electron Microscope / Microscopy
UHV	Ultra-High Vacuum
XPS	X-ray Photoelectron Spectroscopy

Chapter 1

Introduction and Literature Review

1.1 Overview

The work presented in this thesis focuses on the electrochemistry of platinum at the nanoscale, and how scanning electrochemical cell microscopy (SECCM) and high angle annular dark field (HAADF) scanning transmission electron microscopy (STEM) can be combined to provide new information about the nano and atomic scale processes that take place in nanocluster systems. SECCM permits the study of the electrochemical properties of a relatively small number of particles, and STEM can provide high resolution images of a large portion of the studied population. By combining these techniques, correlations between the electrochemical results and particle morphology, size and spatial distributions can be established. Additional insights can be gained by complementary techniques, such as X-ray photoelectron spectroscopy.

This chapter provides a background to the topics that are relevant to this thesis. The material covers the importance of platinum and nanoscale materials, focusing on nanoscale platinum, its role as an electrocatalyst and the structure of Pt nanoclusters (section 1.2).

The development of nucleation and growth theories for the electrodeposition of metals onto low energy substrates is explored, and a summary of recent studies, which challenge the traditional models, is provided in section 1.3.

Platinum is a rare noble metal which has applications in several fields and industries due to its qualities, including high resistance to corrosion, high melting temperature, durability, and catalytic properties (*vide* section 1.2.1). As a catalyst, it plays an especially important role in energy conversion and related technologies, e.g. it is commercially employed in anodes and cathodes in fuel cells (FCs), and a significant portion of the annual platinum consumption (≈40% globally and 70% in Europe) goes into autocatalysts. As a catalyst, platinum is most often employed as highly dispersed nanoparticles on high surface area carbon supports.

Nanoscale materials, usually defined as having dimensions <1 μm, are of great interest due to their unique properties, which differ from those of their constituent atoms or molecules and from bulk materials and can be highly dependent on the material's structure, size and composition (see section 1.2.2). Our understanding of the properties of such materials grows as new technology is developed, allowing the generation, control and investigation of systems and processes at decreasing scales. A better knowledge of the relationships between the characteristics of NPs and their properties can lead to the development of novel materials with higher efficiencies and lower costs.

Studies about the structure of small Pt clusters are explored in section 1.2.3, and the electrocatalytic properties of such particles are introduced in section 1.2.4.

Platinum is the most efficient catalyst material for the oxygen reduction reaction (ORR). This reaction is especially relevant for fuels cells (cathodic reaction), which convert chemical into electrical energy, and Pt is employed in cathodes of such devices in the form of highly dispersed NPs on high surface area supports. Section 1.2.5 sumarises works which have

demonstrated that the size, structure and particle density of Pt nanocatalysts, as well as the nature of the support, can affect the overall performance and selectivity of a catalytic system, and highlights contradictory findings.

Electrodeposition is a technique in which metallic ions are reduced and deposited at an electrode's surface. The potentiostatic electrodeposition of metals is explored in section 1.3, starting with the classical nucleation and growth (N&G) models (section 1.3.1). Recently, through the combination of electron microscopy and electrodeposition studies, significant discrepancies have been revealed between predicted parameters (nucleation density and particle size) and experimental results. These studies, and new proposed mechanisms to exaplain them, are discussed in section 1.3.2.

1.2 Nanoscale Platinum

1.2.1 Importance of Pt

Platinum is a vital raw material in today's economy. It is a very scarce element (approximately $0.5\,\mathrm{ng\,g^{-1}}$ in the upper continental crust[1]), whose main supplies come from South Africa (73% of all primary supplies in 2018).[2] The total platinum deposits are estimated to be about 66 000 t,[3] and resource depletion is not currently considered a danger; however, social, economical and environmental issues put this metal at critical supply risk.[4] Globally, the annual gross demand for platinum is of about 250 tonnes, a significant portion of which is used in various technology-related industries.[2] Due to its high cost, there is a strong motivation to recover this metal. However, some loss is unavoidable, and currently, only $\approx 25\%$ of the total world's Pt supply is from secondary sources (figure 1.1**(B)**), such as recycled or recovered end-of-life industrial products including catalysts (especially auto-catalysts), electrode assemblies and electronic equipment.[3]

Figure 1.1(A) shows the evolution of platinum demand in the last 5 years, globally and in Europe, and how the demand for platinum is distributed into three broad categories: auto-catalysts ("A-cat.", blue), other industrial use ("Ind.", green), and jewellery and investment ("J&I", red). The automotive sector is the biggest single consumer of this metal, at 35 to 40% of global platinum use. It is clear, from the data presented in figure 1.1(A), that this demand is being driven by Europe, which is responsible for 48% of total platinum catalysts for automotive converters. However, legislative changes are predicted for China and India, and an increase in demand for the metal is expected as a consequence.[2]

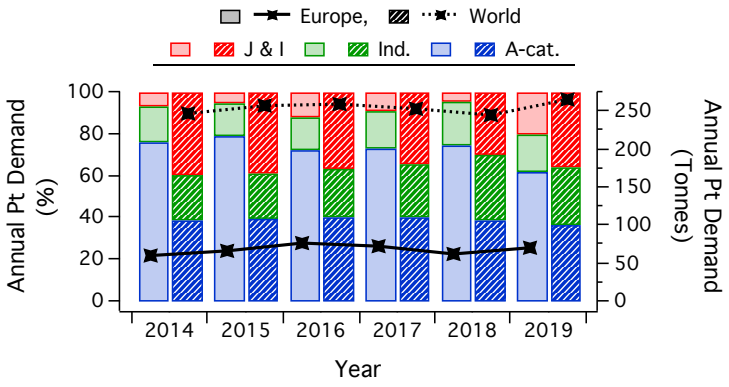

(A) Annual Pt demand by sector (Europe *vs.* world).

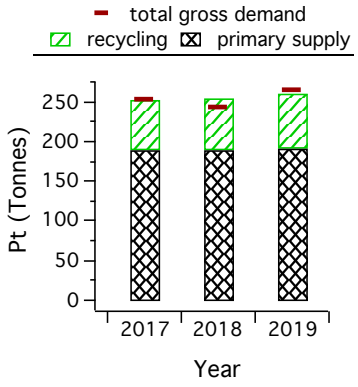

(B) Annual global Pt supply and demand.

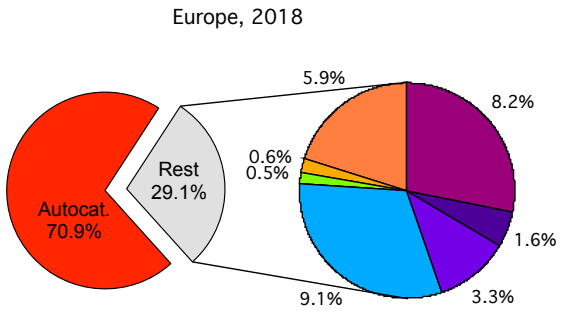

(C) Annual Pt usage by sector in Europe, 2018.

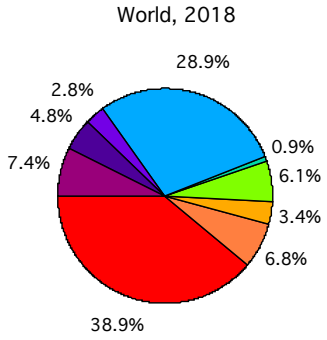

(D) Annual global Pt usage by sector, 2018.

(E) Legend.

FIGURE 1.1: Annual platinum usage in Europe and the world. Data obtained from [2].

New, green technologies and energy-related industries are especially heavily dependent on platinum. For example, it is vital in catalysts that reduce air pollution (autocatalysts),

which convert harmful exhaust gases, such as carbon monoxide (CO), hydrocarbons and nitrogen oxides (NOx) into CO_2, N_2 and H_2O.[5, 6]. In fuel cells (FCs), which convert chemical into electrical energy, platinum is still the most efficient electrocatalyst material for the reduction reaction (usually oxygen reduction), which is the rate-limiting step in these devices. Overall, this noble metal is indispensable in several industries, including chemical, electrical*, glass, (bio)medical, and petroleum. Especially valuable properties include its inertness / resistance to corrosion, biocompatibility, high melting point (1768.3 °C), good performance as an (electro)catalyst and good conductivity. Figures 1.1(C) and 1.1(D) show the detailed breakdown of platinum use by sector for Europe and the world, respectively.

Although strategies are being actively pursued to minimise current technologies' dependence on platinum due to its high cost and scarcity, forecasts predict the demand for this element to rise in the near future. Understanding the mechanisms that underlie platinum's properties, especially as a catalyst and electrocatalyst, is one of the key ways to develop better alternatives, that will either make platinum more efficient (per unit mass), or that will allow the discovery of different materials that can match or even surpass platinum.

1.2.2 Nanoscale materials

Nanoscale materials are customarily defined as having dimensions between one and hundreds of nanometers. In this thesis, the term nanoparticle (NP) is used generally to describe particles in this size range, whereas the term nanocluster (NC, or simply cluster) refers to species having just up to a few nanometers, or up to approximately 10^6 constituent atoms.

The scientific study of nanoparticles only began in 1857, when Michael Faraday first identified that suspensions of "metallic gold in a state of extreme division" produced fluids

*mainly in hard disk drives (HDDs)

of different colours, depending on the size of the gold particles.[7] Since then, "nano" has become indispensable to modern technology and much has been learned about the peculiar properties of nanoscale and nanostructured materials, which differ from both those of the same material in bulk and from those of their constituent atoms or molecules. At this scale, both size (number of atoms) and structure can affect the physical and chemical properties of materials due to the quantum confinement of electrons and to the high surface area to volume ratio in these species.[8–10] This variation as a function of size can happen smoothly or discontinuously, depending on the property and size regime. Properties that have been shown to be size-dependent at the nanoscale include: interatomic bond distances,[11, 12] melting point,[13–15] optical and electronic properties[7, 12, 16], and reactivity.[17–20]

For example, it has been shown that for large metal NPs, assuming a spherical shape (with radius R), several properties, including melting temperature (T_m), chemical reactivity, absorption frequency and electrical conductivity, generally vary with $1/R$, or $N^{-1/3}$ (where N is the number of constituent atoms).[10, 14] This relation arises from the dependence of these properties on the ratio of surface area to volume.

At the smaller end of the nanoscale, a particle's properties become even more strongly dependent on the number of constituent atoms and this law breaks down, often resulting in oscillations about the smooth trend.[10] In this size range, the closing of electronic and geometric shells becomes increasingly important, influencing also the material's structure, interatomic bond distances and structural stability.[21] For the smallest clusters, electronic shell closure (e.g. having 2, 8, 18, 34, 58, 92... shared electrons[8, 22]) contributes most strongly to the species stability. As the NC's size increases, the spacing between its electronic orbitals decreases and geometry becomes a more important factor.[23, 24] The number of atoms necessary for closing electronic or geometric shells are usually termed "magic numbers".

Due to their tunability of behaviour and versatility, nanoscale materials already are employed in many technologies, including in fields such as optics,[25] energy,[26] biology/medicine (therapy and diagnostics)[27–29] and catalysis.[30, 31] For example, most industrial heterogeneous catalysts employ NPs in the size range between 1 and 20 nm dispersed on high surface area solids.[30] Improving the performance of nanoparticles in such applications can not only make such products more efficient, it can help in the development of new technologies.

1.2.3 Structure of Pt Nanoclusters

For clusters with well-defined structures, three structural motifs are generally distinguished: icosahedral (Ih), decahedral (Dh) and octahedral (Oh). As the names imply, icosahedra, decahedra and octahedra are based on geometric shapes possessing 20, 10 and 8 facets, respectively. However, structures of all three motifs include variations on the geometrical shape after which they are named. For example, Oh and Dh can be truncated to obtain lower surface to volume ratios.

The octahedral motif is the only of these three with a crystalline structure. Oh are composed by two square pyramids which share a basis, and have a face-centred cubic (FCC) structure. The resulting facets are closed packed (111), however, this structure has a very high surface to volume ratio. Truncated octahedra can be generated by "cutting" the vertices so that the resulting structure has eight close packed (111) and six square (100) facets. This results in a more spherical shape, with lower surface to volume ratio but higher surface energy due to the (100) facets.[9]

Icosahedra and decahedra are non-crystalline structures with 5-fold symmetries. They are closer to a sphere in shape (the Ih more so than the Dh) and are delimited by close-packed facets but have very high internal strains.[9]

Generally, icosahedral motifs tend to be favoured at the smallest sizes, FCC structures (i.e. truncated octahedra) at large sizes, and decahedral motifs in the intermediate range. The exact size at which these transitions (Ih $\rightarrow$ Dh and Dh $\rightarrow$ FCC) occur depend on the material.[9] It is worth noting that clusters are metastable and that a NC may become trapped at a higher energy structure due to growth effects or kinetic trapping.[32]

Experimental studies about the morphology of Pt NCs are rare, and theoretical calculations tend to focus on small sizes ($N \leq 60$).[32] However, theoretical studies report a dominance for FCC structures, even at the small sizes that were studied. [32, 33]

Lambie *et al.*[32] combined experimental and theoretical studies to investigate the structure of Pt clusters with up to 600 constituent atoms. Mass-selected clusters, ranging in size from 10 to 600 atoms, were generated in the cluster source at NPRL and soft-landed (at *ca.* 1 eV per atom) onto TEM grids. The structures of these clusters were categorised, for each size, into one of the three motifs described above (Ih, Dh and FCC) or as unidentified/amorphous (UI/A). Figure 1.2 summarises their findings, and shows that, for clusters with $N \lessapprox 200$ atoms, the majority does not have a recognisable structure or is amorphous. The percentage of FCC clusters rises steadily from $N = 200$ to 300, and for larger NCs, $\approx$2/3 of the population could be identified as FCC. A small portion of clusters with more than 200 constituent atoms revealed Dh motifs, but no Ih were observed.

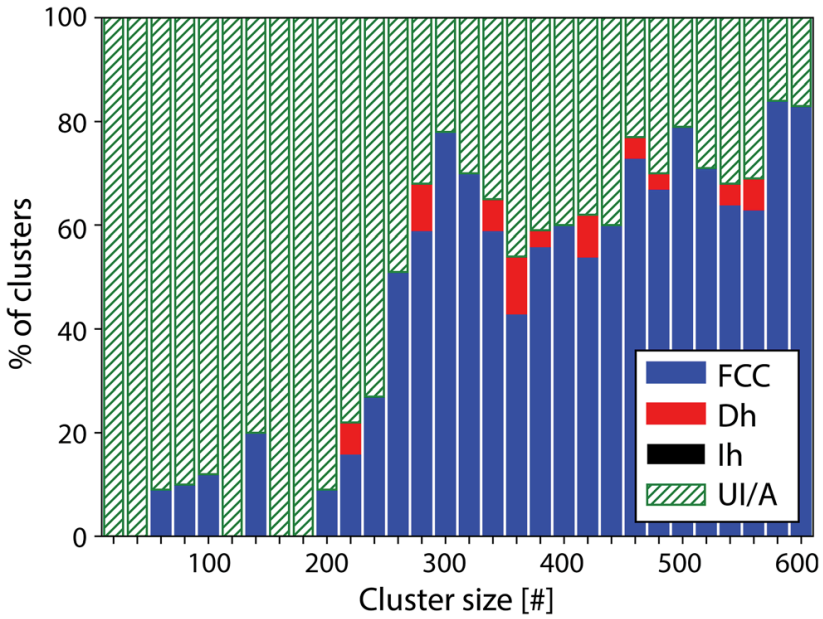

FIGURE 1.2: Overview of the size-dependent motif populations for platinum clusters with 10 to 600 constituent atoms. Four groups were distinguished based on structural motifs: FCC (blue), decahedral, Dh (red), icosahedral, Ih (black), or unidentified/amorphous (UI/A, green). Sample size: 700 clusters. Image taken from [32].

The magic numbers for truncated octahedral structures are given by the expression:

$$N = \frac{2n_l^3 + n_l}{3} - 2n_{cut}^3 - 3n_{cut}^2 - n_{cut} \tag{1.1}$$

where n_l = is the length of the edges of the complete octahedron and n_{cut} is the number of layers cut at each vertex.[9] Cuboctahedra are a specific case of truncated octahedra where $n_l = 2n_{cut} + 1$ and the hexagonal facets degenerate to triangles. This structure has large (100) facets.[9]

According to equation 1.1, the magic numbers for cuboctahedral clusters are 13, 55, 147, 309, 561, 923, 1415, 2057... The same number of atoms is necessary to close the shells for icosahedra and Ino-decahedra.[9]

1.2.4 Nano-structured Pt as an electrocatalyst

Nanoparticles possess several characteristics that make them desirable as (electro)catalysts, such as their high surface area to volume ratio, the high proportion of active undercoordinated sites (e.g. corners and edges), the tunability of their properties by changing their composition, size and structure, and the decreased amounts of material needed for comparable performance.

Three parameters relating to activity are especially important to consider when assessing a catalyst's efficiency: **i)** the mass activity (MA), which is defined as the catalytic current per unit mass of catalyst material (i.e. Pt in this case), usually in $\mathrm{A\,g_{Pt}^{-1}}$, **ii)** the electrochemically active surface area (ECSA) per unit mass of the catalyst (in $\mathrm{m_{Pt}^2\,g_{Pt}^{-1}}$), **iii)** and the specific activity (SA), the electrocatalytic current normalised by ECSA (in $\mathrm{A\,cm_{Pt}^{-2}}$).[34–36]

Platinum-based materials are highly efficient and stable electrocatalysts for several energy-related reactions, especially those occuring in fuel cells, including the oxygen reduction reaction (ORR), hydrogen oxidation reaction (HOR), and the oxidation of small organic molecules (e.g. methanol, ethanol, formic acid).[34, 37] For this reason, Pt is employed commercially as the catalyst in direct methanol fuel cell [37, 38] and hydrogen-fed fuel cell anodes, as well as in the cathodes of polymer electrolyte (proton exchence) membrane fuel cells.[39]

Strategies are being sought to improve the performance of catalysts and decrease their cost. For platinum in particular, there are two main objectives: **i)** to increase the resistance of the catalyst to poisoning (especially CO poisoning)[38, 40], and **ii)** to decrease the amount of platinum used, in order to decrease the final price of the device.

1.2.5 ORR activity, particle size, and interparticle distance

This section will focus on Pt as a catalyst for the ORR, giving a brief overview of the ORR reaction mechanism and a summary of the main findings addressing the relationship between Pt catalyst size, structure and interparticle distance, and catalytic activity, as well as discrepancies and challenges in such studies and results.

The overall reaction for the reduction of oxygen is as follows:

$$O_2 + 4H^+ + 4e^- \longrightarrow 2H_2O \qquad (E^0 = 1.23\,V) \tag{1.2}$$

It can occur in acidic, neutral or basic solution, and depending on the system (catalyst, overpotential, etc.), the reaction pathway can be direct (1-step, 4-electron reaction; equation 1.2), or in two steps, via the production of oxygen peroxide:

$$O_2 + 2H^+ + 2e^- \longrightarrow H_2O_2 \qquad (E^0 = 0.70\,V) \tag{1.3}$$

$$H_2O_2 + 2H^+ + 2e^- \longrightarrow 2H_2O \qquad (E^0 = 1.78\,V) \tag{1.4}$$

Generally, the first, 1-step pathway is preferred for energy-related applications.

Platinum catalysts can promote either of these mechanisms depending on their structure and loading.[35, 36, 41]

In fuel cells, the efficiency of the cathodic catalyst is especially important due to the sluggish kinetics of the ORR, which results in a high overpotential (*ca.* $0.3 - 0.4\,V$), limits the device's performance and brings up its cost because of the need for higher amounts of catalyst material (usually platinum).[42–45] Another challenge for Pt catalysts in FCs is poisoning, usually by CO.[37]

It is known that size, shape and morphology of nanostructured platinum affect its electro-catalytc efficiency strongly. [46–54]

The effect of the particle size on the catalytic activity has been the subject of many studies over the past decades. However, discrepancies have been reported between different studies, and the relationship between size, structure and activity is still under debate. Difficulties in understanding which factors affect catalyst NPs' performance arise from the the variety of relevant parameters which cannot be fully controlled independently or easily isolated. Such factors include particle size, morphology, the substrate, density, and interparticle distance. For example, in many studies, when particle size is varied, so are the total catalyst loading and interparticle distances (*vide infra*). Differences in experimental methodology and techniques used to study and characterise the catalyst systems can also influence the experimental outcomes and resulting conclusions.

Maxima in the mass activity, MA, have been found for specific particle sizes (or size ranges) by some groups for small NP sizes (3 - 5 nm). [46–48, 52, 53] This effect was explained by Kinoshita[49] as being directly related to the NP structures at different sizes and the resulting "types" of surface atoms. The author considered the effect of the Pt-NP structure at small sizes, especially the ratios of (111) and (100) plane atoms, corner and edge atoms on the NPs' mass and specific activities, assuming face-centred cubic structures and cuboctahedral morphologies at all investigated sizes. The results of Kinoshita's simulations showed a non-linear increase of specific activity with increasing size (the curve's slope decreased with increasing size in the studied range of up to 15 nm), and a maximum in mass activity for particles with diameters of ≈ 3.5 nm - the author attributed this effect to "the maximum in the surface fraction of Pt atoms on the (100) and (111) crystal faces" in cubo-octahedral particles. More recently, Shao *et al.*[51] compared the activity of Pt NPs ranging in size between 1 and 5 nm toward the ORR by employing density functional theory (DFT) studies,, and found that particles with a diameter of 2.2 nm and cubo-octahedral shape had the maximum mass activity.

Size-independent mass activities have been reported for NPs with small dimensions (1 - 5 nm) by Gamez and coworkers,[55] while other works [35, 45, 46, 56–59] have reported a variation in mass activity for Pt NPs as a function of size, but without a maximum in mass activity. Instead, the mass activity increases monotonically with decreasing particle dimension (increasing ECSA).

When a wide range of Pt NP catalyst sizes are considered (from about 150 $m^2\,g^{-1}$, or $\approx$2 nm, to extended surfaces with ECSA $<$1 $m^2\,g^{-1}$), the mass and specific activities of Pt as a function of particle size tend to fall about "master curves", as illustrated in figure 1.3, which gathers the results of several experimental studies. For both specific and mass activities, the curve is steeper at low ECSA values (larger particle size), and flatter for high surface areas (smaller NPs). This behaviour has been attributed to a shift in the potential of zero total charge to lower values as the particle size decreases, caused by a higher portion of undercoordinated Pt atoms at the surface, which leads to higher oxophilicity than in larger particles.[45, 60]

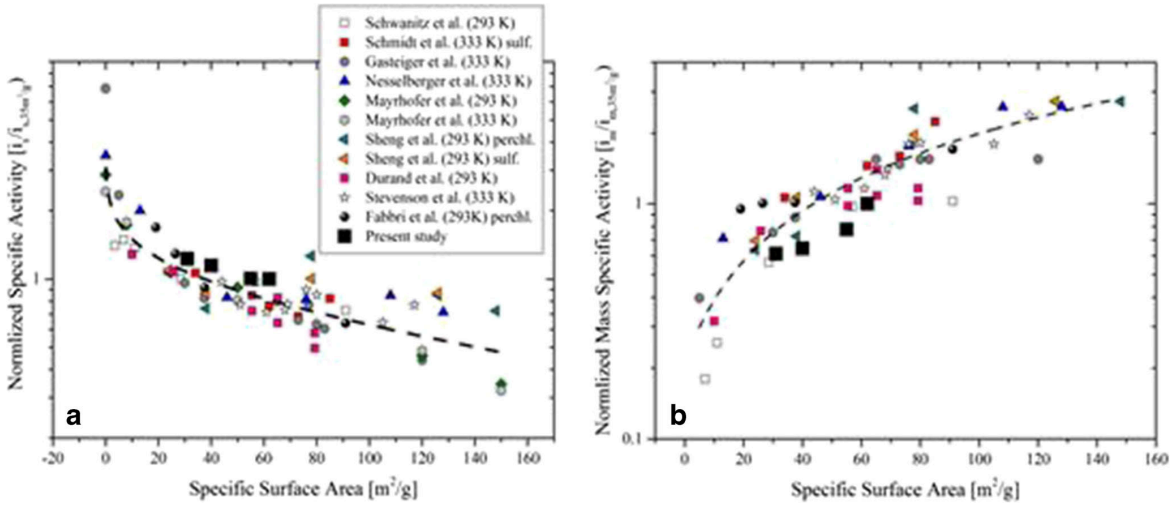

FIGURE 1.3: Relative **a)** mass and **b)** specific activity towards the ORR for different Pt catalysts. Activities recorded at 0.9 V *vs.* RHE and are normalised by the current values at ECSA = 35 $m^2\,g_{Pt}^{-1}$. Image and adapted caption from [61].

Contradictory results have also been found for the specific activity, SA, of Pt NPs, with some works reporting a decrease of the SA with decreasing particle size (see figure 1.3) and others[59] a size-independent behaviour for NPs with ECSA $\gtrapprox 40\,m^2\,g^{-1}$. Indeed, Nesselberger *et al.*[59] reassessed the model explored by Kinoshita [49], comparing it to more recent results obtained by employing a more refined methodology which compensated for the electrolyte resistance and capacitive current contributions from the high surface area carbon supports. The authors could find no agreement between the model and their experimental data.

The effect of interparticle distance (IPD) has not been as widely studied as the effect of the size, however, strong indications have been found that this parameter affects not only the catalyst activity, but also the reaction mechanism for the ORR.[41, 54, 62]

Watanabe[63] tested several samples with different high surface area carbon substrates and Pt NP sizes. The author found that, when the IPD was large enough (*ca.* 18 nm in pure oxygen and *ca.* 20 nm in air), the specific activity was independent of particle size, but it decreased at smaller intercrystallite distances. This effect was attributed to a "mutual inhibition" for the ORR, possibly caused by diffusion or mutual interaction, which effectively reduced the NP surface area that could be used to catalyse the reaction.

More recently, Nesselberger *et al.*[54] studied a series of catalysts prepared by depositing Pt NPs, with diameters ranging from 0.6 to 2.3 nm, onto planar, glassy carbon (GC) supports to investigate the effect of the IPD. The least dense sample had an average edge-to-edge interparticle distance of *ca.* 3 nm. The authors reported that the surface-area-normalized catalytic activity of Pt NPs increased significantly for edge-to-edge distances of <1 nm, and was almost unchanged for distances between 1.5 and 3 nm. This particle proximity effect was attributed to a change in the structure of the electric double layer and its potential distribution.

Yang *et al.*[41] also employed GC-supported Pt catalysts to investigate the effect of the IPD on the ORR catalytic activity. The Pt NPs in this study ranged in size from *ca.* 2.2 to 4.5 nm and the average IPDs from ≈11 to 57 nm. The authors found that the SA decreased with decreasing particle size, and that H_2O_2 formation increased with decreasing particle size and with increasing IPD. The decrease in SA was associated with a change in the reaction mechanism from a 4-electron to a 2-electron process.

An increased H_2O_2 yield with decreasing Pt loading (i.e. increasing distance between the Pt catalysts) was also reported by Seidel *et al.*[64] for GC-supported arrays of Pt nanodisks ($d \approx 100$ nm). The SA for these samples was independent of the Pt loading.

The same pattern for H_2O_2 formation with decreasing IPD was also reported for high surface-area carbon-supported Pt catalysts.[35, 36, 62] For example, Taylor *et al.*[35] studied the effect of loading on the activity of Pt NPs towards the ORR. The authors found that when Pt loading was increased from 20 to 80 wt-%, the morphology changed, transitioning from isolated NPs to agglomerates, interparticle distance decreased from 9.7 to 4.0 nm, specific activity increased from 16.1 to 26.3 $\mu A\,cm^{-2}_{Pt}$, and mass activity decreased from 9.99 to 8.15 $mA\,mg^{-1}_{Pt}$. Selectivity was also affected: the amount of H_2O_2 decreased with increasing Pt loading.

Finally, another factor to consider is the effect of the substrate, which can impact the catalyst's activity.[65, 66] The whole catalytic system must be taken into account. It is imperative that the catalyst itself is stable, but the support must also be chemically and mechanically stable under the operating conditions. For example, carbon corrosion is a known problem in fuel cells, and can lead to massive degradation of the electrodes.[37]

1.3 Electrodeposition: Nucleation and Growth

Electrodeposition (sometimes also called electrocrystallisation) is a technique in which metallic ions in solution are reduced at the interface between the electrode and plating solution, forming a new phase at the electrode's surface. In this thesis, the focus will be mainly on the electrodeposition of discrete metal nanoparticles onto a low energy substrate, i.e. where there is a low interaction energy between the metal and substrate (e.g. carbon).

Several steps are involved in electrodeposition: **1)** diffusion of ions (M^{n+}) in solution to the electrode's surface, **2)** electron transfer from the electrode to the metal ion, **3)** partial or complete loss of the solvation sheath surrounding M^{n+} and adsorption of the reduced neutral atom onto the substrate's surface (formation of "ad-atoms"), **4)** surface diffusion of ad-atoms, **5)** formation of critical nuclei (nuclei with radius $r \geq r_c$, where r_c is the critical radius, below which the nucleus is not stable) on the electrode's surface through the clustering of multiple ad-atoms, **6)** incorporation of ad-atoms at lattice sites of the growing particle, and **7)** development of crystallographic and morphological characteristics of the newly formed metallic deposits.[67]

The critical radius depends on the applied overpotential, η, and it becomes smaller with higher overpotential. The relation between r_c and η depends on the shape of the nucleus and on the nucleus-substrate interaction. For a sphere (minimal contact area with substrate), $r_c \propto 1/\eta^2$; for a cylinder, $r_c \propto 1/\eta$. Nuclei with $r < r_c$ are unstable, whereas those with $r > r_c$ will tend to grow.[67]

In theory, any of the first 6 steps listed above can be rate limiting (or rate determining), i.e. the slowest step in the process, which determines the overall rate. However, generally, for electrodeposition, it is assumed that steps 2 and 3 (electron transfer and subsequent changes in the solvation sheath) are fast.[67] In practice, nucleation and growth (N&G) are usually classified into one of two categories: interfacial (or charge) controlled, or diffusion

controlled. In the former case, the nucleus growth is determined (limited) by the rate at which ions can be reduced and incorporated into growing nuclei. For the latter, charge-transfer is rapid, and growth is controlled by the rate at which M^{n+} ions are transported to the electrode surface.[68]

Electrodeposition has several advantages as a method to produce (nanoscale) electrocatalysts: this technique results in highly electroactive nanostructures because the new metallic phase grows directly on the conducting or semiconducting substrate, ensuring good electrical connection, and is therefore especially well-suited for applications in which electrical connectivity is important, such as fuel cells[69, 70] and (bio)sensors.[71]

However, despite the intensive study of electrodeposition processes, precise control of the deposited nanoparticles, especially their size and size distribution, remains a major challenge for this technique. This issue has been extensively studied by Penner *et al.*.[72, 73] Penner[73] attributes the difficulty in controlling the size distribution to "diffusional cross-talk" between neighbouring metal structures on the electrode surface, or an "interparticle diffusion coupling" (IDC) mechanism. Nuclei are formed in a pseudo-random manner, preferentially on defects on the substrate surface, and depletion regions develop in the vicinity of each particle which grow with time until they overlap with neighbouring depletion zones; after enough time, these depletion zones cover the entirity of the substrate's surface. As a result, the size distribution of the electrodeposited particles becomes monotonically broader with deposition duration.[74, 75]

Penner[73] has found that this "cross-talk", or IDC mechanism, can be minimised by either of two strategies when electrodepositing metals by chronoamperometry. The first consists in separating nucleation and growth in time and reducing the growth rate; the second strategy uses the co-evolution of H_2 to control the size of the growing particles.

Separation of nucleation and growth is achieved by using a double pulse technique, in which first, a high overpotential ($\eta \approx -0.5\,\mathrm{V}$) is applied for a very short time ($t \approx 5$ - 10 ms) to force instantaneous nucleation. A second, longer pulse is then applied, at a low overpotential ($\eta \geq -0.2\,\mathrm{V}$) to induce growth under electron-transfer control (instead of under a diffusion control regime). This results in a slow growth of the electrodeposited particles, and reduces the radius of the depletion layer around them.

The H_2 co-evolution method works by generating a localised convective mixing of the solution in the vicinity of each nucleus as bubbles of molecular hydrogen are formed at, and then released from, the surface of the growing metal particles. A quantitative description of the convection generated by the gas evolution can be found in the literature.[76, 77] Penner[73] notes that an equivalent mixing effect cannot be achieved with commercially available rotating disks electrodes (RDEs). The maximum angular rate of rotation for the RDE is $\omega \approx 10^5\,\mathrm{s}^{-1}$, whereas the rate of rotation required to achieve the same effect as the H_2 bubbles would be 2 orders of magnitude higher.[76, 77]

Although these two strategies result in narrower particle size dispersion, they cannot be employed for all systems and desired particle sizes. Generally, they work well for obtaining mesoscopic particles, with diameters ranging between hundreds of nanometers up to a micrometer. Furthermore, the H_2 co-evolution method has only been shown to work for certain metals, such as Ni, Co and Fe, but has been unsuccessful for silver or other nonferromagnetic metals. It is possible that the magnetic properties of the growing nuclei plays an important role in this growth mechanism.[73]

1.3.1 Classical Nucleation and Growth Models

Traditionally, electrodeposition has been studied by depositing large numbers of nanoparticles, usually by chronoamperometry (CA) and analysing the electrochemical data (current-

time transients) by fitting them to continuous mathematical models to obtain mechanistic information about the electrodeposition process.[21, 68, 78]

The most frequently used analytical models are based on the assumption that the nuclei are formed according to the following rate law[79]:

$$\frac{dN}{dt} = A N_0 e^{-At} \tag{1.5}$$

$$N = N_0 \left(1 - e^{-At}\right) \tag{1.6}$$

where t is the pulse duration (in seconds) , N is the number of nuclei at a given time, N_0 is the saturation nucleus density and A is the potential-dependent nucleation rate constant (in nuclei per second). The limiting cases of equation 1.6, with large A and $A \to 0$ correspond to *instantaneous* and *progressive* nucleation, respectively.

Several adaptations have been developed to describe the nucleation and growth processes analytically based on equation 1.5 and different diffusional models. The most successful models take the overlap of neighbouring fields into account.

Sharifker, Hills and coworkers[80] attempted to solve this problem by assuming hemispherical diffusion to hemispherical nuclei. The resulting equations, which describe the current-time transients for the cases of instantaneous and progressive nucleation according to the Sharifker-Hills (SH) model are:

$$I_{SH,\,inst} = \frac{zFD^{1/2}c}{\pi^{1/2}t^{1/2}} \left[1 - e^{-N\pi kDt}\right] \tag{1.7}$$

$$I_{SH,\,progr} = \frac{zFD^{1/2}c}{\pi^{1/2}t^{1/2}} \left[1 - e^{-AN_\infty \pi k' Dt^2/2}\right] \tag{1.8}$$

where $k = (8\pi cM/\rho)^{1/2}$, $k' = 4/3k$, A is the steady state nucleation rate constant, N is the total number of nuclei, and N_∞ is the number density of active sites; zF is the molar charge, D is the diffusion coefficient, c the bulk concentration of the depositing species, M is the molecular weight, and ρ the density of the deposited material. Equations 1.7 and 1.8 describe the expected currents for instantaneous and progressive nucleation, respectively, and experimental chronoamperograms can be compared to the theoretical curves in their dimensionless forms, using I^2/I_{max}^2 *vs.* t/t_{max}, where I_{max} and t_{max} are the peak current and time.

The Scharifker and Mostany (SM) model[81] builds on the SH model, but assumes cylindrical diffusion fields around the growing nuclei, and does not distinguish between progressive and instantaneous nucleations. The time-dependent current is then described by:

$$I_{SM} = \frac{1}{\alpha(At)^{1/2}} \left\{ 1 - e^{-\alpha(At - 1 + e^{-At})} \right\} \tag{1.9}$$

where

$$\alpha = (2\pi)^{3/2} D \left(\frac{cM}{\rho} \right)^{3/2} \frac{N_0}{A} \tag{1.10}$$

In all cases, for long enough times, the current decays with $I \propto t^{-1/2}$, according to the Cottrell equation:

$$I(t) = \frac{zF D^{1/2} c}{\pi^{1/2} t^{1/2}} \tag{1.11}$$

A more comprehensive review of analytical and numerical models which describe the nucleation and growth processes during electrochemical deposition, their strengths and flaws, can be found in the literature.[68] Each model tackles the problem in a different way, but all have certain things in common. According to these models, nuclei start being formed in an initial phase, distributed randomly on the electrode surface. At this stage,

the interaction between their diffusion fields is negligible, and the current grows with the amount of deposited material. As the number and size of these nuclei increases, so do their surrounding diffusion fields, which begin to overlap with those of neighbouring particles. This results in a slowing down of the growth of the new phase. After long times, the overlapping diffusion fields cover the entirety of the electrode's surface. These processes are reflected in the *I-t* characteristics as an initial increase in current, followed by a decrease in its slope, and eventually an exponential decay. Good agreement has been found between this model and experiment, except for the initial milliseconds, where usually there is a high current and a sharp decay, generally attributed to the charging of the electrochemical double-layer.[80, 82]

It is worthy to note that, according to classical N&G models, growth by direct attachment is assumed. In this case, under diffusion control, the resulting diffusion zones surrounding each growing nucleus will expand to *ca.* 10 times the radius of the particles which originate them. Consequently, assuming a random distribution of particles, the whole electrode surface will be covered by diffusion fields at a surface coverage of $\approx$1%.[83, 84]

Fitting dimensionless *I-t* characteristics (normalised by the peak current and corresponding deposition time from an experimental choronoamperogram) allows the extraction of parameters such as the number of growing nuclei and the nucleation rate constant, as well as identifying if nucleation occurs via an instantaneous, progressive, or hybrid mechanism, due to the distinct, characteristic shapes of this curves.[68]

Instantaneous and progressive nucleation result in different current-voltage-time features, as illustrated in the chronoamperograms (CAs) that are shown in figure 1.4: figure 1.4(A) shows a typical experimental CA obtained during the electrodeposition of silver, and a control CA in just electrolyte solution (absence of Ag^+). The current and time characteristics are then normalised by the peak current and time, respectively, and compared to simulated, dimensionless curves according to the models for progressive and instantaneous nucleation

(figure 1.4(B)). For some metals, such as Ag, a good fit can be obtained. The decreasing current that was registered in the initial millisecond during the chronoamperogram can be attributed to the charging of the electrochemical double layer.[80, 82]

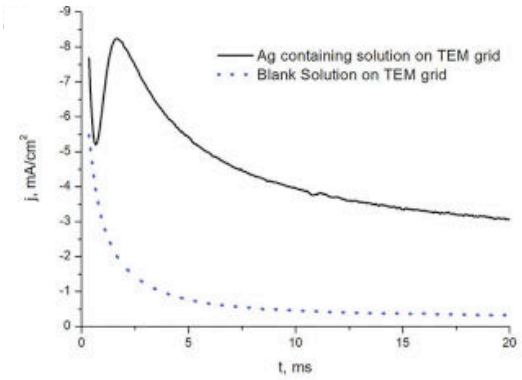

(A) Experimental chronoamperograms obtained during the electrodeposition of silver and control registered in electrolyte solution.

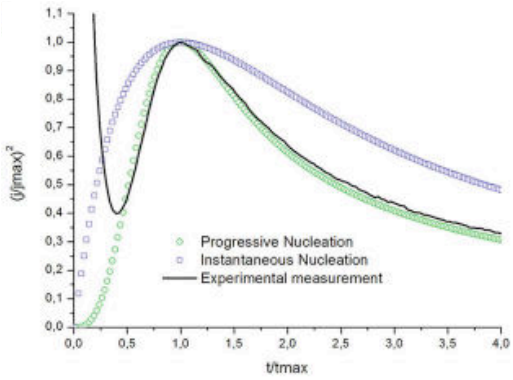

(B) Dimensionless chronoamperogram (A) and simulted chronoamperograms for progressive and instantaneous nucleation.

FIGURE 1.4: Experimental and dimensionless *I-t* transients obtained during the electrodeposition of silver from a $AgNO_3$ solution (1 mM $AgNO_3$ in 0.1 M KNO_3; WE = carbon-coated TEM grid; $E = -0.4$ V *vs.* Ag/AgCl.) Images obtained from [85].

The analysis of the electrochemical data is usually coupled with additional imaging or spectroscopic techniques, such as optical microscopy[68], FE-SEM,[86] AFM/STM,[68] and/or TEM[87]. This can be done *in situ* or *ex situ*. However, most of the techniques employed in such studies are limited to averaging over a large number of particles, encompassing areas that are much greater than the size of the electrodeposited particles. Consequently, mechanistic information about atomic scale processes is lacking and must be inferred by extrapolation.

For example, the horizontal (*x,y*) resolution in AFM/STM is strongly affected by the tip geometry, and the tip can "pick up" particles and move them[88] and FE-SEM cannot resolve features/NPs with diameters smaller than ≈5 nm.[89] Species with small dimensions,

from single atoms up to small clusters with dimension of just a few nanometers become undetectable.

The classical nucleation and growth (N&G) models predict that nuclei can be formed either by instantaneous or progressive nucleation, and that growth then proceeds by the irreversible direct addition of atoms onto particles until the reaction (application of a driving force) is halted. It is worth noting that particle growth according to these models should lead to a majority of the electrodeposited NPs to have defect-free, monocrystalline structures, and that growth proceeds irreversibly once a particle's radius exceeds the critical radius.

1.3.2 Non-classical N&G Models

Although the classical N&G models have been used and reviewed frequently,[68] they have been shown to fail to explain experimental observations appropriately in recent studies, bringing their validity into question. As the available microscopy techniques become more potent and able to achieve higher resolutions, discrepancies between the classical N&G models and experimental results started to become apparent, especially when comparing the values for the particle density, N_0, and size (usually expressed as the radius, r or diameter, d, assuming spherical or hemispherical particles) extracted from the current-time transients (expected value) and from experimental micrographs (usually employing AFM or electron microscopy).

Such discrepancies have been reported for several metals, including copper,[87, 90] palladium[91], silver,[21, 85] and platinum[78, 92]. Most commonly, the experimental island (or particle) density is 1 - 5 orders of magnitude higher than that determined by fitting classical N&G models to current transients.[78, 85, 87, 90, 92] Additionally, traditional models often cannot explain an initial high current, which decays exponentially, and can last up to a few seconds. Although this is usually attributed to the charging of the electrochemical

double layer, evidence suggests that it may be generated by the adsorption of atoms onto the substrate,[87] or by the formation of mainly small, primary clusters, which then aggregate to form larger particles,[84] in contradiction to the assumption by classical models that growth only occurs by the direct attachment of atoms onto growing nuclei.

Sections 1.3.2.1 and 1.3.2.2 highlight some of the works which have explored these discrepancies between experimental results and the classical N&G models, focusing on research which employed *in situ* and *ex situ* characterisation techniques, respectively, in combination with the electrochemical studies.

1.3.2.1 *In situ* TEM studies: adatom adsorption

In a series of studies on the potentiostatic electrodeposition of copper, Radisic and coworkers.[87, 93, 94] investigated the early stages of copper nucleation and growth from solutios containing 0.1 M $CuSO_4 \cdot 5\,H_2O$ with 1 vol.% H_2SO_4 (pH = 1), carried out at different potentials (E_{dep}), onto a Au substrate employing *in situ* TEM. This allowed the authors to correlate the current-time characteristics with the number and size of the copper deposits as a function of time. The experiments were carried out at potentials of $-0.05 \leq E_{dep} \leq -0.10\,V$ *vs.* Cu, in 0.01 V increments. Growth was found to be under diffusion control for $E_{dep} \leq -0.07\,V$, and under kinetic or mixed control for more anodic potentials ($-0.05 \leq E_{dep} < -0.07\,V$).

Images were recorded at a (video) rate of $30\,s^{-1}$, with a typical frame size of up to $\approx 2\,\mu m$ (field view area = $2.64\,\mu m^2$, about $1/760$ of the total working electrode area). The spatial resolution, which was limited by the thickness of the windows and liquid in the cell, was about 5 nm, and particles with diameters < 20 to 30 nm did not produce a strong enough contrast and could not be analysed.[93]

For the chronoamperograms registered under diffusion control, good agreement was found between the current transients and the Sharifker-Hills (SH) model after an induction period ($t_{ind} \approx 0.05$ to 2 s, depending on E_{dep}), as shown in figure 1.5. The current-time characteristics (for $t > t_{ind}$) reflect two main stages of growth: the first is consistent with nucleation under 3D diffusion limited growth of isolated hemispherical clusters, and the particle radii are expected to grow with $r(t) \propto t^{1/2}$, followed, at longer times, by 1D diffusion limited growth as a consequence of the overlap of the diffusion fields of individual growing nuclei, when the current magnitude decreases as $|I(t)| \propto t^{-1/2}$ and the particle growth rate slows down to $r(t) \propto t^{1/6}$.

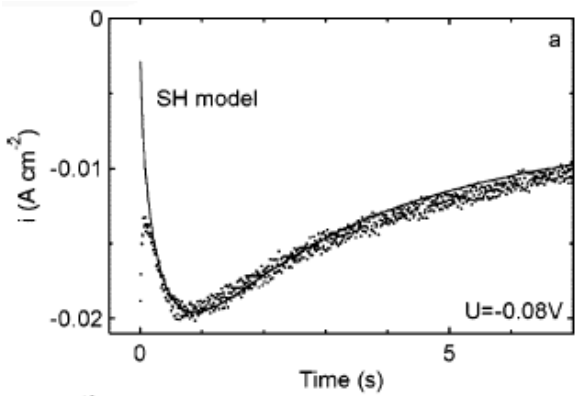

FIGURE 1.5: Experimental chronoamperogram (dots) and fit to the Sharifker-Hills model (solid line) for the electrodeposition of copper at $E_{dep} = -0.08$ V. Details in text. Image and caption adapted from [93].

Despite the regular features of the current-time transients, the authors found significant discrepancies between the expected (calculated from the CA) and experimental (obtained from the micrographs) nucleation density (N_0) and particle size (expressed as the radius, r), which are summarised in figure 1.6. The experimental growth rate (slope in figure 1.6(A)) is in good agreement with the modelled rate at short times ($t < t_{max}$), with a growth exponent of $\approx \frac{1}{2}$ for $E_{dep} \leq -0.07$ V, however, the experimental average particle radius is *ca.* 20 times smaller than predicted, resulting in average particle volumes that are ≈8000 times too low.

The experimental island density, N_0, on the other hand (shown in figure 1.6(A)), is *ca.* $3-4$ orders of magnitude higher than expected based on the SH model for all studied potentials.

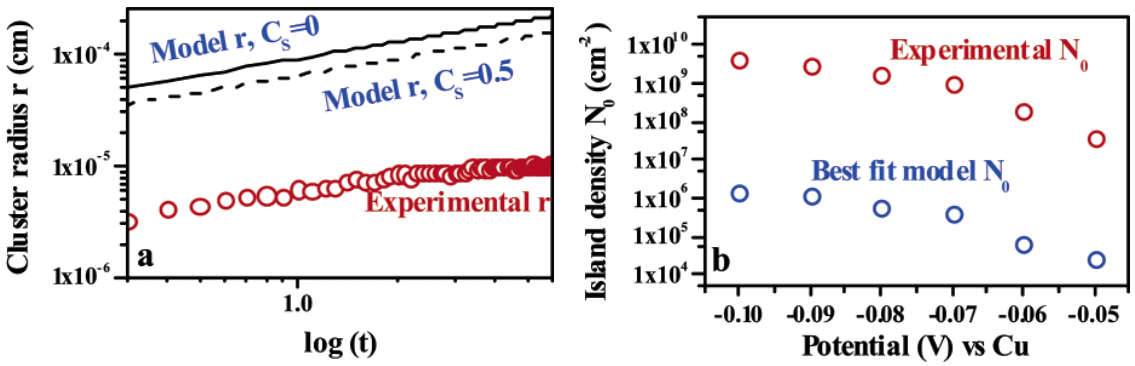

(A) (B)

FIGURE 1.6: Plots of **(A)** average particle radius, r, as a function of time ($E_{\text{dep}} = -0.07\,\text{V}$), and **(B)** particle density, N_0 as a function of potential, E_{dep}, for the potentionstatic electrodeposition of copper (details in text). Experimental values (red) were extracted from *in situ* TEM micrographs; expected values (blue) were calculated from the current-time transients. Images and caption adapted from [87].

Radisic and coworkers[87, 93] propose an explanation for these discrepancies based on adatom adsorption, in which two processes may be occurring in parallel: **i)** adsorption of ions onto the electrode surface, followed by surface diffusion and nucleation, which is stronger during the earlier stages ($t < t_{\text{ind}}$), and **ii)** conventional growth by direct attachment of ions from the solution onto existing metal nuclei, which becomes more dominant with time.

The formation of adatoms at the electrode surface would also explain the initial current decay in the chronoamperograms during the "induction period". Usually, this feature in a current transient is attributed to the charging of the double layer; however, this process should not last more than milliseconds, and in the experiments reported by Radisic *et al.*,[87, 93, 94] the duration of this exponential decay ranges from 0.05 to 2 s. The current contribution of this process (adatom adsorption) decreases with time, because the electrode surface area available for adatom formation decreases as nuclei are formed and start to grow. The adsorption/formation of adatoms at the surface leads to a higher density of nuclei than is

predicted by classical N&G models, and the higher island density leads to smaller particle dimensions.

1.3.2.2 *Ex situ* (S)TEM studies: aggregative growth mechanism

HAADF-STEM was first employed to investigate the early stages of electrochemical deposition of metals by Ustarroz and coworkers.[78, 84, 85, 89] The authors deposited silver and platinum onto carbon-covered TEM grids (CCTGs), which permitted the analysis of the as-deposited particles with high-resolution electron microscopy techniques, such as HR-TEM, FE-SEM and HAADF-STEM to obtain the deposited particle number density, size distribution and morphology .

The authors first used cyclic voltammetry to compare the performance of CCTG and glassy carbon (GC) as electrodes. It was found that the cyclic voltammograms (CVs) displayed the same characteristic features on both carbon electrodes, which were also in good agreement with the literature, confirming that silver electrodeposition and stripping follow the same mechanism on these different surfaces.[89]

The electrodeposition experiments were carried out using chronoamperometry. With the exception of the initial current decay ($t \leq 1$ ms), a good agreement was found between the experimental CA (in its dimensionless form) for the deposition of silver and the Sharifker-Hills (SH) theoretical model for progressive nucleation, as shown in figure 1.4, which allowed the extraction of the particle number density, N_∞, and nucleation rate, A (*vide* equation 1.8). However, this was not the case for platinum, which displayed a behaviour that was intermediate between the progressive and instantaneous SH models (figure 1.7). Furthermore, the authors also found discrepancies between the calculated particle number density (from the *I-t* transients) and that extracted from HAADF-STEM images.

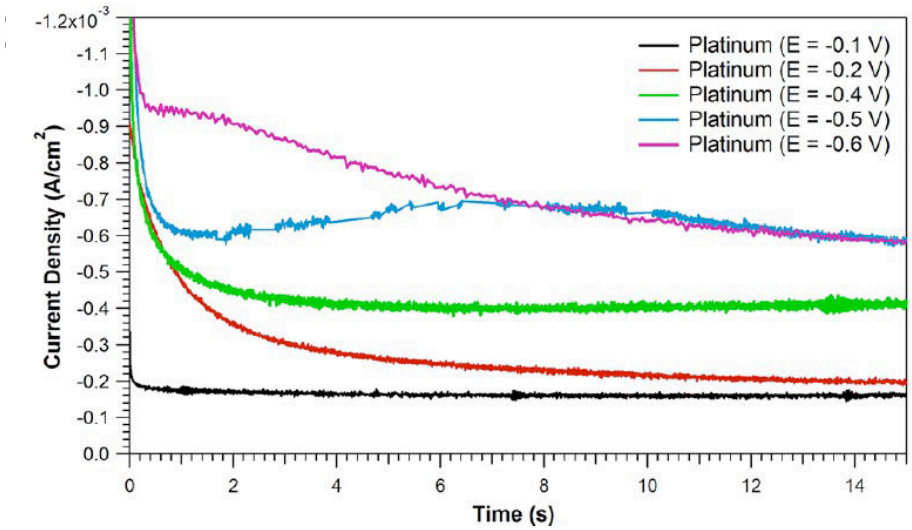

FIGURE 1.7: Current-time transients recorded during the electrodeposition of platinum at different deposition potentials. Image obtained from[84].

Interestingly, HAADF-STEM images revealed a bimodal size distribution for both metals. The average diameter for the "small" clusters in the bimodal distribution is different for Ag ($d_{\text{small, Ag}} \approx 1.8 \pm 0.6\,\text{nm}$) and Pt ($d_{\text{small, Pt}} \approx 2.9 \pm 0.9\,\text{nm}$), but independent of the deposition time or surface coverage, indicating that there is a self-limiting growth mechanism which is species-dependent. Due to the large size dispersion of the small particles ($\approx 32\%$), the authors argue that the most likely cause for the stabilisation of these clusters at small sizes is specific adsorption on the exposed facets of the small clusters.[84] The interplay between small and large silver and platinum NPs, deposited at high overpotentials, and how they evolve with time is depicted in figure 1.8.

For silver, it was observed that the small NPs were not distributed randomly on the substrate, being found preferentially close to larger particles. (Classical N&G models predict a random distribution.) The density of the small clusters increased with deposition time until, approximately, 10 ms, then decreases and, after *ca.* 30 ms, they become undetectable. The population of large silver NPs starts to grow, while maintaining a constant diameter, up to, approximately, 30 ms (when the small particles disappear); after this period, the density of

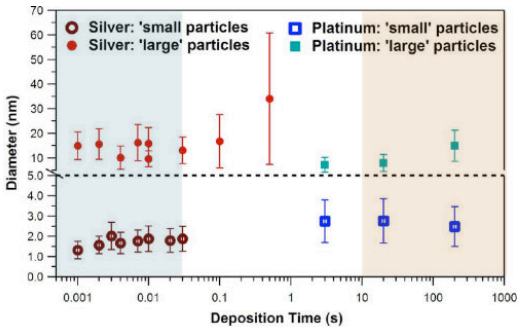

(A) Evolution of "small" and "large" particle diameter with time.

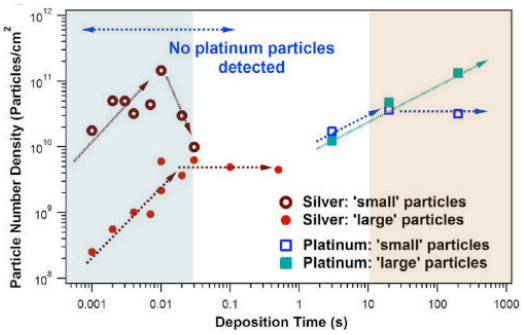

(B) Evolution of "small" and "large" particle density with time.

FIGURE 1.8: Evolution of Ag and Pt "small" and "large" particle **(A)** diameter and **(B)** density with electrodeposition time. Electrodeposition potentials were −0.4 V and −0.6 V vs. Ag/AgCl for Ag and Pt, respectively. The light blue background marks $t \leq 30\,\text{ms} \approx t_{\text{ind,Ag}}$ and the orange background $t \geq 10\,\text{s} \approx t_{\text{ind,Pt}}$. Image and caption adapted from [84].

large particles stabilises, but their average size strongly increases with time. The behaviour of the "large" Ag-NPs is consistent with the SH model for progressive nucleation.[85, 89]

For platinum, large particles can only be detected after a longer period, approximately 10 s, and their evolution is different for the high and low overpotential regimes. For high overpotentials (figure 1.8), the behaviour of platinum is similar to that of silver. Initially, there is an increase in the particle density for both small and large NPs. After a certain time ($\approx$ 10 s for Pt), both density and average diameter of the large particles grow, while the number of small clusters stabilises. For *low* overpotentials, almost no isolated small clusters are observed, independently of deposition duration.[78, 84]

Whereas, traditionally, an induction period is associated with the charging of the electrochemical double layer (steps **1** to **3** described in section 1.3, page 16) and expected to last for microseconds, Ustarroz and coworkers[84] proposed that the time elapsed between the start of the cathodic pulse and the appearance of large NPs, which is reflected by a current decay in chronoamperograms, corresponds to an "induction period" (t_{ind}), which the authors define as the time necessary for small particles to form and start aggregating. The induction

times are represented as orange and blue backgrounds (for platinum and silver, respectively) in figure 1.8.

It is worth noting that the "small" clusters cannot be accurately identified and characterised with the imaging techniques that have traditionally been employed in electrodeposition studies, which lack atomic-scale resolution. Their formation is also not reflected in *I-t* transients during electrodeposition because the currents they generate are much smaller than that of larger particles.

Regarding surface coverage, Ustarroz *et al.* observed that particle density stabilises for Ag at ≈1-2%, and no small clusters can be observed at higher coverages. This is in accordance with classical N&G theories, which predict the radii of diffusion fields to be approximately 10 times that of the particles that originate them. Consequently, the entirety of the electrode area should be covered by overlapping diffusion fields at surface coverages of ≥1%, preventing further nucleation. For platinum this is not the case, and small NPs can be detected even at surface coverages of ≈30%. This implies that the nucleation and growth of Pt NPs is not governed by diffusion. Kinetic control and blocking of the platinum surface by hydrogen evolution were also excluded by the authors.[78, 84] Instead, it is proposed that the growth of the NPs is controlled by the self-limiting mechanism that also limits the growth of the small clusters.

The morphology of the clusters, which was investigated thoroughly by HAADF-STEM and electron tomography, also provided new mechanistic insight into the early nucleation and growth processes of metals.[78, 84, 85, 89] The classical N&G models predict sustained growth by the direct addition of atoms onto particles for as long as a driving force is held, which would lead to defect-free monocrystalline structures. Instead, more than half of the large silver NPs displayed defects such as stacking faults and twinning planes, and some "medium"-sized Ag-NPs a polycrystalline structure (figures 1.9**(B)** and 1.9**(C)**). In the case of

platinum, all large NPs had highly porous, dendritic morphologies; This effect was stronger at low overpotentials (figure 1.9(D)) and less pronounced at high overpotentials (figure 1.9(E)).

Taking all this new evidence into account, the authors propose a revised nucleation and growth mechanism: a "generalised electrochemical aggregative growth mechanism"[84] for metal electrodeposition onto low energy surfaces, which is summarised in figure 1.9(A). First, small (or "primary") clusters are formed, randomly distributed throughout the electrode surface, and grow by direct attachment, with a monocrystalline structure, until a self-limiting mechanism (the exact mechanism is still unknown) stabilises them at a certain, species-dependent size. This period, which will have different lengths depending on the metal, is denoted as an "induction period" by the authors, because larger particles are not formed yet.[84]

After the induction period, the primary clusters diffuse over the substrate surface, driven by the applied electrochemical potential, facilitated due to their small size and the weak van der Waals forces between them and the carbon support. When primary nanoclusters meet other particles, they aggregate, in "aggregative-nucleation events", forming larger aggregated particles (case **1** in figure 1.9(A)). Further growth by direct attachment is strongly dependent on the rate and degree to which the aggregates undergo recrystallisation. This factor also determines the final structure of the larger electrodeposited NPs.

If the depositing metal undergoes recrystallisation easily and to a high degree, as is the case for silver (**2a** in figure 1.9(A)), particles will tend towards monocrystalline structures at long deposition times. As a particle grows and recrystallises, the self-limiting mechanism ceases and growth by direct attachment resumes.[84, 85] Once surface coverage reaches $\approx$1%, the diffusion zones of the growing recrystallised particles become large enough to encompass the entirety of the electrode surface. Once this happens, no more nucleation can occur, and growth can only continue by the aggregation of the remaining primary clusters; the density of small particles starts to decline, and that of the large particles stagnates. In the

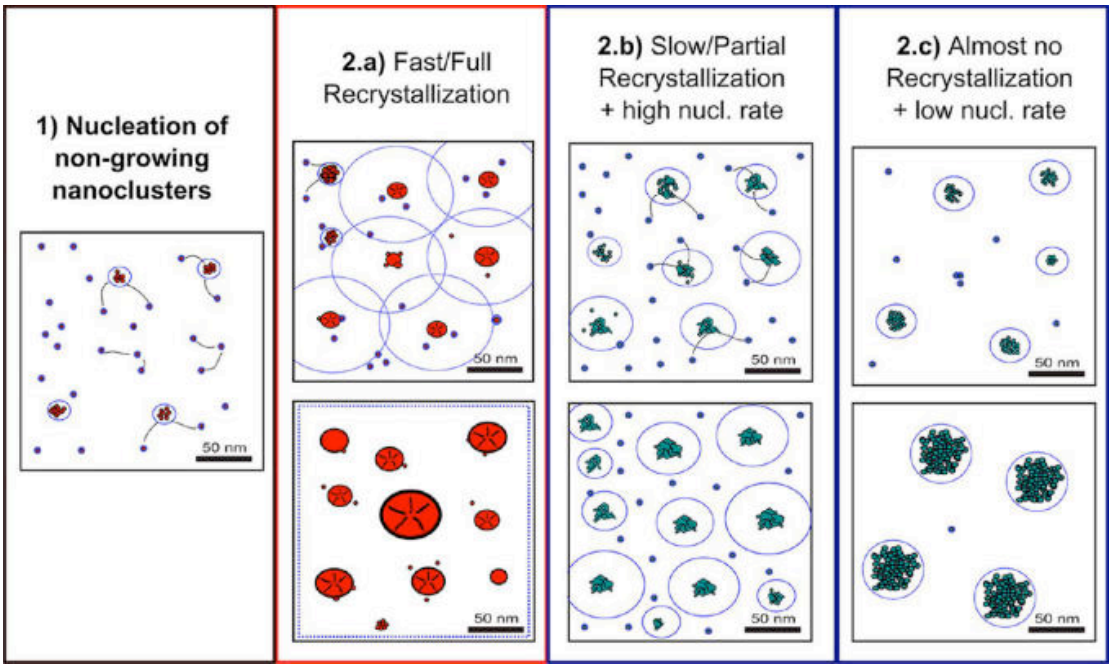

(A) Schematic diagram of the Generalised Electrochemical Aggregative Growth Mechanism proposed by Ustarroz *et al.*[84]. Small dots represent the small, "primary" clusters, larger particles that have recrystallised are depicted as red shapes (the black lines within these represent defects), whereas the porous structures formed by the aggregation of small primary clusters, without significant recrystallisation, are shown as agglomerates of small green dots. The blue circles around particles indicate the projection of their diffusion fields.

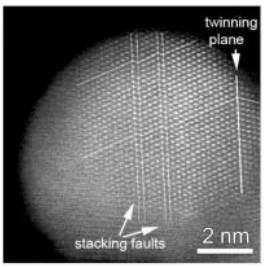

(B) Monocrystalline Ag-NP with defects. Image adapted from [85].

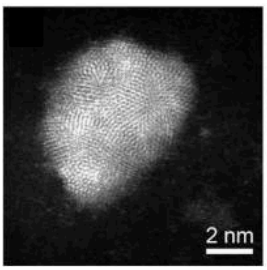

(C) Polycristalline Ag-NP. Image adapted from [85].

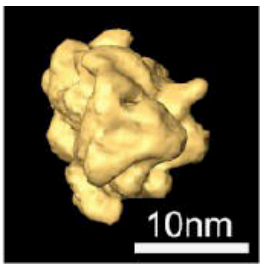

(D) Pt, high overpotential. Image adapted from [78].

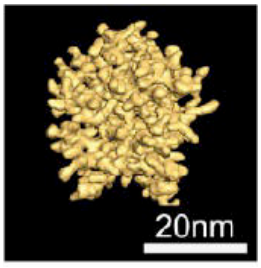

(E) Pt, low overpotential. Image adapted from [78].

FIGURE 1.9: **(A)** Schematic diagram of the Generalised Electrochemical Aggregative Growth Mechanism proposed by Ustarroz *et al.*[84]. **(B)** and **(C)** HAADF-STEM images of large Ag-NPs; Electron tomography reconstructions of typical large Pt-NPs deposited at **(D)** a high overpotential, and **(E)** a low overpotential.

chronoamperogram, this stage is reflected by a peak in the current, after which the current decays monotonically. In such a case, the *I-t* transient will be in good agreement with the classical model for progressive nucleation and growth, except for the initial induction period.

For platinum, two cases are differentiated, depending on the applied overpotential, which determines the rate of recrystallisation in larger particles, formed by the aggregation of primary clusters. These differences are also reflected in the resulting chronoamperograms (figure 1.7). In either of these cases, classical nucleation and growth models fail to provide us with a correct interpretation of the experimental results, and, in both cases, the aggregates' behaviour falls between that of traditional growing islands and that of non-growing particles, and only small diffusion fields are generated surrounding these species. Consequently, new primary clusters continue to be formed for longer periods, and into higher surface coverage rates, because the diffusion fields fail to enclose the entire substrate surface.

At high overpotentials, partial recrystallisation occurs. These cases are characterised by a broad wave in the chronoamperogram, and will result in structures with "medium" porosity, but smoother than in the last case (figure 1.9**(D)**).

If the degree of recrystallisation is very low, such as in platinum electrodeposition at low overpotentials, growth can only occur via aggregation of primary clusters with other particles (other primaries or aggregates), and does not lead to an increase of the active surface for metal cation reduction. In these cases, the current-time transients never rise with time and lack a peak; the resulting particle structure is dendritic and highly porous (figure 1.9**(E)**).

An aggregative growth mechanism for the electrochemical deposition of metals was further supported by studies carried out by Unwin's group.[21, 95] In these investigations, the authors employed SECCM to electrodeposit silver[21] and palladium[95] onto carbon substrates, which were then characterised using high-resolution techniques.

Electrodeposition of silver on a macroscale HOPG electrode resulted in only an imperfect agreement with classical N&G models, especially at longer deposition times. The best fit was obtained using the SM model (equation 1.9), which was used to estimate the number of apparent nucleation sites. However, *ex situ* analysis of the samples by FE-SEM and tapping mode (TM)-AFM revealed experimental densities of nucleation sites of about 10^7 to 10^8 cm^{-2}, 3 orders of magnitude higher than that provided by the SM model ($\approx 10^5$ cm^{-2}), even though the microscopy techniques that were employed in this study could not resolve particles with diameters smaller than 100 nm and 10 nm for FE-SEM and TM-AFM, respectively.

The electrodeposition of silver was also carried out using SECCM, with a double-barrel pipette with a tip with $d \approx 400$ nm. This experiment resulted in a very different *I-t* transient, as can be seen in figure 1.10, which shows the current-time traces obtained at $\eta = -0.1$ V. These are comprised of successive "events", with a fast current rise initially, and then a decay that can be described by a modified Cottrell equation for a micro- or nano-electrode.[21] This is followed by a period with no current. These events repeat periodically.

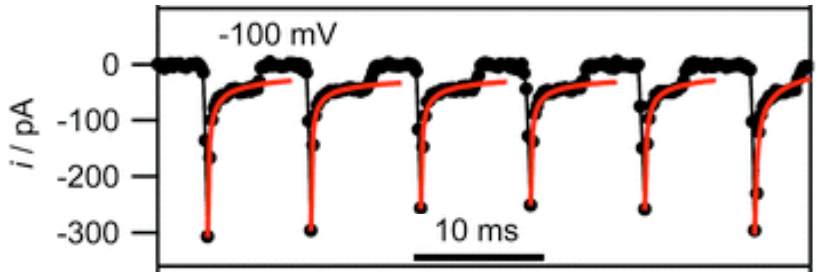

FIGURE 1.10: Current-time transient for the electrodeposition of silver in a SECCM setup with a pipette diameter ≈400 nm at an overpotential $\eta = -0.1$ V (black connected circles). The red lines are the fitted modified Cottrell curves. Each current event corresponds to the nucleation and growth of one silver NP. Image and caption adapted from [21].

Although the *I-t* transient registered approximately 100 to 150 discrete events during the entire contact time (1 s), high-resolution FE-SEM only revealed "a few" NPs.[21] Two control experiments were performed to elucidate what had happened. The same experiment was repeated, with and without $AgNO_3$ in solution and, after the application of the potential

pulse, the tip was broken onto the electrode surface, leaving a small volume of the solution on the surface.

No particles were detected from the solution containing only electrolyte, but a large number of large ($d = 28 \pm 11$ nm) NPs were found after the electrodeposition of silver. This set of experiments confirmed that a majority of electrodeposited Ag-NPs detach from the solution after being formed and reaching a certain size, going into (and remaining in) the solution.

The findings of this work, combining electrochemistry and microscopy, are consistent with a "nucleation-aggregative growth-detachment" mechanism for the electrodeposition of silver NPs onto HOPG, which is summarised in figure 1.11.

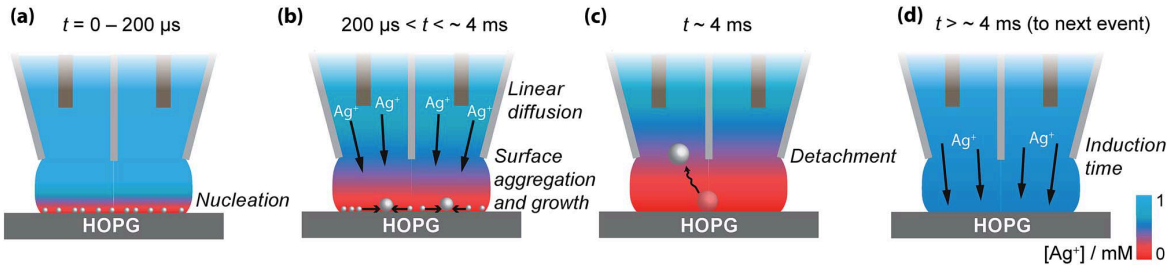

FIGURE 1.11: Nucleation-aggregative growth-detachment mechanism proposed by Lai *et al.*[21]. Description in text. Image from [21].

Initially (fig. 1.11(a)), many small, randomly distributed critical nuclei are formed at the electrode surface. This is reflected in the initial current spike of each event ($t \leq 200$ µs). These nuclei grow fast, consuming all the silver ions at the electrode surface and entering a diffusion-controlled growth regime, in which the growth rate is determined by the linear diffusion of the silver cations down the pipette barrel and into the meniscus (fig. 1.11(b), 200 µs to 4 ms). At the same time, these small nuclei, which are mobile on the electrode surface, aggregate to form larger NPs. This is in accordance with the findings of Ustarroz *et al.*[84, 85]. Finally, after ≈3 to 5 ms, the NPs reach a critical size at which it becomes more energetically favourable to diffuse into the solution than to remain adsorbed on the substrate.

The NPs then detach from the surface and diffuse/are transported into the electrolyte solution, up the barrel of the pipette (fig. 1.11(c)).

Before this cycle can begin again, the silver ions at the electrode surface need to be replenished. The time it takes for them to diffuse down to the surface is reflected in the "induction time" between current events (a few ms, fig. 1.11(d)). The duration of this induction time, observed experimentally, is in accordance with the expected diffusional time needed for the Ag ions to diffuse onto the surface.[21] Further evidence for detachment during electrodeposition (as opposed to due to the lifting/removal of the meniscus from the surface) comes from experiments that were run for longer durations. In such experiments, it was found that the frequency of the events ($\approx$ 100-150 events/s) does not decrease with time. Assuming that each event produces a NP with an average diameter of 30 nm, and the whole surface should be covered by Ag.

It is important to note that this mechanism is specific for SECCM: the size and geometry of the meniscus setup encourage the detachment of the electrodeposited NPs and diffusion into the solution due to the small contact area between the droplet and electrode combined with the relatively high volume of solution.[21]

In another electrodeposition study using SECCM, Kim *et al.*[95] deposited palladium onto HOPG using double potential step chronoamperometry (DPSC), employing a cathodic pulse (potentials and durations were varied between $+0.2 \geq E_c \geq +0.025$ V and $0.6 \leq t_c \leq 1$ s) to generate Pd-NPs, whose surface was then oxidised to palladium oxide (PdO) during the subsequent anodic pulse (always $E_a = 1$ V *vs.* Ag/AgCl QRCE, $t_a = 1$ s). The reduction and oxidation charges (integrated current as a function of time) for each experiment were used to calculate the total amount (volume) and electrochemical surface area of the electrodeposited Pd-NPs, respectively. Particle size (radius) and density (particles cm^{-2}) were also estimated using these parameters, assuming spheres and monodispersed particle size.

Before performing electrodeposition experiments on a TEM grid, the authors compared the cyclic voltammetric (figure 1.12) and chronoamperometric (not depicted) responses on HOPG and a CCTG.[95] Each time, the same setup was used with a 2 µm diameter micropipette. Kim *et al.* found evidence for slower kinetics on the TEM grid substrate, reflected in a longer lag time and lower current magnitudes for this electrode. The authors suggest that this difference may be due to the lack of features such as step edges, which are abundant on the HOPG used but absent on the CCTG.

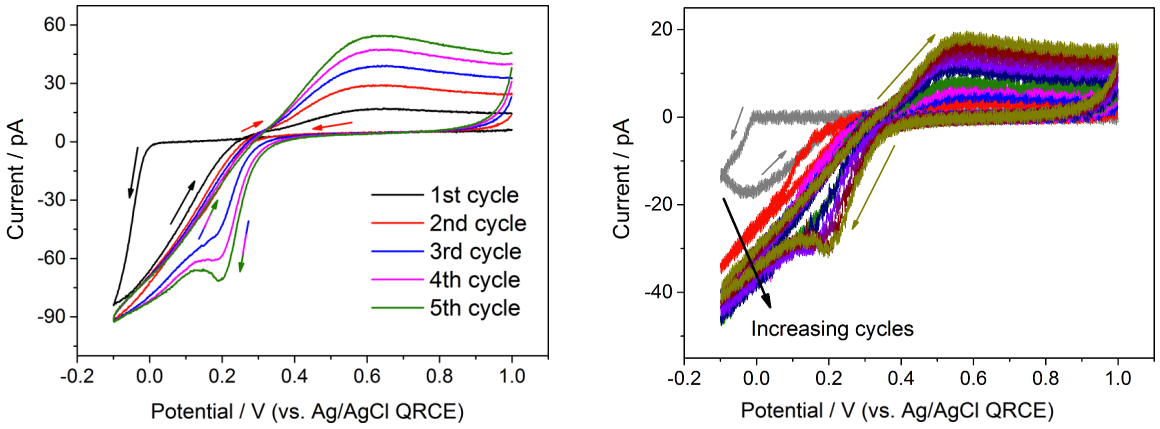

(A) WE = HOPG. **(B)** WE = CCTG.

FIGURE 1.12: Cyclic voltammograms for 1 mM K_2PdCl_4 in 0.1 M $HClO_4$ on **(A)** HOPG and **(B)** CCTG electrodes with a SECCM setup using a 2 µm diameter micropipette; scan rate $\nu = 0.2\,\mathrm{V\,s^{-1}}$. The arrows indicate the scan direction. Images and adapted caption from [95].

Palladium was deposited onto a carbon-coated TEM grid using a single pulse, at $E_{appl} = 0.05$ V *vs.* Ag/AgCl QRCE and for a longer duration, $t = 14$ s, in order to compensate for the slower kinetics on this substrate. The TEM images obtained from this sample revealed areas with aggregated large Pd structures, such as region 3 in figure 1.13(A), and a gradient in the degree of aggregation with distance from these large structures (e.g. region 2 *vs.* region 1 in figure 1.13(A)).[95]

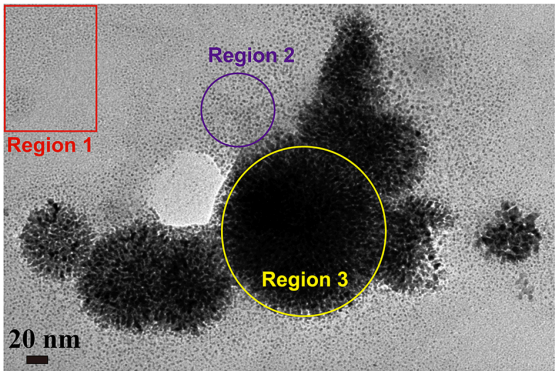

(A) TEM images of Pd NPs electrodeposited on a CCTG after 14 s deposition at 0.05 V.

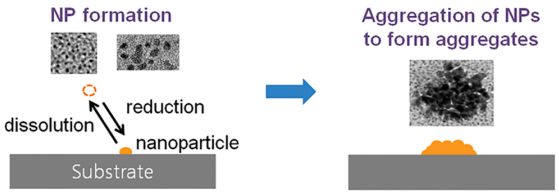

(B) **LEFT** reversible formation/dissolution of metal NPs and **RIGHT** irreversible aggregation of NPs to form extensive aggregates.

FIGURE 1.13: **A)** TEM image of electrodeposited Pd NPs, and **B)** schematic illustration showing the proposed electrochemical nucleation and growth processes. Image and adapted caption obtained from [95].

Higher magnification images revealed a mean particle size of $d = 1.0 \pm 0.1$ nm and density of $N_{\mathrm{TEM}} = 7 \times 10^{12}$ cm^{-2} in region 1 and $d = 2.2 \pm 0.4$ nm and $N_{\mathrm{TEM}} = 1.2 \times 10^{13}$ cm^{-2} in region 2. Region 3 shows evidence of being built of smaller NP aggregates.

The TEM results (particle size and density) were found to be in good agreement with those calculated from the *I-t* transients, with radii ranging between 0.8 and 1.7 nm and densities between 1.3 and 6.5×10^{12} particles /c^{2}m, depending on the deposition conditions. The higher value for r and lower densities obtained from the electrochemical data can be attributed to the aggregation of the NPs.

These results are consistent with a nucleation and aggregative mechanism[84], and Kim and coworkers[95] propose a model, illustrated schematically in figure 1.13**(B)**, in which the first step consists in the rapid and reversible nucleation and dissolution of discrete NPs. The electrodeposited particles are mobile on the substrate[21, 96] and must attain a critical size (and aggregate) to become stable on the substrate. Consequently, the resulting *I-t* transient is determined by the NPs that survive. The model developed in this work allows the determination of the potential-dependent rates for nucleation, dissolution and aggregation

from the *I-t* characteristics registered during the DSPC, and the authors propose that this model could be used to help control the number of deposited NPs by tuning the deposition time and potential.

1.4 Summary and objectives

A majority of electrochemical studies about the activity of Pt nanoscale catalysts is performed on relatively poorly defined systems, with NPs having relatively broad size distributions (e.g. $\geq 30\%$ [35]), or, more often, with only an average particle size being given, without information about the size dispersion.[47, 54, 59, 63, 97] Additionally, in several studies, catalysts are prepared by conventional, wet-chemistry synthesis methods in which the particle size and catalyst loading cannot be controlled separately.[54]

Well-defined and -characterised Pt NP systems are essential in order to reliably identify the effects of particle size, structure, and interparticle distance on the electrocatalytic activity. Ideally, the studied catalytic systems should have NPs with minimal size dispersion and good control over the Pt loading / interparticle distance. Finally, characterisation of a representative and sufficiently large section of each sample should be performed with the highest possible (ideally, atomic) resolution.

Traditional nucleation and growth models are based on the assumption of immobile nuclei, which become stable after reaching a critical size, grow as long as a cathodic overpotential is applied, and only by the direct incorporation of atoms. However, recent studies have reported significant discrepancies between predicted and experimental results, challenging the validity of these models, especially during the initial stage. Notably, evidence has been found for processes which occur in parallel with the growth of metal nuclei by direct attachment, especially before the diffusion fields expand to cover the entire working electrode area. These processes are the adsorption of atoms onto the substrate, and the formation of small, "primary

clusters", which undergo self-limiting growth (the size seems to depend on the metal, but not on the applied potential). Such primary clusters can aggregate to form larger particles. Recently, a generalised aggregative growth mechanism has been proposed, however, the details are still under discussion.

The objective of this thesis is to gain new insights into the electrochemistry of platinum at the nanoscale. The work presented here is divided into two parts: the first, presented in chapter 3, explores the catalytic activity of size-selected Pt clusters, and the second (chapter 4) investigates the electrodeposition of platinum. Throughout this thesis, a combination of electrochemical experiments performed by scanning electrochemical cell microscopy (SECCM, described in section 2.2) and sample characterisation by high angle annular dark field scanning transmission electron microscopy (HAADF-STEM, *vide* section 2.3) is employed.

In chapter 3, a magnetron sputtering, gas aggregation cluster beam source with a lateral time of flight mass filter (described in section 2.1) was employed to generate well-defined samples, with mass-selected platinum clusters with 923 atoms, Pt_{923}, (relative mass dispersion $\frac{\Delta m}{m} \approx 5\%$) which were deposited onto carbon-covered gold TEM grids (CCTGs) with controlled particle densities. These samples were used to study the electrocatalytic activity of the Pt_{923} clusters (diameter $d \approx 3\,\text{nm}$) and the effect of the Pt loading on the ORR, while maintaining the particle size constant, and to investigate the changes in the Pt/C system as a consequence of driving this reaction.

CCTGs were also utilised as working electrodes for the study of the electrodeposition of Pt onto a carbon substrate, described in chapter 4.

In both cases, SECCM was employed to perform electrochemical experiments in small areas (up to a few μm^2) on the same TEM grid samples, ensuring that the same system would be investigated multiple times. The use of this technique also allowed the imaging of a large

portion of the total effective working electrode for each experiment with *ex situ* HAADF-STEM. A thorough statistical analysis of the micrographs was performed to characterise the platinum NPs and correlate changes in the samples with the electrochemical data to gain a better understanding of the mechanisms which occur during the ORR and electrodeposition, respectively.

Chapter 2

Experimental Methods

2.1 Cluster Source

Size selected platinum clusters were generated and deposited onto TEM grids using a magnetron sputtering, gas aggregation cluster beam source[98] with a coupled lateral time of flight mass selector.[99] This equipment is referred to as just "cluster source" in this thesis.

A schematic illustration of the equipment is shown in figure 2.1. The cluster source consists of four sections: the condensation chamber (C1), the ion optics section (C2), the lateral time-of-flight (LTOF) mass filter (C3), and the deposition chamber (not depicted). All sections of the cluster source are differentially pumped to a base pressure of $\approx 10^{-7}$ mbar. The performance of the rotary and turbo vacuum pumps is monitored by pirani and penning gauges.

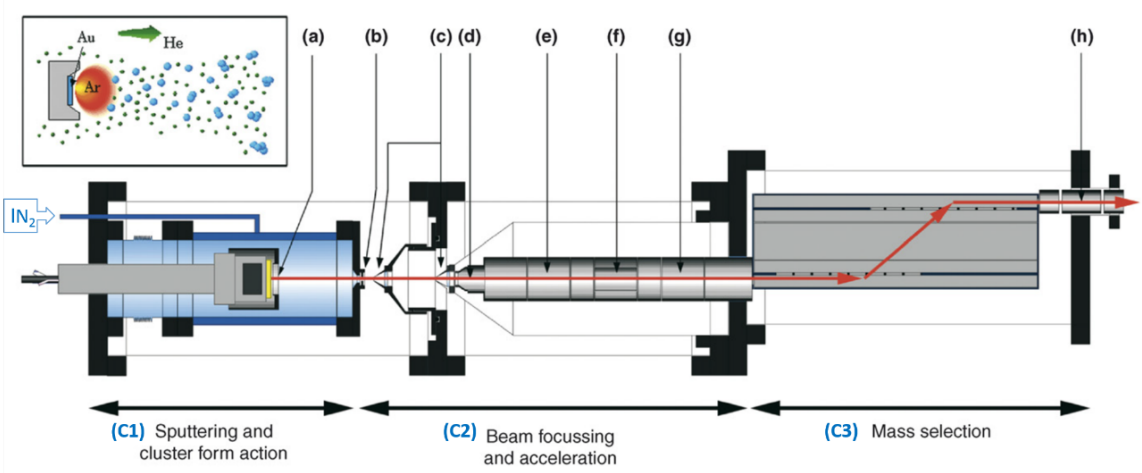

FIGURE 2.1: Setup of the magnetron gas condensation cluster source with LTOF mass filter: **(a)** The magnetron gun with a gold target; **(b)** an adjustable-diameter nozzle; **(c)** electrostatic skimmers; **(d)** a high voltage lens; **(e)** an Einzel lens for controlling the kinetic energy of the clusters; **(f)** X–Y deflector plates for spatial control of the cluster beam; and **(g)** and **(h)** Einzel lenses. The red arrows indicate the trajectory of the (sizeselected) clusters in the instrument. Figure and caption adapted from [100].

2.1.1 Magnetron Sputtering and Gas Condensation

Clusters are formed in the condensation chamber, where a 2 inch disk of the target material (e.g. metal, alloy or oxide) is mounted in front of a magnetron on a movable, axial arm (a in figure 2.1). For the work presented in this thesis, a 99.95% pure platinum target was used, purchased from PI-KEM. Argon, the sputter gas, enters the chamber in a controllable flow, and a plasma is ignited by applying a high voltage to the target; the Ar^+ ions are accelerated to the target, which is negatively biased, creating a dense vapour of sputtered atoms, ions and small clusters in front of the target. The introduction of helium gas cools the sputtered species, inducing the condensation of clusters. Small cluster "seeds" are formed in three-way collisions with He atoms, which dissipate excess kinetic energy from the sputtered species. Larger clusters can be formed by two-body (e.g. cluster-cluster) collisions[101] or by atomic vapour condensation onto cluster seeds.[102] The formation of larger clusters is

further encouraged by liquid nitrogen cooling of the chamber. The flows of the two gases are adjustable independently by mass flow controllers.

An advantage of magnetron sputtering is that it readily ionises ≈30%[103] of the sputtered material in the plasma, allowing the use of ion optics and mass filter without the need for a further, ionisation step.[98]

The cluster size range that is generated in the condensation chamber can be controlled by regulating the flows of Ar and He (up to 200 sccm), the aperture of the nozzle (b) (up to a 10 mm diameter), the distance between the magnetron head (a) and the nozzle (b) (which determines the volume in the chamber; can be varied between 150 and 250 mm), and the magnetron power. Modifying the conditions in the condensation chamber can also influence the proportions of different structural isomers[104] or the composition of bimetallic clusters.[105]

2.1.2 Ion Optics and Lateral Time of Flight Mass Filter

The gas, including clusters in a wide range of sizes, exits the condensation chamber through the adjustable nozzle (b) into the ion optics chamber (C2) through supersonic expansion. There, cationic species can be accelerated and focused by a set of electrostatic lenses and plates (c-g) through the application of tunable negative potentials. The focal point of the beam is set to the small aperture at the opposite (right side) end of the mass selector's wall.

Mass selection is achieved by using a lateral time of flight (LTOF) mass filter (C3); a more detailed schematic can be seen in Figure 2.2, and an in depth discussion of this technique can be found in the literature.[99, 106] Plates 1 and 4 are connected to high-voltage switches, plates 2 and 3 have mesh-covered openings so that the cluster beam can transverse them.

The regions between plates 1 and 2, and between 3 and 4 are called the acceleration and deceleration zones, respectively. The area between plates 2 and 3 is a field-free region.

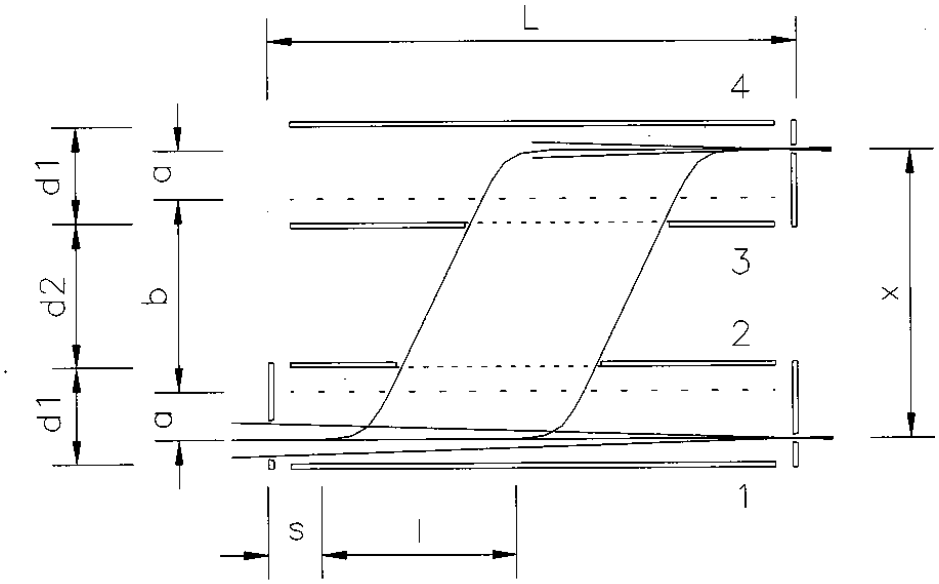

FIGURE 2.2: Schematic of the LTOF mass selector. A detailed description is given in the text. Image and adapted caption from [99].

As the focused ion beam enters this chamber, it is "bent" laterally (upwards) through the application of a high voltage pulse on plate 1, which generates an electric field perpendicular to the beam's original direction. The duration of this pulse is set so that the clusters will travel a distance *a* upwards (smaller than, but close to the height of the acceleration region), ensuring that no particle can leave the acceleration zone while the pulse is applied. Consequently, all ions gain the same momentum, and the upwards velocity of each ion depends on its mass. The length of the opening in plate 2 determines the length of the ion package, *l*, that travels upwards through the LTOF filter.

The beam travels a distance *x*, crossing the field-free region and into the deceleration zone. Here, the lateral momentum of the beam is cancelled by a second pulse (applied to plate 4), of equal magnitude and duration, but in the opposite direction as that applied by plate 1, returning the beam to its horizontal flight direction. (Note that *b* corresponds to

the distance travelled by the ion beam between the end of the upwards and the start of the downwards pulses.) The result of the lateral displacement of the beam is that the original ion beam is separated into parallel beams according to the mass of the ions, and only the portion of this beam with the desired mass range is allowed to exit through the exit aperture and into the deposition chamber. [99]

The mass resolution for the LTOF mass filter is independent of the mass of the selected ions. It is determined by the ratio of the lateral displacement, x, and the width of the exit aperture, Δx:[99]

$$R = \frac{m}{\Delta m} = \frac{x}{\Delta x} \tag{2.1}$$

The current setup has a height of 180 mm, and throughout the work done for this thesis, the maximum aperture height was used for the exit aperture ($\Delta x = 8$ mm). Accordingly, the theoretical (maximum) mass resolution is $R = \frac{x}{\Delta x} = 22.5$.

The real mass resolution needs to be calibrated from a peak of known mass (e.g. Ar^+ or $Pt_1{}^+$ ions), and it varies with time. Factors such as the liquid nitrogen cooling condition, temperature of the condensation chamber, deformation of the target surface, material precipitation on the lenses are difficult to control and can impact the focus of the beam, which will influence the real mass resolution.[98] For example, figure 2.3 shows two mass spectra of $Pt_1{}^+$. The peak position and full width half maximum (FWHM) of the best fitted Gaussian were used as m and Δm to calculate the experimental values for the resolution (eq. 2.1) and relative mass dispersion ($\frac{\Delta m}{m}$). The results were 18.4 and 17.4, or 5.4% and 5.8%, for the spectra in figures 2.3(**A**) and 2.3(**B**), respectively.

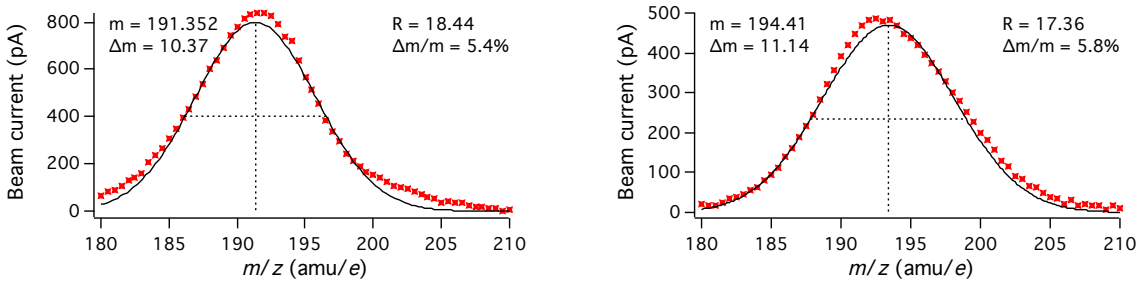

(A) (B)

FIGURE 2.3: Mass spectra of Pt_1^+ obtained under different conditions. Red markers: experimental data, black lines: fitted Gaussian curves, dotted lines: height and FWHM of the Gaussian.

2.1.3 Deposition

Finally, the beam of size-selected clusters enters the deposition chamber. Here, it can be deposited onto an appropriate substrate, e.g. a TEM grid or an electrode material, such as a glassy carbon disc. The size-selected cluster beam current is measured by an electrometer with a noise level of $\approx$ 1 pA.

The impact energy of the species in the beam is predominantly determined by the substrate voltage ($\leq$1500 V). There are 3 landing regimes, depending on the NC's acceleration energy: soft-landing, pinning, and implantation.[107] The exact energies needed for these thresholds depends on the composition of the clusters and substrate, but generally they are *ca.* $<$10 eV per atom for soft-landing and $>$20 eV per atom for implantation. Soft-landed NCs will suffer the least degree of deformation upon impacting on the substrate; however, they may diffuse on the surface and aggregate due to the relatively weak cluster-surface interaction. Pinning occurs when the impact between the cluster and the (carbon) surface causes a point defect in the substrate, which binds the cluster more strongly to the surface than in the soft-landing regime, suppressing cluster diffusion.[108] Clusters deposited at very high energies can be implanted into a soft substrate (e.g. graphite), creating a "well", the depth of which can be controlled.[109] Such an impact can deform or damage the NCs.

In the work presented in this thesis, substrate voltages of 500 and 1500 V were used to deposit Pt_{923} clusters in a soft-landing regime, corresponding to energies of 0.54 and 1.63 eV per atom, respectively.

2.2 Scanning Electrochemical Cell Microscopy

Scanning electrochemical cell microscopy (SECCM) is a droplet-based scanning probe microscopy (SPM) technique that allows the conduction of highly localised electrochemical experiments. The probe in SECCM is usually formed by a pipette or capillary, whose tip dimensions can be in the range of tens of nanometres[110, 111] up to micrometres. A cell is formed when the liquid meniscus touches the sample, confining electrochemical measurements to the contact area between the droplet and specimen and providing spatially resolved topographical and electrochemical information about the sample's surface. The probe can approach, make contact, retract, and move parallel to the substrate's surface repeatedly. The spatial resolution of the technique is determined by the contact area between the droplet meniscus and the substrate, which depends on the size of the tip of the pipette and the wetting of the specimen's surface.[112]

SECCM probes are shaped from borosilicate or quartz pipettes in a laser puller. By adjusting the puller parameters, tips with specific diameters can be fabricated easily and reproducibly. Pipettes with different geometries can be used to create SECCM probes, depending on the application. Single-barrel or single-channel pipettes (represented in figure 2.4(A)) can be used on semiconducting and conducting substrates, and make the use of the smallest tips possible. Double-barrel (or theta / θ) pipettes (figure 2.4(B)) can be used for the same types of experiments as single-barrel probes, but, additionally, they can also be used on non-conducting surfaces.[113]

The probe is filled with a solution containing an electrolyte and/or electrochemically active species, and a quasi-reference counter electrode (QRCE) is inserted into each compartment at the top of the pipette. At the bottom, under the tip, the liquid naturally forms a small droplet which, in the case of probes with inner divisions (e.g. θ pipettes), electrically connects all sections of the probe.[114] The ouside walls of the pipette probes can be silanised with dimethylchlorosilane ($[Si/CH_3)_2Cl_2]$) to help confine the meniscus formed by aqueous solutions,[115] and a thin layer of silicone oil can be used to cover the surface of the solution at the top of the pipette in order to minimise evaporation of the liquid.[116] Chloridized silver (Ag/AgCl), Pd-H_2 or Pt wires are often used as QRCEs. The two QRCEs in a double-barrel probe should be identical.[117]

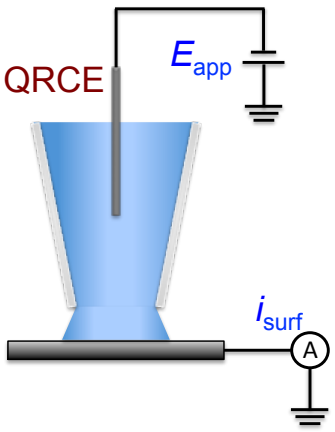

(A) Electrochemical cell configuration with a single barrel probe (adapted from [118]).

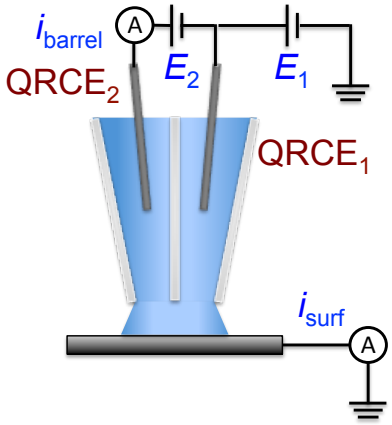

(B) Electrochemical cell configuration with a double barrel probe (adapted from [114]).

FIGURE 2.4: Schematic overview of scanning electrochemical cell microscopy cell configurations with probes with different geometries.

The electrical circuit is closed, forming a cell, when the liquid below the tip touches the surface of the sample. The shape of the meniscus, when in contact with the substrate, depends on the wetting properties (hydrophilicity/hydrophobicity) of the surface and the volume of the liquid in the droplet under the pipette. Electrodeposition experiments can be used to accurately determine the meniscus contact area and have provided evidence that, typically, the contact radius is mostly determined by the radius of the tip, varying only by up to 20%

of the pipette radius for silanised tips.[112] Furthermore, simulations using finite element method (FEM) models have shown that the diameter of the meniscus contact area and the height of the droplet have limited effect on the steady-state, diffusion-limited current.[119]

Generally, the sample is held at ground, and the potential difference is driven through the QRCE(s)[114]. For a cell with only one QRCE, the potential at the sample's surface, E_{surf}, will be $E_{surf} = -E_{app}$ (see figure 2.4(A)) and for a θ pipette with two QRCEs, in a typical case in which the barrels are symmetrical and the septum is in the centre of the pipette (as in figure 2.4(B)),[112] the potential at the substrate's surface is given by:

$$E_{surf} = -(E_1 + E_2/2) = -E_1 - E_2/2 \tag{2.2}$$

In the case of the double-barrel, two-QRCE probe, in addition to i_{surf}, there is also a current component that is measured, in parallel and simultaneously with i_{surf}, between the two QRCEs. The potential difference, E_2, results in direct current (DC) component, i_{DC}, due to the migration of ionic species (e.g. electrolyte) in the solution between the barrels "ion conductance current across the liquid meniscus".[112] Additionally, an alternating current (AC) component, i_{AC}, can be generated when the probe is oscillated sinusoidally in the z-direction (normal to the sample). This component oscillates about i_{DC} at the same frequency as the vertical movement because of the reversible deformation of the droplet. The magnitude of the AC component (i_{AC}) of the barrel current depends strongly on the meniscus height (see figure 2.6). It is detected by lock-in techniques[112] and can be used as a "feedback parameter" to control the distance between the tip and the substrate.

A typical SECCM workstation is illustrated in figures 2.5(A) and 2.5(B), which depict the detailed setup of probe and sample, and the arrangement of the complete workstation, respectively. The sample (**1** in figure 2.5(A) - fig 2.5(A)-**1**) is mounted on a sample holder (fig. 2.5(A)-**2**), which is usually placed on x, y piezoelectric positioners (fig 2.5(A)-**3**). The

pipette (fig 2.5(A)-**4**) is secured onto a probe holder (fig 2.5(A)-**5**) which is mounted on a z piezoelectric positioner (fig 2.5(A)-**6**). A coarse control of the probe's position relative to the sample is achieved through a manual x, y, z stage (fig 2.5(A)-**7**), onto which the z piezoelectric positioner (and probe holder) is attached. An optical microscope can be placed under the sample stage and cameras with zoom capability can be used to help visualise the position of the tip relative to the sample's surface.

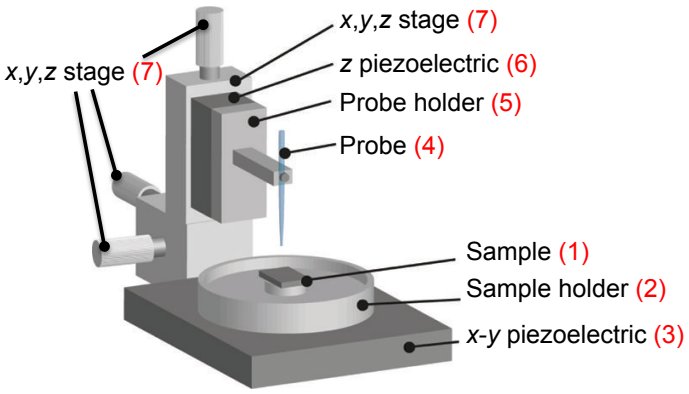

(A) Schematic of the SECCM setup, including probe and sample holders and positioners.

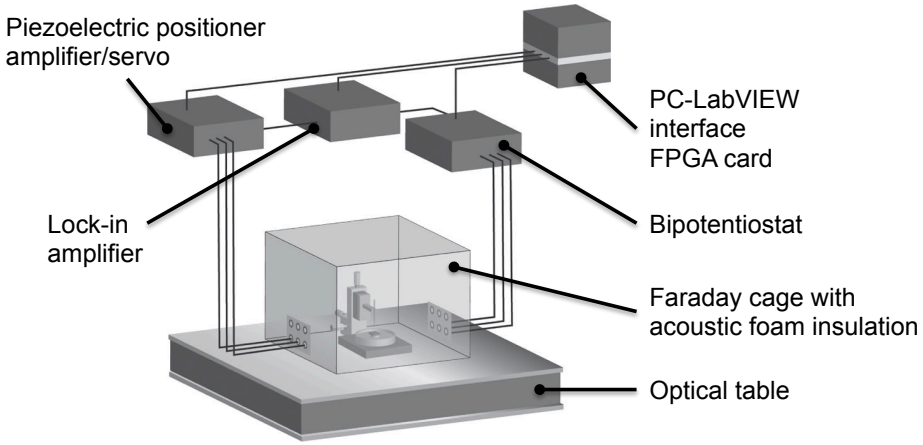

(B) Schematic overview of the whole setup (full instrumentation).

FIGURE 2.5: Scanning electrochemical cell microscopy setup (adapted from [114]).

The piezoelectric positioners can be employed in one of two configurations: **sample scanning** (as shown in figure 2.5(A)), where the x and y positioners are mounted beneath the sample holder, or **tip scanning**, where all piezoelectric components (x, y and z) control

the probe holder. The sample scanning configuration allows for greater spatial resolution, whereas tip scanning is preferred when samples are impractical to move (e.g. samples that are too heavy, large or bulky).

The *sample stage* (figure 2.5(B)) is placed inside a custom-made Faraday cage with acoustic foam lining and heat sinks, and mounted on a vibration isolation optical table (BM-8, Minus K., U.S.A.) to minimise noise due to electric, acoustic and vibrational interference.

The instrument is controlled from a personal computer (PC) with a data acquisition (DAQ) or field programmable gate array (FPGA) card (piezoelectric positioners) and a bipotentionstat (electrochemical signals), through custom-made LabVIEW programmes, as shown schematically in figure 2.5(B). A lock-in amplifier can be also be connected to the FPGA card or DAQ array to generate oscillation signals. [114]

Different methods can be employed in order to detect contact between the droplet and sample surface. For a single barrel probe, a potential difference is applied between the QRCE and working electrode during the approach, at which a jump in current, i_{surf}, is expected, but where no conflicting electrochemical reactions occur, which might modify the system. The probe's downward movement is halted when the magnitude of i_{surf} exceeds a pre-determined value. In the case of double-barrel pipettes with two QRCEs, the same methodology can be used, if both E_1 and E_2 are held constant. Alternatively, i_{barrel} can be used to detect contact instead of i_{surf}. In this case, a potential difference is applied to the two QRCEs (E_2), which induces an ionic conductance current, i_{DC}, across the droplet beneath the tip of the probe. (The relative potential of the (semi)conducting specimen is controlled through E_1 and E_2 as described above (eq. 2.2). Typically, E_2 is maintained constant throughout an experiment, whereas E_1 can be fixed (chronoamperometry) or varied (voltametry).) The currents between the QRCEs (i_{barrel}) and at the surface of the substrate (i_{surf}) can be measured independently.

In the case of the dual barrel probe and once the droplet has made contact with the substrate, the alternating current (AC) component, generated by a sinusoidal oscillation of the probe in the z-direction, can be used as a feedback signal to determine the height of the droplet meniscus (figure 2.6). This methodology can be used to obtain topographical information on not only conducting samples, but also semi-conductors and insulators. In the case of (semi)conducting specimens, electrochemical experiments can also be performed, allowing current-time-voltage characteristics to be obtained simultaneously with topography.[112, 120, 121]

Figure 2.6(A) shows typical responses of the AC and DC components of i_{barrel} as a 1 µm-diameter probe filled with a 50 mM KCl electrolyte solution approaches a HOPG surface. The downward speed is 50 nm s^{-1} before contact is made, and decreases to 2 nm s^{-1} after. Before the droplet comes into contact with the sample's surface, both the DC and AC components of the current are constant, with negligible magnitudes. When contact is established, there is a large jump in both components (different magnitudes) due to the deformation of the meniscus. As the probe continues to move toward the HOPG surface, the droplet is pressed between the tip and the sample, causing a slight decrease in i_{DC}, but an increase in i_{AC} due to the reduced meniscus height.[112]

Figure 2.6(B) compares simulated and experimental i_{DC} and i_{AC} as a function of the meniscus height (m_{h}), which are in excellent agreement, and demonstrates how these data can be used to estimate the separation between the tip and substrate. In this study, a 1 µm tip was used (simulated), filled with 50 mM KCl solution, and oscillated at an amplitude of 50 nm and frequency of 70 Hz As the tip moves closer the substrate, i_{DC} decreases and i_{AC} increases with increasing gradient of i_{DC}. [112]

The SECCM probe can be used to make discrete point measurements or, alternatively, it can be scanned laterally, following the surface's topography (using the barrel current as the feedback signal with a θ-pipette). Scan patterns can be defined by the user; for example,

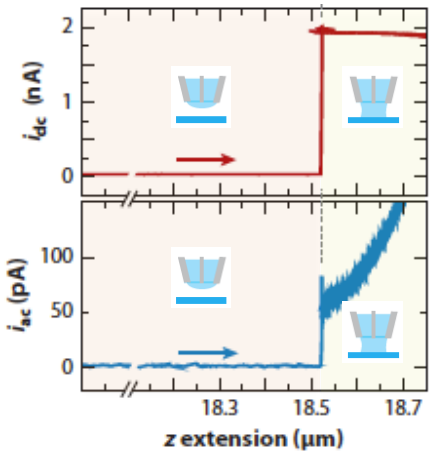

(A) Typical (experimental) responses of i_{DC} and i_{AC} as a probe moves downward toward a conducting surface.

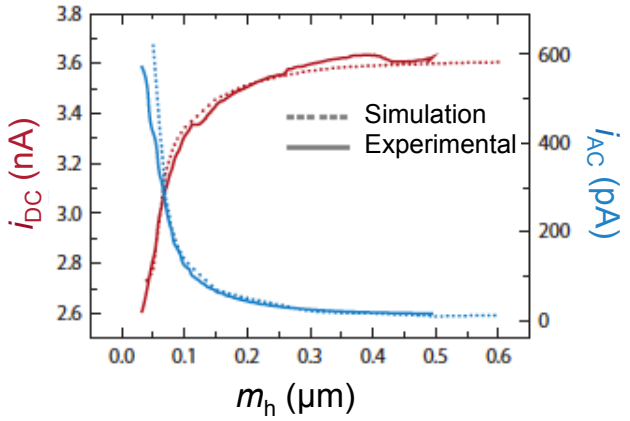

(B) Comparison of simulated and experimental current components i_{AC} and i_{DC} as a function of the meniscus height, m_h.

FIGURE 2.6: Dependence of i_{DC} and i_{AC} on the tip-substrate separation. Adapted from [112].

parallel lines (constant scan), spirals[122] or discrete point measurements have been used. Comprehensive reviews of SECCM can be found in the literature.[112, 114]

2.2.1 Locating SECCM experiments *ex situ*

In order to analyse the effects of the SECCM experiments *ex situ* by microscopes, it is important to locate these areas. Two different strategies have been used in the work presented in this thesis, which are described in the following subsubsections.

2.2.1.1 Inverted Microscope

In a configuration where an inverted microscope with zoom capabilities can be introduced beneath the sample stage, such as the one shown in the schematic illustration in figure 2.7(A), it is possible to see, control, and capture images of the position of the tip relative to both the boundaries of the square it's on and relative to the centre of the TEM grid (*vide* figure 2.7(B)). The centres of TEM grids have asymmetrical features, such as the ones shown in figure

2.7(C), which permits the unambiguous identification of every square in its mesh. Images taken from the inverted optical microscope at a higher magnification, showing clearly both the tip and the edges (and corners) of the square where it is being landed, can then be used to calculate coordinates of the position of the probe in relation to the corners of the square.

For *ex situ* characterisation of the SECCM experiments, for example in STEM, the procedure is repeated in reverse order to find the tip-landing location again: first, the centre features of the TEM grid are identified, and the correct square located. Then, the coordinates of its corners are registered, and the STEM coordinates are obtained by translating the relative coordinates that were calculated previously. The resulting "final" coordinates have some error associated to them, typically of a few microns. However, if the SECCM experiments leave a visible residue/footprint, this method allows for the correct position to be located relatively quickly.

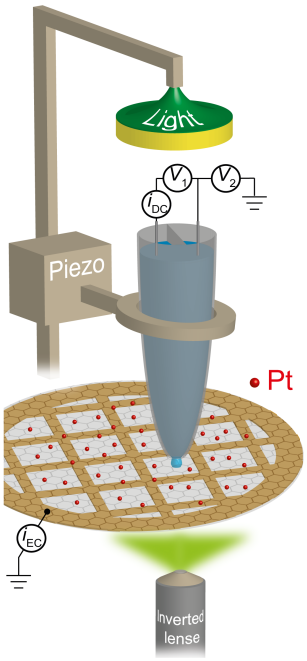

(A) SECCM setup with inverted microscope. Image obtained from [123].

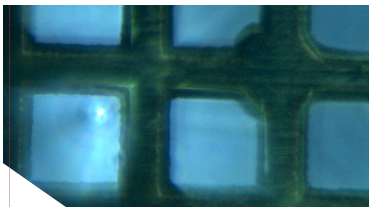

(B) Image taken with from the inverted microscope including the tip location and the centre of the TEM grid.

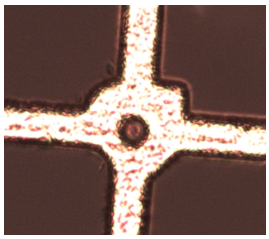

(C) Detail of the assymetrical features at the centre of a TEM grid.

FIGURE 2.7: (A) SECCM setup with inverted microscope, and **(B)** and **(C)** micrographs of TEM grids.

In addition to the method described above, salt markers can be deposited near areas of interest. Figure 2.8(A) shows a NaCl crystal that was left on the CCTG's surface after a SECCM tip (≈1 µm diameter), filled with 0.5 M NaCl solution, was landed and held in contact with the substrate for 60 s, then lifted. The NaCl is resistant to the electron beam at low magnifications, however, when the beam is highly focused, it "dissolves" the crystal, revealing the Pt clusters beneath it (figure 2.8(C)), and leaving behing a "hole" in the crystal (figure 2.8(B)). Due to this behaviour, the salt "markings" can easily be distinguished from other large, bright features in the STEM (e.g. contamination).

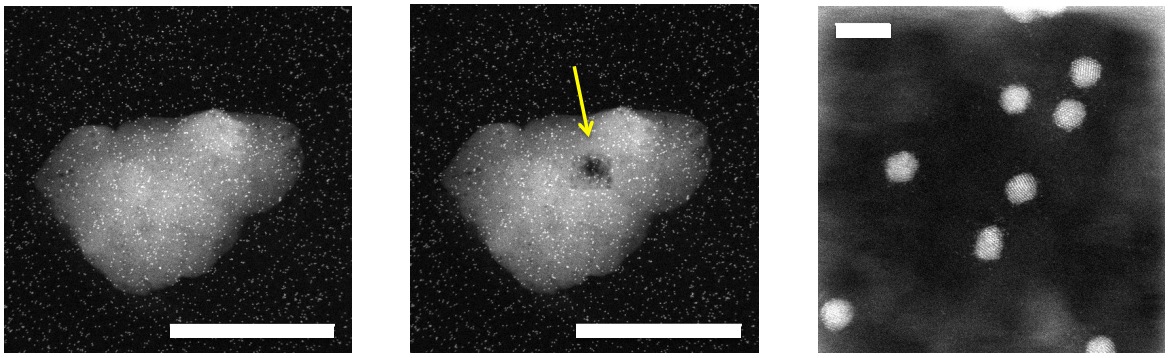

(A) NaCl crystal. The scale bar indicates 300 nm.

(B) NaCl crystal after exposure to the electron beam at high magnifications. The scale bar indicates 300 nm.

(C) High magnification image of Pt_{923} "under" the NaCl crystal. The scale bar indicates 5 nm.

FIGURE 2.8: HAADF-STEM images of a NaCl marker on a sample of Pt_{923} clusters on a CCTG.

2.2.1.2 Breaking the Carbon Film

Using a setup with environmental control prevents the use of an optical microscope beneath the sample stage, which would allow control over where the SECCM tip lands in relation to the TEM grid, as well as recording the tip position as described in the previous section. It is therefore necessary to visualise the grid by an alternative way. This can be

accomplished by creating a topographical map of (a region of) the TEM grid prior to starting experiments.

This is achieved by using a "hopping" programme to raster over a wide range in the *x* and *y* directions. Briefly, the process is as follows: The tip begins above the sample's surface, not touching it. A potential is set for the approach as before (so that a jump in current will be provoked when the droplet touches the substrate, but at which no electrochemical reaction will occur). The tip is then sequentially lowered onto the substrate at determined *x, y* coordinates, lifts back up as soon as the current increase is detected, moves to the next location in the *x, y* plane, and the process is repeated until the entire pre-defined area is covered. The coordinates of the probe (*x, y* and *z*) as well as current and tip potential are recorded throughout.

In this work, the full range of the piezo elements (300 µm × 300 µm), and hop distances of 7.5 µm were used. Figure 2.9(A) shows a topography map created following this methodology.

Locations for the experiments are chosen based on the features that are made visible through this map. For this work, the experiments were performed close to the centre of the squares in the TEM grid (green lines in figure 2.9(A)).

After the experiments are concluded, a set of 3 unused squares, forming an asymmetrical pattern, are chosen to be damaged from the "map" (circled red crosses in figure 2.9(A)). The carbon film on these squares is damaged by driving the probe through them, creating a hole which inevitably grows. Figure 2.9(B) shows an optical micrograph of a TEM grid after this procedure. The centre of the grid is also visible (green circle), which permits the unambiguous identification of the square where the experiments of interest were performed (orange square in the schematic map in figure 2.9(C)), which allows the *ex situ* analysis of the SECCM experiments.

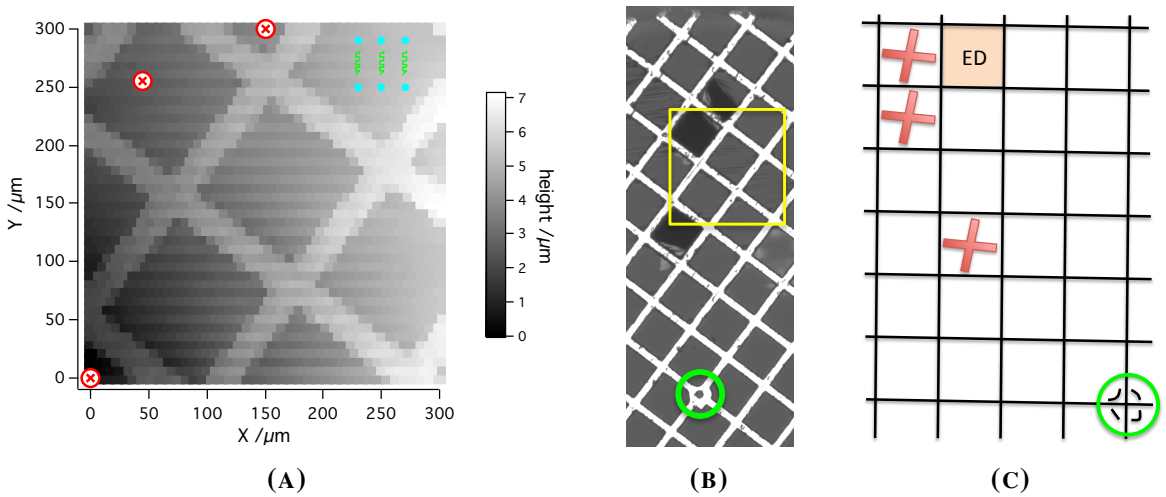

FIGURE 2.9: **(A)** Topography map obtained with SECCM. The red encircled crosses mark the positions where the tip was punched through the carbon film, the orange lines and blue dots indicate where the ED experiments were performed and where markers were placed, respectively. **(B)** Optical micrograph and **(C)** schematic map of the TEM grid, including the centre of the grid (green circle) and the area in **(A)** (yellow square). In **(C)**, the red crosses indicate the squares with damaged carbon and the orange square is where the electrodeposition experiments were carried out.

2.2.2 SECCM Workstations

Localised electrochemical experiments were performed in two different home-built scanning electrochemical probe microscopy workstations (WS) in the WEIG labs. For simplicity, the workstation used for the work presented in chapters 3 and 4 will be referred to as the "ORR-WS" and "ED-WS", respectively. A FPGA card (PCIe-7852R) and a LabVIEW (National Instruments, U.S.A.) interface running Warwick Electrochemical Scaninng Probe Microscopy (WEC-SPM) software (www.warwick.ac.uk/electrochemistry) was employed in both cases to control the equipment and acquire data.

Both workstations have a sample scanning configuration, employing an *xy*-piezoelectric positioner (ORR-WS: P-622.2CL PIHera, Physik Instrumente; ED-WS: Nano-Bio300, Mad-CityLabs, U.S.A.) underneath the sample stage, and a *z*-piezoelectric positioner (P-753.1CD LISA and P-753.3CD, Physik Instrumente, Germany, for the ORR-WS and ED-WS, respec-

tively; both having a 18 µm range) behind the probe holder. A coarse approach was carried out with the help of a picomotor (Newport, 8303 Picomotor Actuator in both cases).

For the work described in chapter 3, the experiments were conducted in contact to air. For the electrodeposition experiments in chapter 4, the TEM grid substrate was mounted inside a custom environmental cell, which was continuously purged with humidified high-purity, argon gas. After exiting the environmental cell, the gas was passed through a bubbler, ensuring that the cell was a closed system. A more detailed description of the environmental cell can be found in the literature.[118]

Data was set to be acquired every 2.56 ms (10 µs per data point, averaged 256 times) and 516 µs (516 µs, averaged 128 times) for the measurements executed at ORR-WS and ED-WS, respectively. The resulting data acquisition rates were $\approx$390 s^{-1} and 1938 s^{-1}, respectively.

2.2.3 Chemical Reagents and Electrode Materials

All solutions were prepared with deionised water (Integra HP, Purite, U.K., resistivity = 18.2 MΩ at 25 °C). All reagents were used as supplied by the manufacturer.

Amorphous carbon-coated 200-mesh gold TEM grids (C200Au, EM Resolutions, U.K.) were used as the working electrode (WE) for all SECCM experiments reported in this thesis, and are referred to here as CCTGs (carbon-coated TEM grids). For each experiment, a TEM grid was mounted in a home-built holder (for the work discussed in chapter 3) or in an aluminium TEM grid holder on SEM pin stub (Agar, U.K., product code AGG3662) (chapter 4).

The SECCM probes were shaped using a CO_2-laser puller (P-2000, Sutter Instruments, U.S.A.). Solution was introduced into the pipettes with MicroFill syringes (World Precision Instruments Inc., U.S.A.). For the experiments presented in chapter 4, a thin layer of silicone oil (DC 200, Sigma-Aldrich) was applied on top of the solution to minimise its evaporation.

For the work described in chapter 3, dual-barrel borosilicate capillaries (TGC 150-10, Harvard Apparatus, U.S.A.), pulled to generate a tapered tip with a diameter of ≈1 µm, were used to fabricate the SECCM probe. Two Pd wires (0.25 mm diameter, purity >99.95%; MaTecK GmbH, Germany) were used to prepare Pd−H_2 QRCEs by applying −3.0 V for 30 min in 0.1 M $HClO_4$ solution before being iserted into the barrels of the pipette.

For the electrodeposition experiments (chapter 4), the probes were shaped from single chamber, borosilicate filamented capillaries (GC120F-10, Harvard Apparatus, U.S.A.) to obtain tips with an inner diameter of 1.6 µm. One platinum wire ($d = 0.25$ mm, Goodfellow, U.K.) was used as the QRCE, cleaned by fame annealing with a Bunsen burner before use. The potential of the Pt QRCE was calibrated in the solution of interest against a commercial leakless Ag/AgCl electrode (3.4 M KCl, ET072, eDAQ, Australia), which has a theoretical potential of +0.206 V *vs.* the standard hydrogen electrode (SHE). The Pt QRCE had a stable potential of (+0.55 ± 0.01) V *vs.* Ag/AgCl (3.4 M), equivalent to +0.756 V *vs.* SHE

The experiments reported in chapter 3 were performed using air-saturated 0.1 M $HClO_4$ (70%, Acros Organics) electrolyte solution. The effect of H_2O_2 was assessed employing the same electrolyte solution, but with the addition of H_2O_2 in concentrations ranging between 1 and 5 mM. The electrochemical cleaning procedure described in section 3.2.1 was executed by immersing most of the TEM grid into 0.1 M $HClO_4$ solution and carrying out CVs between −0.29 and +1.05 V *vs.* Ag/AgCl (*ca.* −0.08 and +1.26 V *vs.*Pd/H) at $\nu = 0.5\ \mathrm{V\,s^{-1}}$. A 3-electrode cell was employed, with a commercial Ag/AgCl reference electrode (3.4 M, ET072-1, eDAQ, Australia) and a Pt wire counter electrode. The SECCM LSVs performed before and after cleaning were carried out using a pipette with $d \approx 500$ nm.

The electrodeposition solution was composed of potassium tetrachloroplatinate(II), $K_2[PtCl_4]$ (Sigma-Aldrich, 99%), diluted to 1 mM, in 0.1 M hydrochloric acid (HCl, VWR, 37%).

2.3 Scanning Transmission Electron Microscopy

The scanning transmission electron microscope (STEM) works by scanning a focused electron beam (the probe) over a sufficiently thin specimen, and an image is formed by collecting the desired transmitted signal.[124] One of the main challenges for electron microscopes has been the imperfection of electron lenses, which unavoidably introduce aberrations that limit the microscope's resolution. The introduction of spherical aberration correction (C_s) allows the generation of smaller electron probes with higher currents, which has greatly improved the sensitivity and spatial resolution of the STEM. Today, scanning transmission electron microscopes are among the most powerful tools for the characterisation of materials at the nanoscale (<1 nm to $\approx$100 nm).

Figure 2.10 shows a simplified schematic of the components of a dedicated STEM with aberration correction, such as the one in NPRL. Electrons are generated from a source and accelerated through a set of condenser lenses, the aberration corrector and an objective lens, to be focused into a point on the sample. Multiple detectors can be used to form an image, either alone or simultaneously.

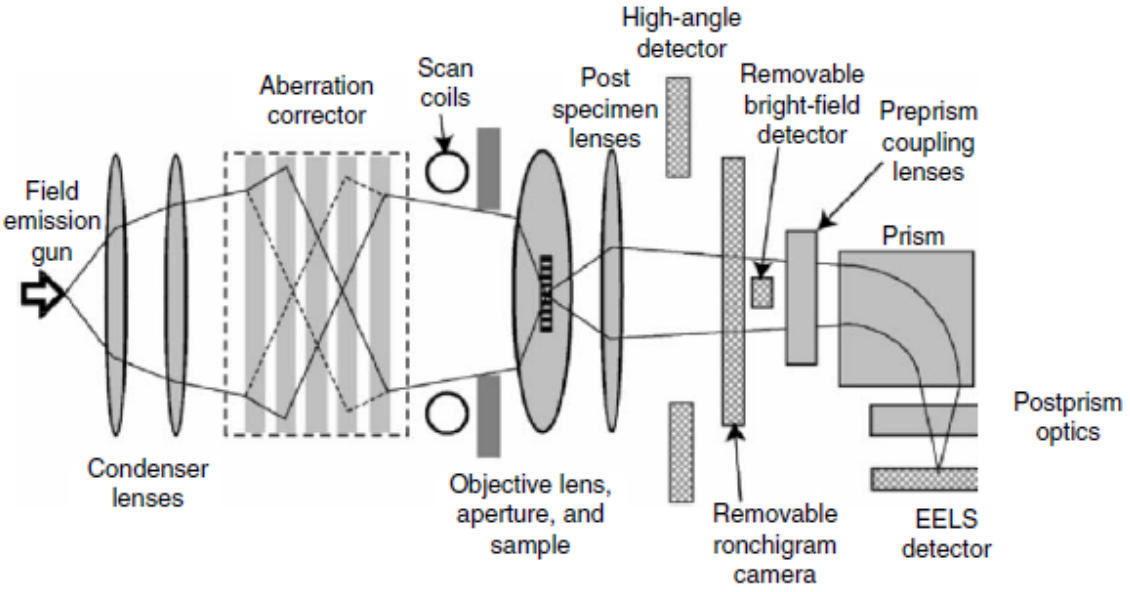

FIGURE 2.10: Schematic of the components of an aberration-corrected STEM. Image taken from [125, 126].

Electrons are generated by an electron source, usually a thermionic gun or a field-emission gun (FEG). In this case, a ZrO/W Schottky field-emission gun is used. The FEG consists of a fine needle (or "tip") and electrons are produced when a strong electric potential is applied between it and two anodes,causing electrons to be extracted from the tip (first anode) and accelerated (second anode).It is vital that the surface of the tungsten needle be free of contaminants and oxide, it must therefore be kept in ultra-high vacuum (UHV) (at room temperature) or in high vacuum (HV) and heated. FEGs produce an electron beam that is brighter, more coherent and monochromatic than thermionic guns, which is especially important for the STEM.

Spherical aberration is caused because the lens field in magnetic lenses is stronger the further off-axis it is, as illustrated in the ray diagram in Figure 2.11. The result is that a point object is imaged as disk of finite size, surrounded by a halo of decreasing intensity; this degrades detail and limits resolution.[127] It is now possible to correct for spherical aberration by forcing the rays to re-converge.[128, 129]

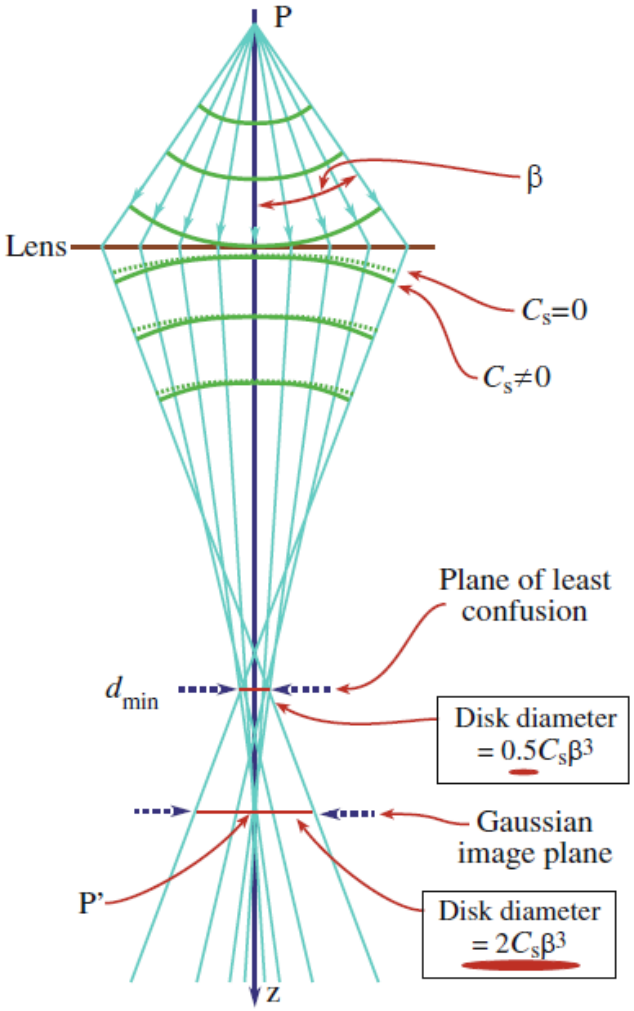

FIGURE 2.11: Spherical aberration; image taken from [127].

When the electron beam interacts with a thin specimen, the electrons can be scattered in different ways, and the transmitted electrons can be collected at different angles, as shown in Figure 2.12. Collection of the direct beam results in coherent, phase-contrast bright-field (BF) images; these are formed by mass-thickness and diffraction contrast: areas that are thicker (assuming constant composition), or that have higher-mass (higher atomic number, Z) (assuming constant thickness) or that are of high crystallinity will be darker.

Annular dark-field (ADF) images are formed by incoherent, elastically scattered and coherent, diffracted electrons. Collecting electrons that have been scattered to high angles, >50 mrad (≈ 3 deg), the effect of Bragg scattering (by electron clouds) is minimized, and

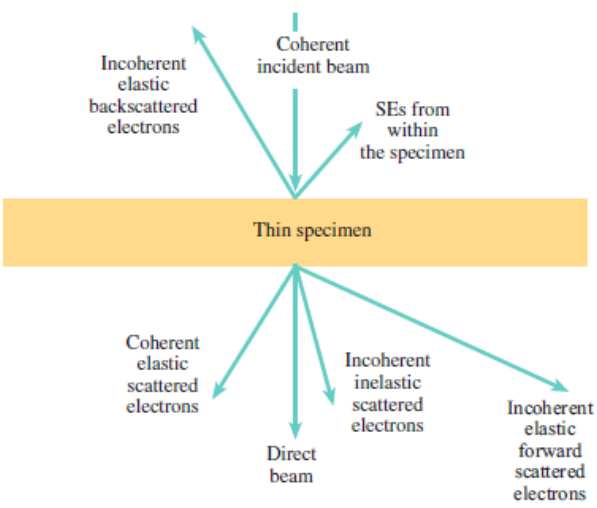

(A) Different kinds of electron scattering (both backward and forward) from a thin specimen.

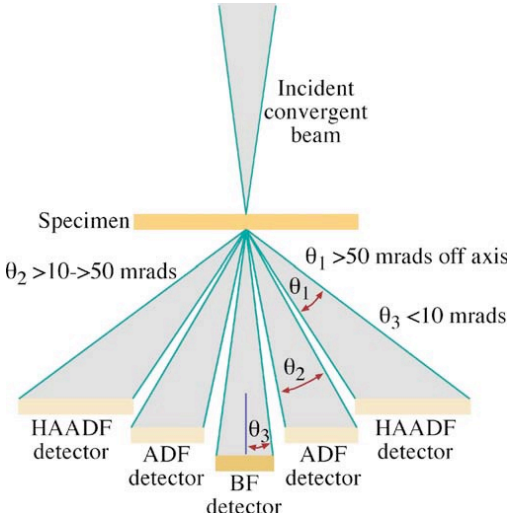

(B) Schematic of the different detectors (BF, ADF, HAADF) for STEM imaging and the range of electron scattering angles gathered by each of them.

FIGURE 2.12: Different types of electron scattering, angles and STEM detectors. Figures adapted from [127].

it can be assumed that Rutherford scattering (by the nuclei) is the dominant phenomenon. These high-angle ADF (or HAADF) images are also called Z-contrast images, because the intensity is proportional to the atomic number, Z, and to the thickness of a sample, t, according to the relation:

$$I \propto t \cdot Z^{\alpha} \tag{2.3}$$

(mass-thickness contrast), where the exponent α is ideally 2 (usually $1 < \alpha \leqslant 2$ in experimental conditions). The use of HAADF imaging makes it possible to "count" atoms in clusters; it has been shown experimentally that the relationship between the HAADF integrated intensity and the size of the cluster is linear for up to $N = 1500$ atoms.[130] It can also be used to calculate the size of clusters made of more than one element (if the composition is known), using the relation:

$$\frac{I_A}{I_B} = \left(\frac{Z_A}{Z_B}\right)^{\alpha} \tag{2.4}$$

The value of α has been calculated experimentally for our STEM using size-selected Au_{923} and Pd_{923} clusters and it was found to be $\alpha = 1.46 \pm 0.18$ for an inner collection angle of 62 mrad.[131]

2.3.1 Operation Conditions

The samples in this work were imaged and characterised by scanning transmission electron microscopy employing a spherical aberration (C_s) corrected (CEOS, Germany) JEM-2100F field-emission electron microscope (JEOL, Japan), with a beam acceleration of 200 kV. Unless stated otherwise, the images were obtained using inner and outer collection angles of 62 and 164 mrad, respectively, a convergence angle of 19 mrad (camera length of 10 cm), an image resolution of 512^2 pixels, and a pixel dwell time of 38 µs (corresponding to 10.0 s per image).

The equipment was operated using DigitalMicrograph software (Gatan, U.S.A.[132]).

2.3.2 Magnifications

Throughout the work described in this thesis, the STEM was used in SM-MAG mode. The magnifications utilized range from 20k to 15M. Table 2.1 lists the magnifications that were routinely used during the works described here, as well as the resulting image widths.

For the work described in chapter 3, all statistical analysis was performed on 2 M or 1 M images, unless stated otherwise. In chapter 4, different magnification ranges were used and referred to as described below:

Very low (20k - 50k): overview of entire droplet footprint; estimation of the droplet areas. **Low (100k - 500k):** statistical information about the particles (including particle number density, size and spatial distributions). **High (1M - 5M):** structural information

about medium-sized and larger NPs. **Very high ($\geq$ 10M):** atomistic information; presence of single atoms.

TABLE 2.1: Magnifications used routinely for recording HAADF-STEM images throughout the work presented in this thesis, including the respective image width and nominal pixel area (for images with 512^2 px).

Magnification	Abbreviation	Image Width	Nominal Pixel Area
20×10^3	20k	7.87 µm	2.36×10^2 nm^2
50×10^3	50k	3.15 µm	3.79×10^1 nm^2
100×10^3	100k	1.57 µm	9.40 nm^2
250×10^3	250k	0.63 µm	1.51 nm^2
500×10^3	500k	315 nm	3.79×10^{-1} nm^2
1×10^6	1M	157 nm	9.40×10^{-2} nm^2
2×10^6	2M	78.7 nm	2.36×10^{-2} nm^2
3×10^6	3M	52.5 nm	1.05×10^{-2} nm^2
5×10^6	5M	31.5 nm	3.79×10^{-3} nm^2
10×10^6	10M	15.7 nm	9.40×10^{-4} nm^2
15×10^6	15M	10.5 nm	4.21×10^{-4} nm^2

2.4 Image Analysis

The STEM images were analysed using the ImageJ2 software package (FiJi distribution).[133] The ImageJ programming language was employed to automatise as much as possible through the use of custom-written programmes, or "macros". As a rule, each programme opened an image from a specified folder, waited for the user to adjust the intensity threshold, then automatically identified and analysed the particles according to its programme, and saved the required outputs. This was repeated for all images within the

folder. Information obtained from each image included the 2D projected area, perimeter, integrated HAADF intensity, centre of mass and parameters of the best fitting ellipse (centre coordinates, major and minor semi-axes, angle) for each particle. Generally, each macro ran twice over each image, to extract this data when including and excluding edge-touching particles.

2.4.1 Atom Counting

The platinum in individual NPs was estimated by using the HAADF integrated intensity of single Pt atoms as "weights" to calibrate that of particles and nanoclusters.

Simple ImageJ macro programmes ("macros") were written in order to automatise as much as possible in the process, and measures were taken with the objective of reducing user-associated errors.

To estimate the amount of platinum in each particle and in the meniscus footprint as a whole, the first requirement was to obtain a "weight" with which to calibrate the HAADF intensities of particles in the STEM images. For this purpose, the background-corrected HAADF intensities of ≈200 single Pt atoms were calculated using very high magnification (15M) images, in order to obtain statistically significant single-platinum intensity value.

The carbon-platinum boundaries were defined by manually setting an intensity threshold (using ImageJ's *threshold* function) for each image. This allowed all Pt atoms and clusters to be identified, their areas calculated, and two concentric ellipses to be drawn surrounding each platinum-containing species (called "object" from here onwards), as demonstrated in figure 2.13(C).

Information was collected from each object defined by the thresholding function, including its area, equivalent radius, centre of mass, and parameters for the best fitted ellipse (centre, semi-major and semi-minor axes). These were then used to draw the ellipses around

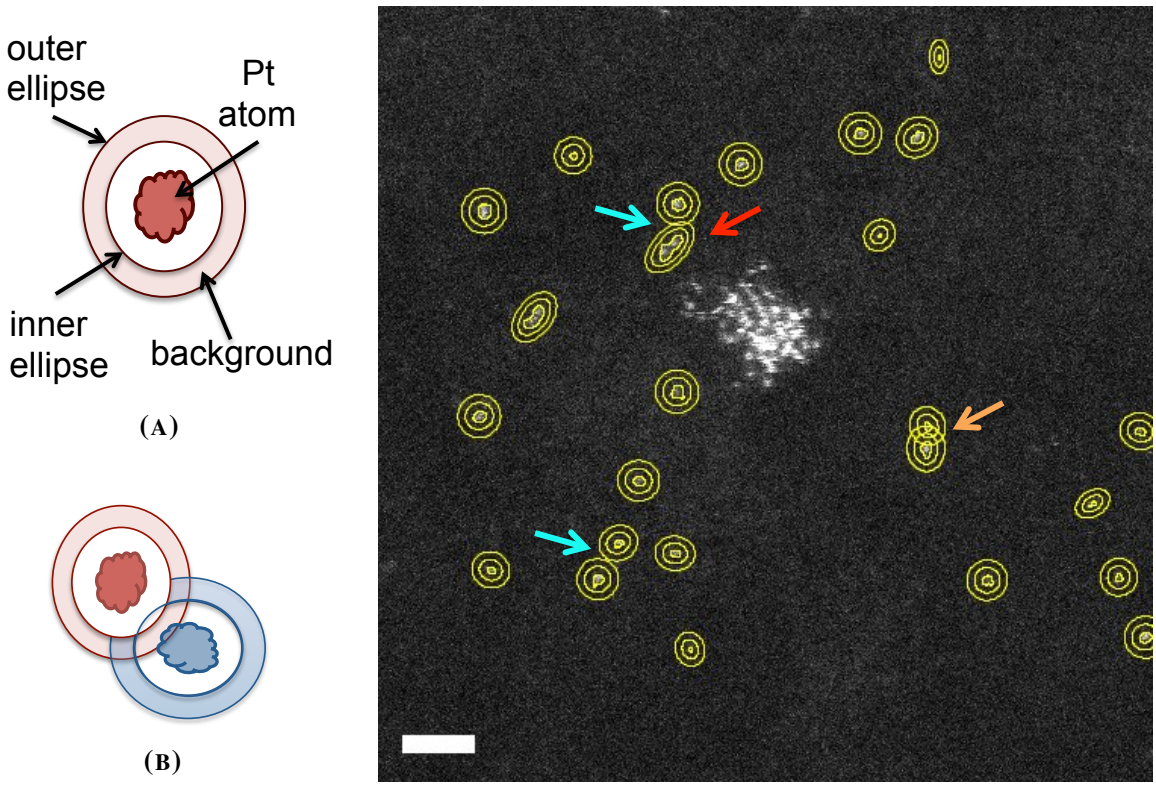

FIGURE 2.13: **(A)** and **(B)**: Schematic diagrams showing Pt atoms surrounded by concentric ellipses: **(A)** single Pt atom, **(B)** two Pt atoms with overlapping inner ellipses. **(C)** Representative high magnification image showing a small, amorphous cluster and surrounding single platinum atoms. The red, orange and blue arrows indicate, respectively, a dimer, single atoms with overlapping inner ellipses, and atoms that are close but with no overlap. The scalebar represents 1 nm.

each object. The same lengths (ΔL_1 and ΔL_2) were set between the radius of the object and the semi-major axis of the inner ellipse (ΔL_1), and between the semi-major axes of the inner and outer ellipses (ΔL_2) for every object in one image, but these lengths could be manually adjusted for each image independently of each other.

The integrated intensity within the area delimited by the two ellipses (pink area in figures 2.13(A) and 2.13(B)) was used to obtain the background intensity density surrounding each object as follows:

$$ID_{\mathrm{BG}} = \frac{(II_{\mathrm{e2}} - II_{\mathrm{e1}})}{(A_{\mathrm{e2}} - A_{\mathrm{e1}})} \tag{2.5}$$

where the symbols A, II and ID represent the area, integrated intensity and intensity density, respectively. The subscripts e1 and e2 indicate the inner and outer ellipses, respectively, and BG signifies background.

The background-corrected integrated intensity for each platinum atom (II_{Pt}) was calculated from the area enclosed by the inner ellipse to minimise the error associated with the manual thresholding:

$$II_{\mathrm{Pt}} = II_{\mathrm{NP}} - ID_{\mathrm{BG}} \cdot A_{\mathrm{e1}} \tag{2.6}$$

In the case of neighbouring atoms whose inner ellipses have some overlap, such as in figure 2.13**(B)**, any overlapping area was excluded from further calculation. For example, considering the blue atom in figure 2.13**(B)**, only the visible part of the blue disk would be used to calculate its background's intensity density, and only the portion of its inner ellipse that is untouched by the red inner ellipse would be used to extract this atom's area and intensity.

Atoms which touched or overlapped with the inner ellipse of a neighbouring object, as well as dimers, were discarded (e.g. the objects indicated by the orange and red arrows in figure 2.13**(C)**).

The background-corrected intensities of all suitable single Pt atoms were plotted as a histogram, and a Gaussian fit was optimised. The peak location was used as the single atom intensity for further calculations (see figure 2.14).

2.4.2 Measuring Projected Areas

The determination of projected areas of Pt NPs reported in chapter 3 was carried out employing custom-written ImageJ macros, as described at the beginning of this section (section 2.4), with the intensity thresholds being set manually for each image.

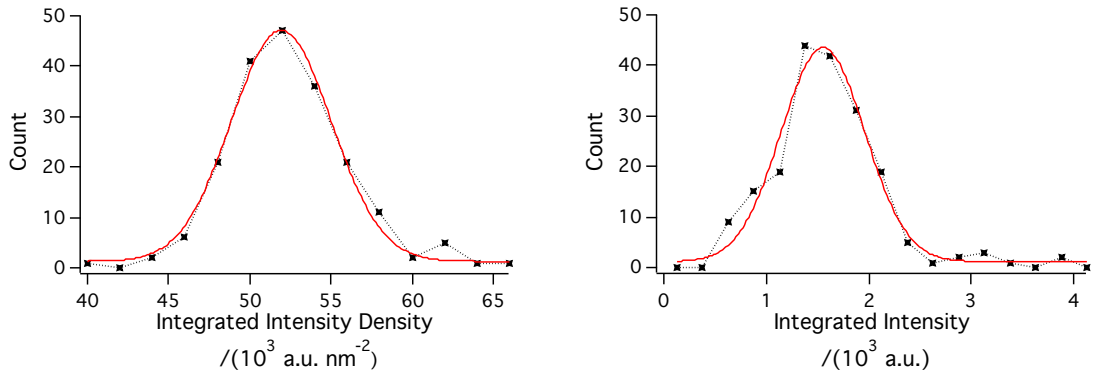

(A) **(B)**

FIGURE 2.14: Histograms of **(A)** the background integrated intensity normalised by area (nm^2) and of **(B)** the integrated intensity of a single platinum atom. Black markers with dotted lines indicate the experimental data and the red curves correspond to the Gaussian fits.

The most suitable value for the intensity threshold can depend on factors such as the image magnification, the particle density on the image, the size of the particles, the particles' maximum intensities, the background intensity, and the ratio of pixel size to particle size. For this reason, determining the projected areas of objects from HAADF-STEM images is not trivial, and setting the boundaries for the particles is a subjective process, which can introduce some error, as well as increase the variation of, for example, the particle diameter in samples with high homogeneity (e.g. the Pt_{923} samples studied in chapter 3).

With this in mind, very high magnification images of size-selected Pt_{923} clusters were analysed, in order to estimate the "real" mean cluster size, and to ensure that the projected areas obtained from lower magnification images were accurate. The aims of this analysis were to identify and minimise subjective bias in measuring the projected cluster area / cluster diameter. ImageJ macro programmes were written and employed to minimise user input and associated error. The steps for each analysed 10 M image were the following:

1. The noise in the image was reduced by applying a soft filter ("mean", radius = 2).

2. A threshold was set manually, and the resulting shape delimiting the clusters was saved.

3. The image was reverted into the original and cluster parameters were measured, including the centre of mass coordinates, (X_{CM}, Y_{CM}).

4. Centred at (X_{CM}, Y_{CM}) for each cluster, 6 lines were drawn at different angles, in 30° steps (as shown in figure 2.15(A)).

5. The "length" of the cluster along each line was calculated at different intensity percentages relative to the cluster's background-corrected maximum intensity (horizontal lines in figure 2.15(B)).

6. The average of the cluster lengths calculated in the previous steps is taken as the cluster diameter.

This is illustrated in figure 2.15. Figure 2.15(A) shows a 10 M image with two clusters, each is overlayed by the 6 lines through its centre of mass. Figure 2.15(B) shows the plot profiles along the lines on the cluster NC1. The three horizontal lines indicate, from bottom to top, 15%, 20% and 25% of the cluster's background-corrected maximum intensity.

It is important to point out that the threshold set in step 2 does not affect the diameters obtained for the clusters in step 5, as it was only used to obtain the centre of mass for each cluster.

As expected, the thresholds set in step 5 (indicated by the horizontal lines in figure 2.15(B)) all fall within the regions in the plot profile where the intensity has the steepest slopes (at the edges of the clusters), and identifying a precise intensity boundary would be very difficult with only the naked eye. The results for this analysis of high magnification images are summarised in table 2.2. It can be seen that the thresholded diameter

($d_{thr} = 3.22 \pm 0.11$ nm) is only slightly less than that obtained at 15% of the cluster intensity ($d_{15\%} = 3.24 \pm 0.14$ nm).

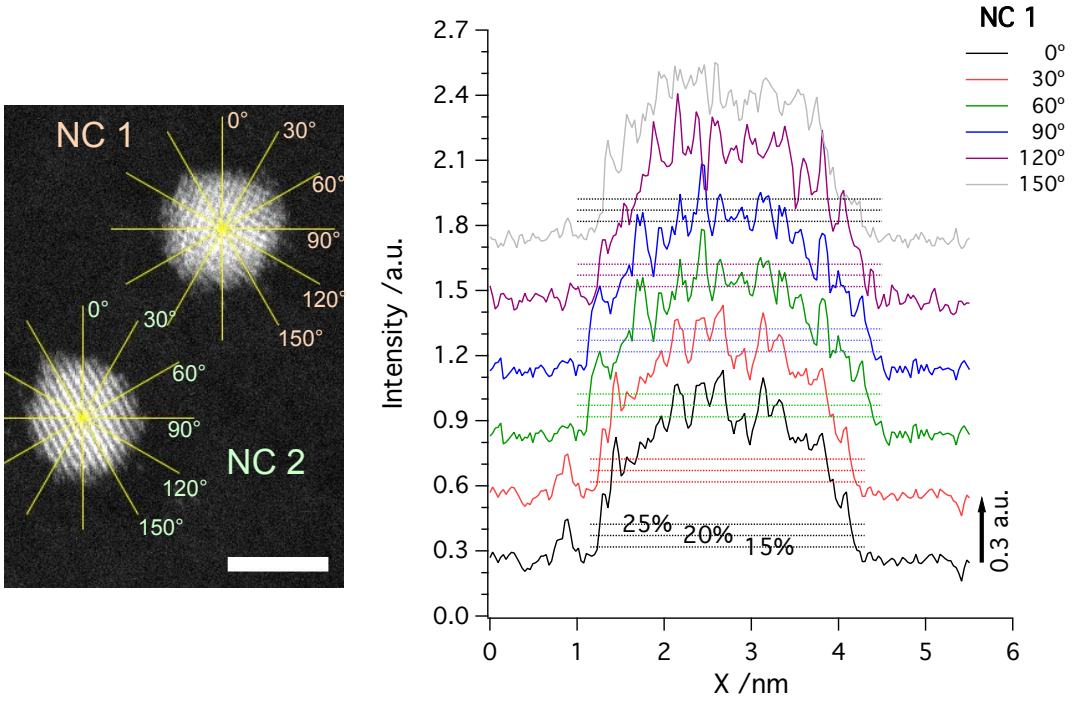

(A) (B)

FIGURE 2.15: A) Very high magnification (10 M) image of two Pt_{923} clusters (NC1 and NC2), overlayed with lines which cross the clusters' centre of mass at different angles. **B)** Line profiles for NC1. Each line plot is shifted vertically by 0.3 a.u. relative to the previous plot. The dotted horizontal lines indicate 15%, 20% and 25% of the cluster's background-corrected maximum intensity.

TABLE 2.2: Diameters of Pt_{923} clusters obtained from 10 M images. The values for A_{thr} and d_{thr} were obtained by setting an intensity threshold manually; the remaining diameters were obtained from the plot profiles of the clusters.

Cluster	A_{thr} /nm^2	d_{thr} /nm	$d_{15\%}$ /nm	$d_{20\%}$ /nm	$d_{25\%}$ /nm
1	7.92	3.17	3.18 ± 0.09	3.10 ± 0.13	3.01 ± 0.15
2	7.40	3.07	3.11 ± 0.22	2.96 ± 0.19	2.86 ± 0.18
3	8.97	3.38	3.34 ± 0.19	3.19 ± 0.18	3.02 ± 0.16
4	7.46	3.08	3.11 ± 0.30	2.91 ± 0.27	2.79 ± 0.22
5	8.48	3.29	3.16 ± 0.19	3.06 ± 0.14	2.95 ± 0.12
6	8.95	3.38	3.37 ± 0.17	3.19 ± 0.14	3.08 ± 0.11
7	8.58	3.30	3.23 ± 0.20	3.08 ± 0.17	2.95 ± 0.25
8	8.43	3.28	3.52 ± 0.27	3.33 ± 0.21	3.21 ± 0.16
9	7.95	3.18	3.40 ± 0.46	3.21 ± 0.39	3.08 ± 0.29
10	7.71	3.13	3.13 ± 0.15	3.02 ± 0.14	2.93 ± 0.16
11	7.76	3.14	3.13 ± 0.09	3.02 ± 0.10	2.90 ± 0.09
12	8.24	3.24	3.19 ± 0.14	3.08 ± 0.13	2.99 ± 0.13
$d_{av.}$	—	3.22 ± 0.11	3.24 ± 0.14	3.10 ± 0.12	2.98 ± 0.11

These results will be referred to later in this thesis, when discussion the results in chapter 3.

2.4.3 Droplet area

The contact area between the droplet and the CCTG support ("droplet area") for the electrodeposition experiments (chapter 4) was calculated by fitting regular shapes (i.e. ellipses) to the meniscus footprint in 50 k magnification images. This magnification was chosen because it is the highest magnification which encompasses the whole droplet area. This is exemplified in figure 2.16.

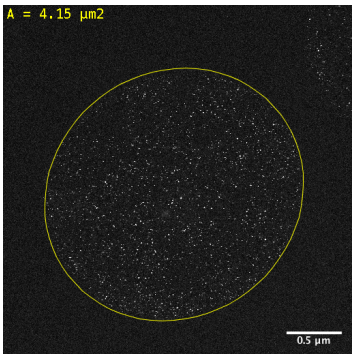

FIGURE 2.16: 50 k-magnification image used to calculate the droplet area. Platinum deposited potentiostatically at $E_{app} = -0.9\,\text{V}$ for $t_{app} = 10\,\text{s}$. The scalebar indicates 0.5 µm.

For the electrodepositions performed for a duration of 10 s, only $E_{app} \leq -0.7\,\text{V}$ resulted in enough deposited platinum to be visible at a very low magnification, (this can be seen very clearly in figure 4.4, in chapter 4). Consequently, only the footprints of the 3 highest overpotentials could be utilised to extract the droplet area.

The contact area between the SECCM droplet and amorphous carbon substrate was calculated to be $4.21 \pm 0.08\,\mu\text{m}^2$, which corresponds to a diameter of $d_{\text{droplet}} = 2.31 \pm 0.02\,\mu\text{m}$. These values represent increases of 209% and 145% relative to the tip area and diameter, respectively.

Chapter 3

Oxygen Reduction Reaction on Carbon-Supported, Size-Selected Pt_{923} Clusters: Poisoning and Mobility of the Pt Catalysts

The work presented in this chapter was done in collaboration with the Warwick Electrochemistry and Interfaces Group (WEIG) under the supervision of Prof. Pat Unwin and it has been published in a peer-reviewed journal.[123] Dr. Guohui Zhang and Dr. Jon Ustarroz executed the SECCM experiments to test the ORR, Dr. Minkyung Kang carried out the whole-grid electrochemical cleaning and the H_2O_2 tests, and Dr. Marc Walker performed the XPS experiments and deconvoluted the spectra discussed in this chapter. The author has prepared all samples and carried out all STEM imaging and analysis. Figures which were not prepared by the author are clearly referenced.

3.1 Introduction

Electrochemical energy conversion and storage plays a vital role in sustainable energy technologies, because it facilitates the conversion of electrical into chemical energy, and *vice versa*. This is especially vital for the storage of energy from renewable sources (wind, solar, etc.) when supply exceeds demand. For example, electrolysis cells use electrical energy to drive nonspontaneous electrochemical reactions, storing it as chemical energy. The inverse process is carried out in fuel cells, where spontaneous electrochemical reactions (oxidation of the fuel and reduction of the oxidant) occur in galvanic cells, transforming the previously stored chemical energy into electrical energy.[134]

The oxygen reduction reaction (ORR) is the cathodic reaction in polymer electrolyte membrane fuel cells (PEMFCs), where O_2 is converted into H_2O or H_2O_2. However, the ORR is the rate limiting reaction in such devices due to its high overpotential and sluggish kinetics, even with the most efficient catalysts (platinum).[135–137]

The state of the art catalysts for the ORR are platinum-based, generally employed as highly dispersed nanostructures on a high surface area, inert support (typically carbon).[134, 136] However, the mechanisms of the ORR are not yet fully understood, and the effect of parameters such as particle size and size dispersity, interparticle distance and catalyst loading are still under discussion.[135, 138] These factors are interrelated and affect stability, selectivity and the reaction pathway (i.e. a $2\,e^-$ (equations (1.3) and (1.4)) or $4\,e^-$ (equation (1.2)) mechanism). Furthermore, the practical application of catalysts for the ORR faces significant challenges, especially regarding resistance to degradation of the catalyst systems under FC working conditions.[139]

In most experimental studies about the catalytic activity of Pt NPs toward the ORR, there is little control over particle size distribution and loading, and separating the effects of these two parameters becomes very difficult. However, recently, subtle differences in the spatial

distribution, size and loading of Pt nancocluster catalysts have been shown to significantly affect their activity and selectivity.[54, 59, 140–142]

In this work, SECCM was employed to test the electrocatalytic activity and stability of mass-selected platinum clusters, Pt_{923} (923 constituent atoms, $d \approx 3$ nm), with a very narrow size distribution (theoretical size dispersion of $\pm$ 4%), which were deposited onto a carbon-coated TEM grid from a cluster beam. The electrochemical investigations were performed in a small area (*ca.* 1 μm^2), containing ≈5000 to 20 000 particles, depending on the sample. The SECCM setup results in a very high mass transport rate for oxygen (≥ 0.1 cm s^{-1}) due to the high surface-volume ratio and the three-phase nature of the droplet cell, which allows additional O_2 to come into the electrolyte solution through the liquid-air interface.[137] The changes in this system were then investigated with *ex situ* HAADF-STEM, which allowed the visualisation of the whole droplet footprint, easily identified by the change in the background HAADF intensity, as well as to obtain images of a large portion of the Pt NCs in the footprint area with subatomic resolution. This permitted the performance of a statistical analysis and comparison of the cluster populations inside such areas and outside. The "outside" areas were untouched by the SECCM probe, and hence can be used as a control, equivalent to "before" electrochemical testing. For the statistical analysis, a minimum of 3 images (> 100 clusters) was used for each condition, i.e. each experiment / footprint and each corresponding "outside" area.

The low platinum loadings ($\leq 0.9\,\mu g\,cm^{-2}$), the carbon support (amorphous carbon film), the high mass transport rates, three-phase configuration (gas-liquid-solid) and wide potential windows employed in this work serve to mimic PEMFC conditions and allow the study of the changes undergone by the system due to the ORR.

3.2 Sample preparation and characterisation

The cluster source, described in section 2.1, allows for independent control of cluster size (mass), coverage (or density), and deposition (impact) energy. In this work, samples were prepared by depositing mass-selected platinum clusters with 923 atoms (Pt_{923}) onto gold TEM grids covered by a thin amorphous carbon film. Two different densities and two different impact energies were chosen, and the three samples studied here are referred to as LD-LIE (low density, low impact energy), LD-HIE (low density, high impact energy), and HD-HIE (high density, high impact energy). The Pt loadings on the samples were chosen so that there would be a ≈10-fold difference between them, while ensuring a good enough signal-to-noise ratio for the electrochemical response of the LD samples, and minimising cluster aggregation for the HD sample.

The characteristics of each sample, including their particle density, surface coverage and platinum loading, are summarised in table 3.1. Representative HAADF-STEM images are shown in figures 3.1(A), 3.1(C) and 3.1(E), and the size distribution (expressed as the clusters' projected area) for each sample is presented in figures 3.1(B), 3.1(D) and 3.1(F). Note the separate peaks in the histograms for monomers (Pt_{923}, referred to as "singlets"), dimers (or "doublets", Pt_{923x2}, formed by the aggregation or merging of two Pt_{923} NCs) and larger particles ("bigger"), generated by the sintering of 3 or more singlets.

TABLE 3.1: Impact energy (E_{impact}), particle density, surface coverage and platinum loading for each of the three samples employed in this study.

Sample	E_{impact} (eV/atom)	Particle Density (μm^{-2})	Surface Coverage	Pt loading $\mu g\,cm^{-2}$
LD-LIE	0.54	5200 - 6100	5.5 ± 1.1%	0.10
LD-HIE	1.6	6300 - 6500	6.1 ± 1.0%	0.10
HD-HIE	1.6	16000 - 20000	36.9 ± 1.9%	0.85

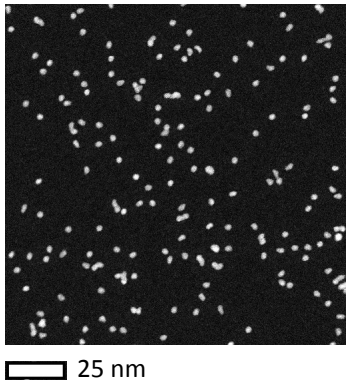

(A) LD-LIE

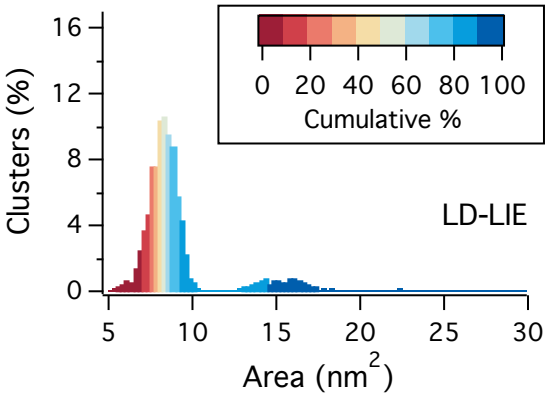

(B) LD-LIE

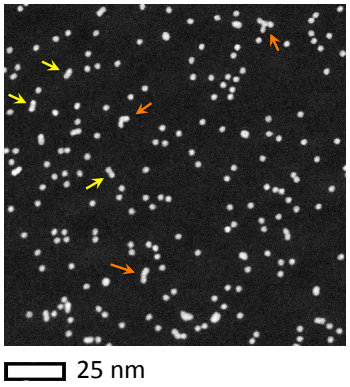

(C) LD-HIE

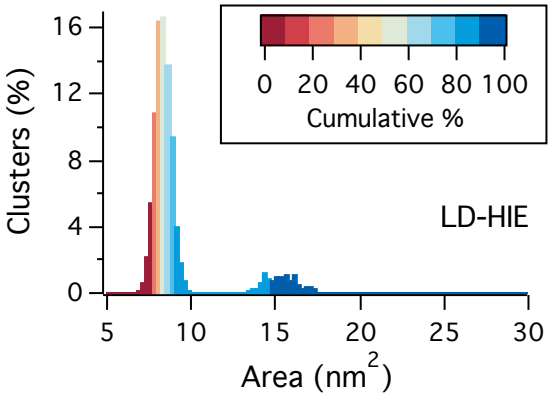

(D) LD-HIE

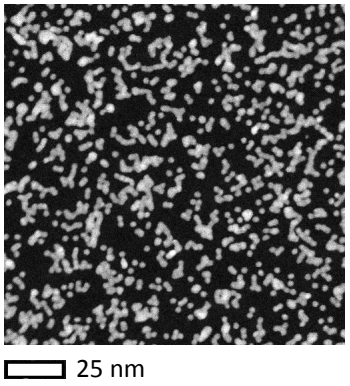

(E) HD-HIE

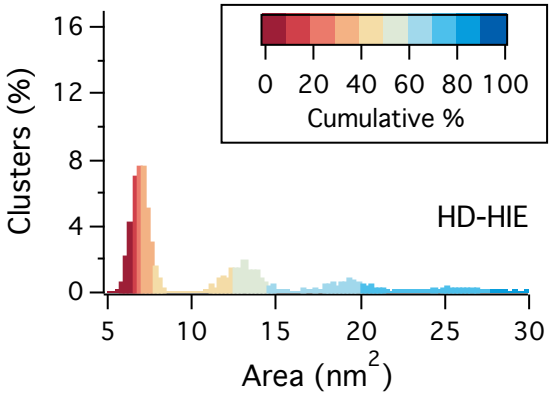

(F) HD-HIE

FIGURE 3.1: **(A)**, **(C)**, **(E)**: Representative STEM images of the three samples in areas where no EC was performed. The yellow and orange arrows in **(C)** point to doublets and bigger aggregated clusters, respectively. **(B)**, **(D)**, **(F)**: Cluster area histograms. The colour scale indicates the cumulative percentage of the clusters at each size.

As described in section 2.1.3, there are three landing regimes: soft-landing, pinning and implantation. Generally, soft-landing occurs when the cluster impact energy is $\lessapprox$10 eV per atom, but the exact value at which the transition into pinning occurs depends on the cluster and substrate. More specifically, a cluster is thought to be soft-landed when its kinetic energy per atom on impact (during deposition) is smaller than the binding (or cohesive) energy of its constituents. This prevents fragmentation of the NC, but deformation of its structure is possible.[107]

For platinum, the experimentally determined binding energies have been reported to be 5.8 eV per atom for a bulk crystal, and between 2.6 and 3.7 eV per atom for the Pt_2 dimer.[143]It is reasonable to assume that the cohesive energy for Pt_{923} will fall between that of Pt_2 and that of bulk platinum. However, even considering the lowest of these reported cohesive energies (2.6 eV/atom), it is significantly higher than the highest impact energy used in this work (1.6 eV per atom). Therefore, all samples prepared for this work should be within the soft landing regime. This is confirmed by the analysis of the HAADF-STEM images of the samples, which show no evidence of cluster fragmentation. Instead, the histograms (*vide* figure 3.1) show distinct Gaussian-shaped peaks for Pt_{923} and its dimers (for the LD samples) and multiples (in the HD sample).

Please note that for the histogram for the high density sample, HD-HIE (figure 3.1**(F)**), only ≈81.3% of the clusters are represented in the included size range. The remaining ≈18.7% of the clusters are larger agglomerated particles, ranging in size (projected area) from 30 to 376 nm^2. For the low density samples, the histograms shown in figures 3.1**(B)** and 3.1**(D)** include 99.8% and 99.6% of all Pt NCs, respectively, and the maximum observed particle projected areas were *ca.* 50 and 37 nm^2 for the LD-LIE and LD-HIE samples, respectively.

It is worth noting that a difference in the morphology of the clusters in the LD-HIE and LD-LIE samples was observed, with the former having rounder shapes (aspect ratios,

AR, closer to 1), and the latter a bigger variation in shape (wider AR distribition). These differences are not obvious to the unaided eye, but they are reflected in the shape descriptors of the NCs, as shown in the aspect ratio histogram depicted in figure 3.2. The different morphologies of the clusters in these samples do not seem to have any effect in their electrochemical response, however, as will be shown in section 3.3.

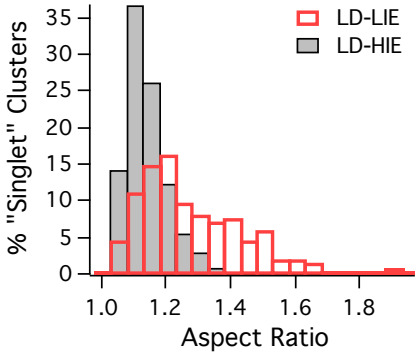

FIGURE 3.2: Aspect ratio of the singlet clusters in the LD-LIE and LD-HIE samples.

3.2.1 Electrochemical Cleaning

Typically, prior to electrochemistry studies employing platinum, the working electrode is cleaned, usually by repeated voltammetric cycling in a wide potential range to include the potentials at which hydrogen is adsorbed onto the Pt surface at the cathodic limit and at which its surface is oxidised at the anodic limit.[144] The potential cycling is generally carried on until consecutive CV cycles are identical, indicating that impurities have been successfully removed from the platinum surface. However, this process can result in changes to the working electrode, which is sometimes undesirable.

For the work presented in this chapter, having a well-defined sample, with randomly distributed clusters of a pre-determined size and narrow size distribution was vital. For that reason, two HIE samples (1.6 eV/atom) were cleaned by electrochemical cycling, in order to evaluate the effect of this process on the size-selected Pt_{923} clusters. A high deposition

energy was chosen for this purpose to ensure a stronger adherence of the NCs to the substrate and reduce cluster mobility. Two different cluster densities, "low" (LD) and "high" (HD), were employed (*vide* table 3.2).

For these experiments, the TEM grid samples were submersed almost entirely into a 0.1 M $HClO_4$ solution and the potential was cycled between -0.29 and 1.05 V *vs.* Ag/AgCl at a scan rate $\nu = 0.5\,\mathrm{V\,s^{-1}}$.

The electrocatalytic activity of the Pt NCs was investigated before and after this cleaning procedure using the SECCM configuration, with a pipette with tip diameter of ≈0.5 µm. Figure 3.3(A) shows linear sweep voltammograms (LSVs) performed on the LD sample, and figure 3.3(B) shows LSVs performed on the HD sample, after cleaning, in two different locations. Representative STEM images of these samples obtained before and after cleaning are depicted in figure 3.4, and table 3.2 summarises the main results from the size analysis performed based on images such as those shown in figure 3.4.

The LSVs obtained before and after cleaning (figure 3.3(A)) reveal (i) a decrease in the ORR onset potential, and that (ii) the apparent limiting current (before the onset of HER) remains broadly unchanged. The onset of the ORR shifts by *ca.* +0.1 V, confirming faster kinetics after the treatment. However, even in the "clean" sample, the overpotential remains larger than those typically obtained in RDE setups with higher Pt loadings, indicating that the large η measured in this study (*vide* section 3.3) are a consequence of the system used herein (i.e. high mass transport due to the SECCM setup and low platinum loading), and not due to contamination of the catalyst surface at the start of the experiments. Furthermore, the cleaning process does not change the limiting currents in our specimens (≈–0.7 pA for the LD sample, figure 3.3(A)), which remain significantly lower than that expected in the diffusion control regime (*ca.* $6\,\mathrm{mA\,cm^{-2}}$, or ≈12 pA for a $4e^-$ process and a working electrode with $d = 0.5\,\mu\mathrm{m}$), even if a $1e^-$ process is considered.

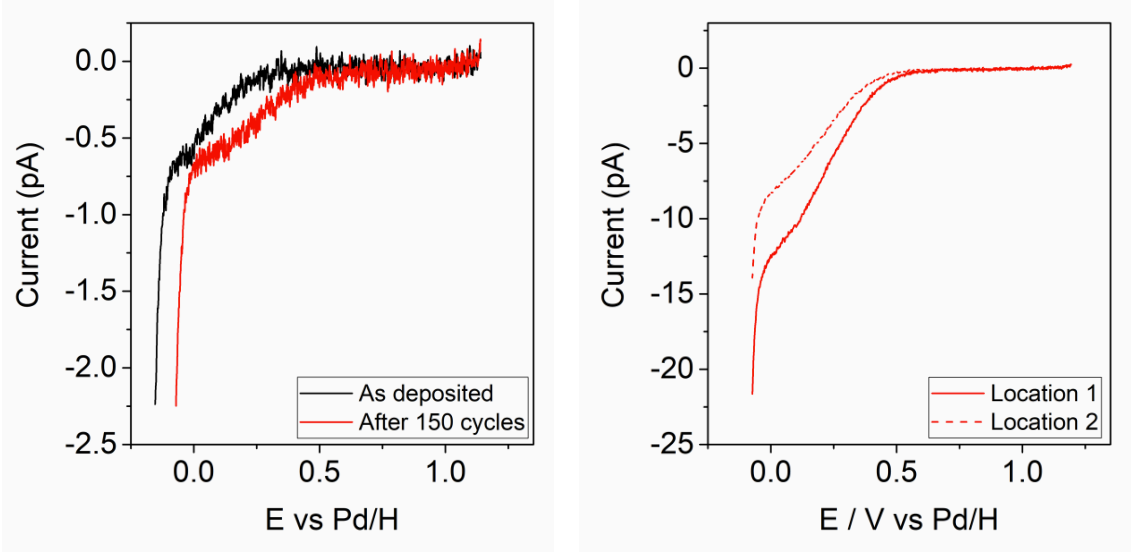

(A) LSVs obtained on the LD-HIE sample before (black) and after (red curve) electrochemical cleaning.

(B) LSVs obtained on the HD-HIE samples after electrochemical cleaning in two different locations.

FIGURE 3.3: LSVs obtained on the **(A)** LD-HIE and **(B)** HD-HIE samples before (black curves) and after (red curves) electrochemical cleaning. Scan rate ν =0.1 V s^{-1}, solution: 0.1 M $HClO_4$. Images obtained from [123].

As for the Pt clusters on the samples, STEM imaging after electrochemical cycling revealed harsh alterations to particle spatial distribution, as well as causing some platinum loss and NCs to aggregate. This is reflected in the different LSVs that were obtained on the HD sample in different areas (*vide* figure 3.4), where significant differences between the ORR limiting currents were observed when the tip was landed in different locations on the TEM grid's surface, probably due to the uneven distribution of the agglomerated clusters after cleaning.

Whereas the catalyst activity of the samples towards the ORR only improved slightly, the changes to the NCs, reflected in their morphology, size and spatial distribution, is drastic, as illustrated in the STEM images in figure 3.4 and particle size histograms in figure 3.5, especially for the HD sample. Table 3.2 lists relevant parameters obtained from the analysis of HAADF-STEM images, including the percentage of "singlets", their projected area, the substrate's covered area, cluster density and average particle area. For this analysis, 1 M

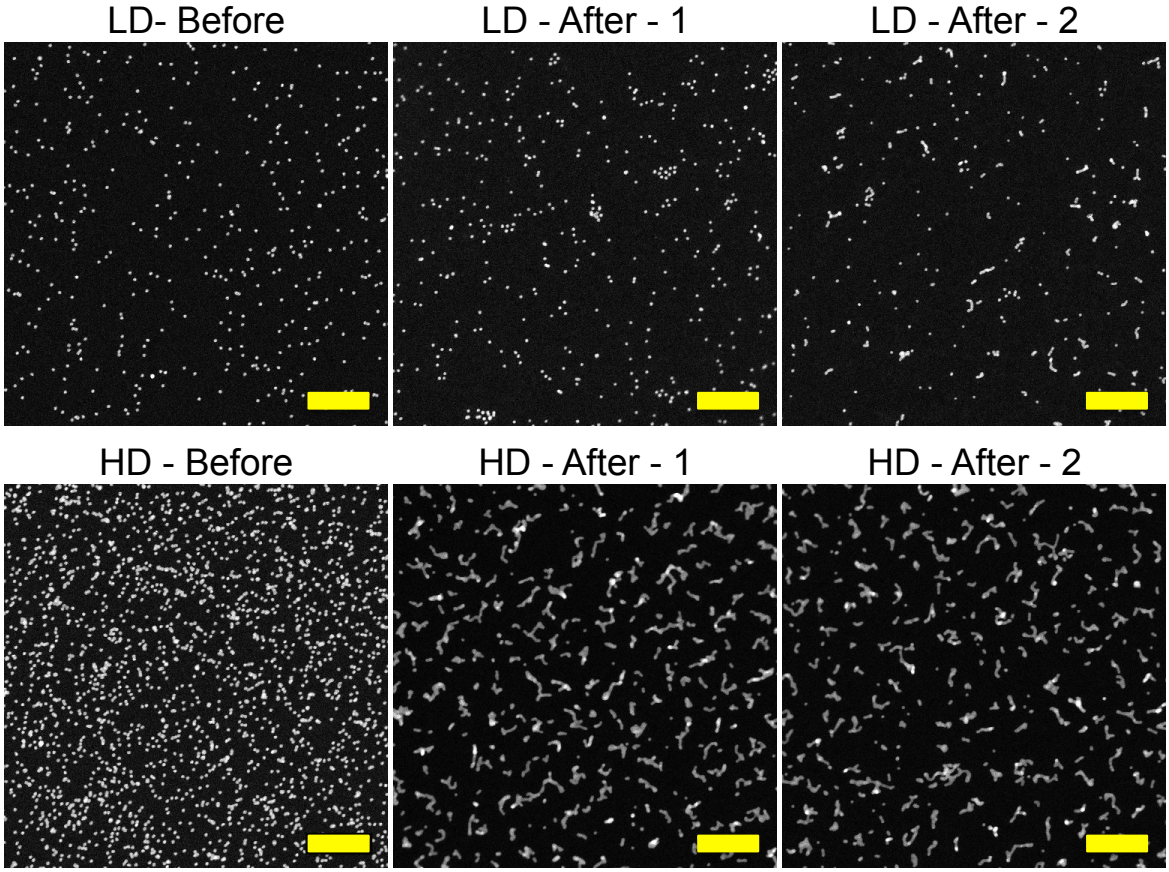

FIGURE 3.4: HAADF-STEM images of LD-HIE and HD-HIE samples before and after electrochemical cleaning. Two different locations are depicted of the sample after EC cleaning (indicated as "after 1" and "after 2"). The scale bars indicate 50 nm.

images were used (at least 5 images per sample and state (i.e. before and after)). The relative quantity of singlets is a measure for cluster aggregation, and a decrease in their size reveals platinum dissolution. The percentage of the substrate area that's covered by Pt, cluster density and the average NP area (including particles of all sizes) all depend on particle aggregation, detachment and platinum loss.

Note that, although it was not possible to take images in the exact same locations before and after the EC cleaning, all images presented here were recorded in the same square in each of the TEM grid samples. Significant changes were observed for all these parameters and both samples.

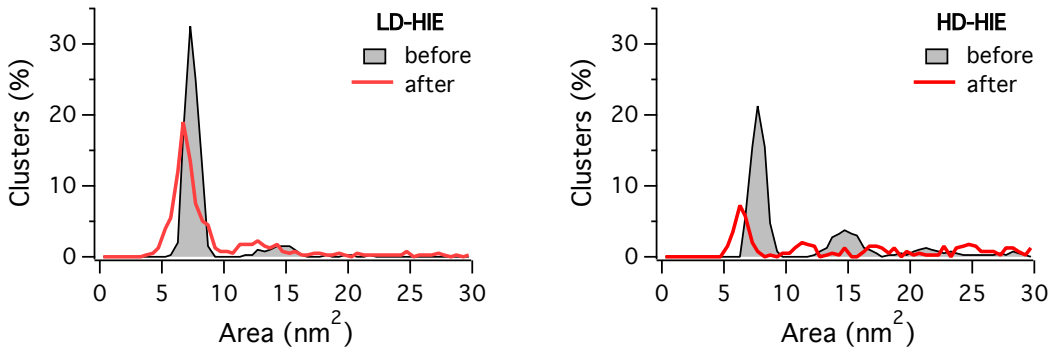

(A) LD-HIE. (B) HD-HIE.

FIGURE 3.5: Cluster area histograms of the LD and HD samples before and after electrochemical cleaning.

TABLE 3.2: Size and Pt loading descriptors obtained before and after electrochemical cleaning of LD-HIE and HD-HIE samples: percentage of singlet NCs, singlet projected area (average and standard deviation), surface coverage (A_{covered}), cluster density and particle projected area (average and standard deviation, including particles of all sizes).

Sample	Singlet %	Singlet area nm^2	A_{covered} %	cl. density cm^{-2}	Particle area nm^2
LD before	90.1	7.44 ± 0.50	3.3	4.1×10^{11}	8.15 ± 2.30
LD after	76.1	7.00 ± 1.10	2.9	3.0×10^{11}	9.70 ± 6.45
HD before	63.3	7.74 ± 0.57	17.6	1.4×10^{12}	12.45 ± 8.50
HD after	20.9	6.39 ± 0.57	12.6	3.2×10^{11}	39.17 ± 35.49

Analysis of the images obtained of the Pt_{923} samples before and after EC cycling confirms more dramatic changes in the HD specimen, but the same trends were observed for both samples. Although the cluster size histograms obtained after EC cleaning still shows distinct peaks for singlet and doublet particles, there is a shift to smaller sizes, and in the HD sample, the peaks for the larger particles broaden and merge after the treatment. This is accompanied by a decrease in the proportion of singlets and increase in the percentage of larger particles. Whereas before electrochemical cycling only 0.35% and 14.5% of all particles were larger than $20\,nm^2$, after, these percentages grow to 6.5% and 61.3% for the LD and HD samples, respectively. Additionally, particle density and surface coverage decrease (see table 3.2), and average particle size increases.

For both samples, there is strong evidence for particle movement (evident in the STEM images, *vide* figure 3.4), sintering (i.e. increase in particle average size, decrease in proportion of singlets, decrease of particle density and surface coverage), and of loss of platinum (indicated by the decrease in singlet and doublet size, decrease in covered surface area).

The results presented here clearly demonstrate that electrochemical cleaning of the samples leads to a loss of the properties, such as narrow size distribution of the Pt catalysts and their random spatial distribution, which were vital in this study (*vide infra*). For that reason, further experiments were executed with samples "as deposited", without further processing steps.

3.3 Oxygen Reduction Reaction

The electrocatalytic activity of the as-deposited (not pre-cleaned, as discussed in section 3.2.1) Pt_{923} clusters towards the ORR was investigated by linear sweep voltammetry. Figure 3.6 presents LSVs obtained at $\nu = 10\,mV\,s^{-1}$ (1^{st} cycle) on the three samples and compares their performance. The LSVs are plotted with the current density normalised by

the tip area (≈1 μm^2, figure 3.6(A)) and by the Pt surface area (figure 3.6(B)). The droplet contact area and total platinum surface area employed to normalise the currents in figure 3.6 were estimated using the results from the particle size analysis by considering hemispherical particles.

The LSVs in figure 3.6 reveal onset potentials for the ORR of *ca.* 0.7 V *vs.* Pd/H for the HD sample, and *ca.* 0.6 V for the low density samples, and a wide kinetic or mixed-control region down to *ca.* 0.2 V *vs.* Pd/H. For the HD sample, the current plateaus between ≈0.2 V and 0.05 V. At 0.05 V *vs.* Pd/H, the current increases strongly due to the hydrogen evolution reaction (HER) for all samples. Similar curves have been reported for the ORR on platinum in setups with very high mass transport rates.[137, 142, 145]

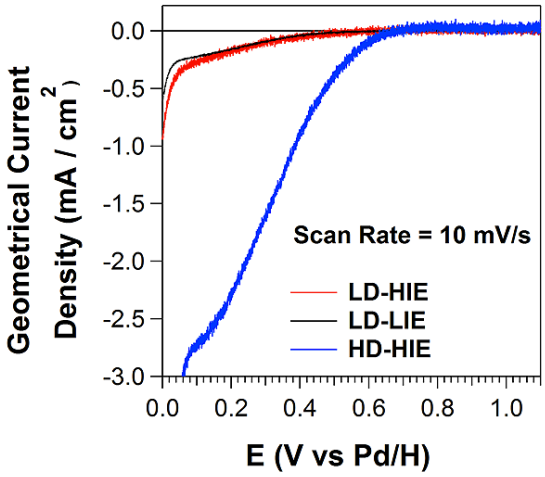

(A) LSVs with current densities normalised by the droplet-substrate contact area.

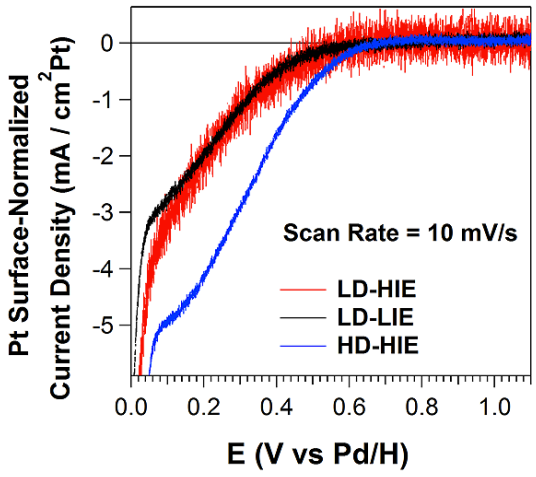

(B) LSVs with current densities normalised by the platinum surface area.

FIGURE 3.6: LSVs (1st scan) obtained on the three samples studied in this work with a SECCM setup. Details in the main text. Image obtained from [123].

Finite element method (FEM) simulations have been carried out for a SECCM configuration that is comparable to the one used in this work and is available in the literature.[120, 137] The concept of the model is described in detail in [137] (Supplementary Information, section 2). Briefly, the simulation was carried out for an air-saturated 50 mM H_2SO_4 solution

and a tip with $d \approx 0.5\,\mu m$ and the boundary conditions took into account the permeability of the meniscus walls to air (the concentration of oxygen at the meniscus walls was set to that of air-saturation ($c_{O2} = 2.5 \times 10^{-7}\,mol\,dm^{-3}$). The theoretically expected diffusion-limited current for the $4e^-$ ORR (equation 1.2 in section 1.2.4), calculated from the FEM simulations,[120, 137] was found to be $\approx 6\,mA\,cm^{-2}$.

For the samples studied in this work, the apparent limiting current densities are *ca.* $2.7\,mA\,cm^{-2}$ and $0.3\,mA\,cm^{-2}$ for the HD and LD samples, respectively.

For the HD sample, this implies that, if the current measured just before the onset of HER is limited by the diffusion of O_2 to the electrode's surface, the ORR occurs via a $2e^-$ mechanism (equation 1.3). Although HER only starts at $E \approx 0.1\,V$, hydrogen adsorption starts at $E \leq 0.3\,V$ for platinum,[146–151] preventing the 4-electron ORR from occurring. In this case, the $2e^-$ pathway is expected, in agreement with the experimental results for this sample.

For the LD samples, the current density is much lower than the expected value, indicating that the process is not limited by mass transport, even in the case of a $1e^-$ mechanism. The most probable reason for the low limiting currents in the LD samples is the blocking of catalytically active sites on the Pt surface due to adsorbed species.[147–152] The current densities for the LDs samples are lower than that of the HD sample even when normalised by the platinum surface area (figure 3.6(**B**)). The low currents for the samples with low platinum loadings indicate that O_2 is not fully reduced at the clusters; instead, the reduction reaction is incomplete, and intermediate species are free to move and attack the carbon support (*vide infra*). This is further promoted by the mass transport asymmetry in the SECCM setup, where the oxygen flux is enhanced (due to the air/solution interface at the droplet) and any products of the ORR are confined to the solution.

Figure 3.6(B) also shows that LD-HIE and LD-HIE are very similar, confirming that the different impact energies employed to deposit the clusters and the small changes in their shape (section 3.2) do not affect the NCs' catalytic activity.

3.3.1 Stability of the electrocatalytic activity

Figure 3.7 shows the cathodic scans of CVs with multiple cycles. Figures 3.7(A) and 3.7(B) were performed on the LD-LIE and LD-HIE samples, respectively, at $\nu = 10\,\mathrm{mV\,s^{-1}}$ and figures 3.7(C) and 3.7(D) on the LD-HIE and HD-HIE samples at $\nu = 100\,\mathrm{mV\,s^{-1}}$.

Figures 3.7(A) and 3.7(B) compare the performance and stability of the LD samples. The current density (normalised by the tip area) is slightly higher for the LD-HIE sample than for the LIE sample just before the onset of the HER (at 0.05 V *vs.* Pd/H). In the 1st cycle, the current densities were *ca.* $-0.33\,\mathrm{mA\,cm^{-2}}$ and $-0.27\,\mathrm{mA\,cm^{-2}}$ for LD-LIE and LD-HIE, respectively. This reflects the slightly higher Pt loading in the LD-HIE sample (≈6400 NCs μm^{-2}) relative to that in the LD-LIE (≈5650 particles μm^{-2}) specimen (see table 3.1). In both cases, the performance of the Pt_{923} catalysts degrades at a similar rate, and the current density falls to $\approx -0.1\,\mathrm{mA\,cm^{-2}}$ by the 10th cycle, indicating that the deposition impact energy has no effect in the catalyst stability over time.

Comparing figures 3.7(B) and 3.7(C), both performed on the LD-HIE sample but with different scan rates, there are two main differences: (i) the apparent limiting current density (at $E = 0.05$ V *vs.* Pd/H, just before the onset of HER) at $\nu = 100\,\mathrm{mV\,s^{-1}}$ is *ca.* 1.5× that recorded at $\nu = 100\,\mathrm{mV\,s^{-1}}$, and (ii) the current magnitude decreases faster with each cycle at a slower scan rate, suggesting that the degradation of the Pt catalysts is time-dependent.

This decrease in the electrocatalytic current magnitude is much slower in the HD sample (figure 3.7(D)). Whereas the current magnitude is reduced by $\approx 1/3$ at the LD-HIE sample,

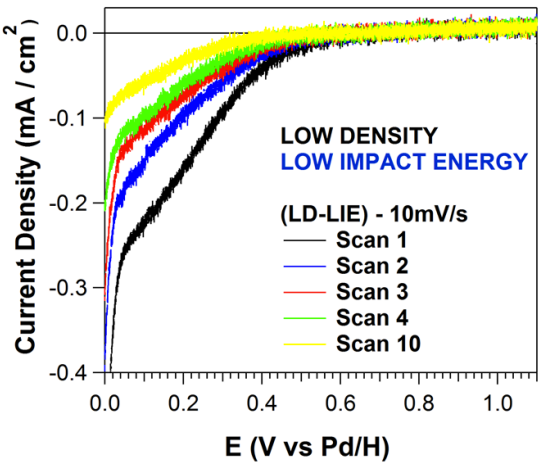

(A) LD-LIE; $\nu = 10\,\mathrm{mV\,s^{-1}}$.

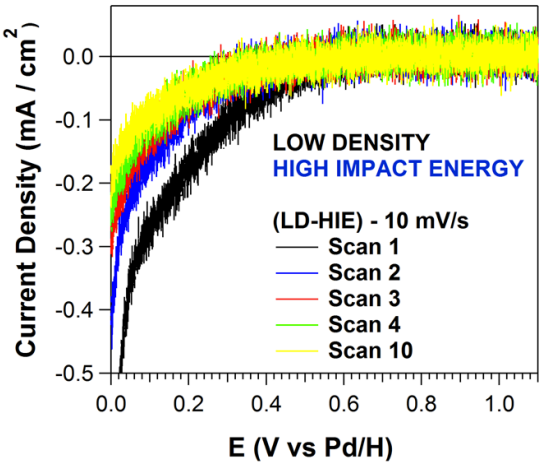

(B) LD-HIE; $\nu = 10\,\mathrm{mV\,s^{-1}}$.

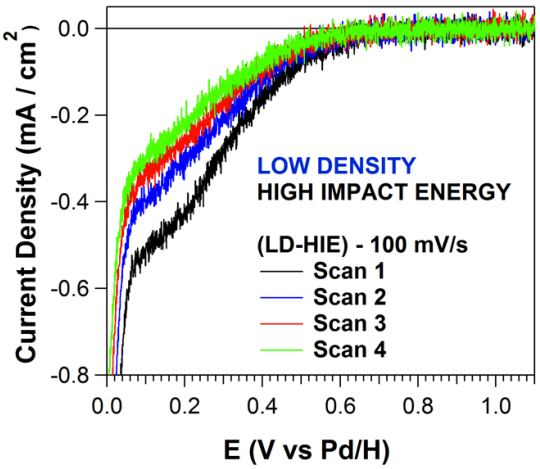

(C) LD-LIE; $\nu = 100\,\mathrm{mV\,s^{-1}}$.

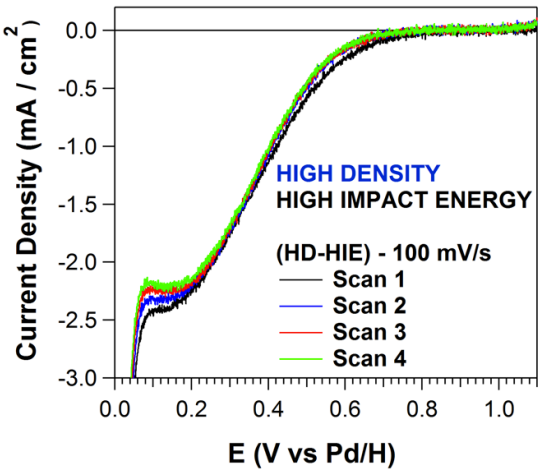

(D) HD-HIE; $\nu = 100\,\mathrm{mV\,s^{-1}}$.

FIGURE 3.7: Repeat LSVs recorded in the SECCM configuration ($d_{\mathrm{tip}} \simeq 1\,\mu\mathrm{m}$) in air-saturated 0.1 M $HClO_4$. Currents were normalised by the geometrical area. Image obtained from [123].

it only decreases by ≈10% for the HD-HIE specimen. This suggests that the degradation mechanism is retarded at a higher Pt loading.

The possible causes for the catalyst degradation which were considered in this work are Pt dissolution, cluster migration-aggregation, Ostwald ripening, Pt surface poisoning, and carbon corrosion (*vide* schematic illustration in figure 3.8). Platinum dissolution leads to a decrease in catalyst loading and in electrochemically actice surface area (ECSA), reducing the catalytic current. Cluster migration-aggregation and Ostwald ripening also results in a decrease in ECSA due to aggregation of smaller particles into larger ones. Finally, carbon corrosion can induce Pt migration and/or detachment due to a weakening of the Pt-C interaction.[134, 139, 153–156]

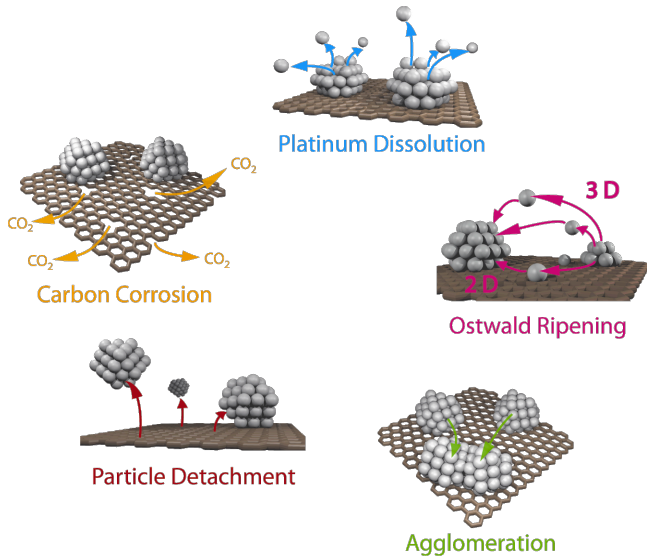

FIGURE 3.8: Schematic illustration of the possible degradation mechanisms for a carbon/Pt catalytic system. Image obtained from [139].

Small carbon-containing species (expecially CO) can block active sites on platinum catalysts, causing a deterioration of their performance.[156, 157] Such contaminants may originate from the carbon support itself, catalysed by the Pt clusters. It has been shown that Pt catalyses the oxidation of carbon to CO_2 electrochemically at $E > 0.207\,\mathrm{V}$ *vs.* RHE. [158] Although the kinetics of these reactions are very slow at $E \leq 1\,\mathrm{V}$ *vs.* RHE,[159] it is

catalysed by small platinum clusters.[160] Alternatively, the carbon can also be attacked by reactive intermediaries (RIs) and oxidised chemically. [161–164]

Possible RIs include hydrogen peroxide, H_2O_2, [161, 163] , superoxide anion radical, $O_2^{\bullet -}$, [165–168] hydroxil radical, $^{\bullet}OH$,[169–171] and hydroperoxyl radical, $^{\bullet}OOH$,[172] and all of these have been identified as products of the ORR in PEMFCs.[169, 173, 174] and in acidic solutions [166, 172, 175] and suggested as possible intermediates.[149, 150, 176] Due to the high mass-transport rates in the SECCM configuration, these species can wander off as soon as they're formed, and attack the carbon substrate.[160] The products of those reactions can, in turn, be adsorbed on the surface of Pt NCs, effectively poisoning them.[163]

In the following sections, these possible causes for the catalyst degradation after driving the ORR are explored. The effect of H_2O_2, an oxidative product of the ORR, was investigated employing cyclic voltammetry (section 3.4), Pt migration and aggregation was assessed through HAADF-STEM imaging (section 3.5), and the stability of the carbon support was studied with the help of X-ray photoelectron spectroscopy (XPS) (section 3.6).

3.4 Hydrogen Peroxide Damage

Possible damage done on the amorphous carbon / Pt_{923} catalyst system by hydrogen peroxide (which is generated during the ORR) was assessed by landing a SECCM tip ($d \approx$ 1 µm), filled with 0.1 M $HClO_4$ solutions containing 1 and 5 mM H_2O_2, and holding the droplet in contact with the substrate during 3 min. CVs were obtained as soon as the tip landed, and after this period, and are presented in figure 3.9.

Figures 3.9(A) and 3.9(C) show CVs recorded immediately after contact was established between the SECCM droplet and the TEM grid sample (black curve) and after a 3-minute wait period (red curve), where no electrochemical reaction was driven. Similar currents were

recorded before and after the wait period for both H_2O_2 concentrations used. Additionally, a series of consecutive CVs were performed on the same sample. The 1st (black curve) and 5th (green curve) scans are represented in figures 3.9(B) and 3.9(D), revealing decreases in current as observed previously in $HClO_4$ solutions with no added H_2O_2 (section 3.3.1). It is worth highlighting that, for a potential window of 1.1 V and a scan rate of 0.1 V s^{-1}, the 5th scan is performed <2 min after the 1st. These results are clear evidence that the degradation of the NC catalysts are not a result of hydrogen peroxide and must be generated by other reactive species formed during ORR.

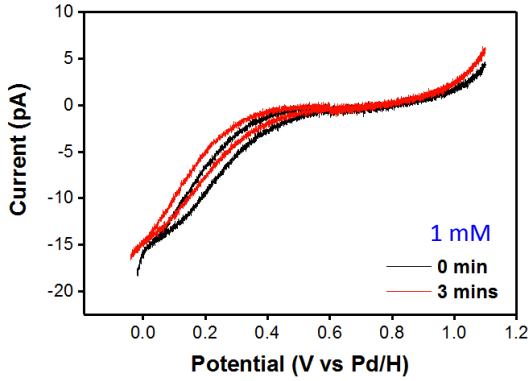

(A) 1 mM H_2O_2; CVs before and after a 3 min contact with the substrate.

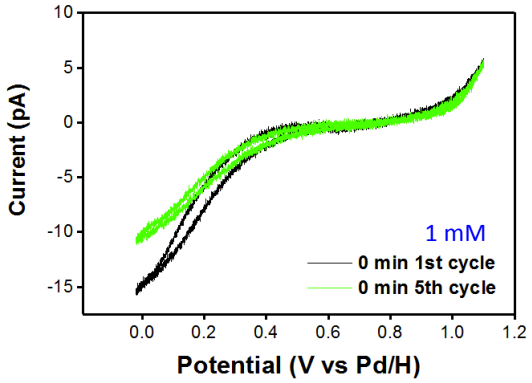

(B) 1 mM H_2O_2; 5 CV cycles performed immediately upon landing.

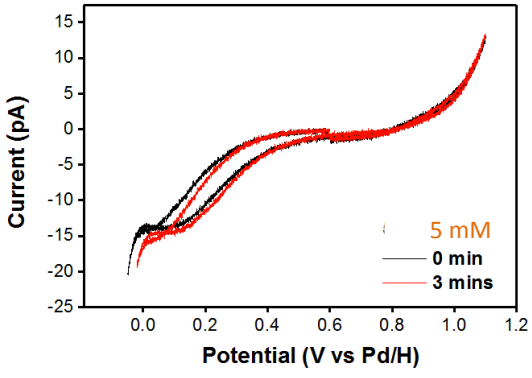

(C) 5 mM H_2O_2; CVs before and after a 3 min contact with the substrate.

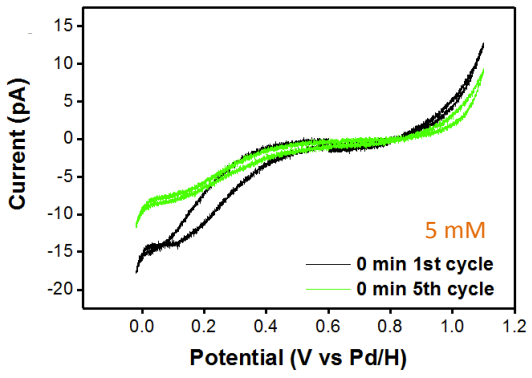

(D) 5 mM H_2O_2; 5 CV cycles performed immediately upon landing.

FIGURE 3.9: CVs recorded at 100 mV s^{-1} in a SECCM configuration on a LD-HIE sample with H_2O_2-containing 0.1 M $HClO_4$ solutions immediately upon landing of the SECCM tip and after a 3 min holding period. Image obtained from [123].

3.5 Cluster Mobility and Aggregation

3.5.1 STEM analysis

HAADF-STEM was employed to explore the changes to NC size distribution, spatial distribution, particle density and surface coverage as a consequence of electrochemical experiments. This information is utilised to assess the occurrence of dissolution, detachment, Ostwald ripening and migration-aggregation during the ORR, and to help determine the cause for the gradual loss of electrocatalytic activity reported in section 3.3.1.

The SECCM landing locations were estimated as described in section 2.2.1.1 and areas where the ORR was executed were identified due to the resulting increase in the background intensity. Examples of such bright areas can be seen in figure 3.10. Clusters were imaged in these locations ("inside", or after ORR) and also in nearby areas ("outside"). The "outside" clusters were used as a control, as their state is equivalent to before performing any electrochemical tests. Unfortunately, due to the brightening of the carbon background, a quantitative analysis of the integrated HAADF-intensity of individual clusters to determine their size (number of constituent atoms) was not possible. For that reason, the size analysis was performed employing the NCs' projected area and corresponding diameter (assuming spherical clusters).

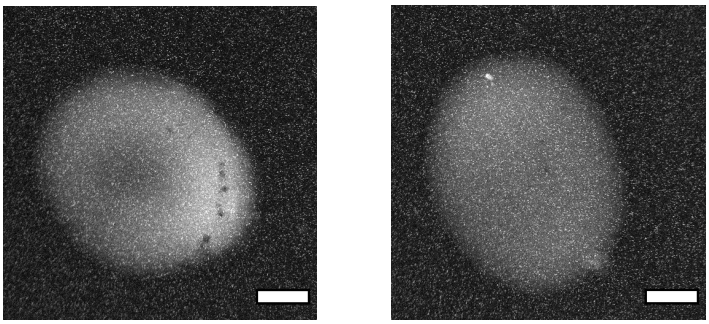

(A) 50 scans, 100 mV s^{-1}. (B) 50 scans, 1000 mV s^{-1}.

FIGURE 3.10: STEM images of the LD-HIE sample showing the brightened background after ORR. The scalebar indicates 250 nm.

Figures 3.11 **(A)-(C)** show representative STEM images of the LD samples after ORR. Figure 3.11(A) was recorded after 15 cycles at a scan rate $\nu = 10\,\text{mV}\,\text{s}^{-1}$ on the LD-HIE sample, highlighting the lack of obvious changes to the clusters (in size or spatial distribution) compared to pristine areas (see figure 3.1(C)), even after subjecting the sample to the lengthiest ORR testing (total time = 3300 s, or 55 min). Figures 3.11(B) and 3.11(C) were obtained from the LD-LIE sample after 20 scans at $\nu = 50\,\text{mV}\,\text{s}^{-1}$ and 50 scans at $\nu = 100\,\text{mV}\,\text{s}^{-1}$, respectively. Both images show a change in the NC spatial distribution: instead of randomly distributed clusters (compare to figure 3.1(A)), a significant portion of the Pt clusters deposited with a low impact energy form groups of closely arranged clusters, revealing clear evidence of particle movement. Interestingly, although the NCs get very close and can form groups of 15 clusters or more, the NCs do not touch or merge to a significant extent (*vide infra*). This "clustering" of the NCs is typical for this sample.

The change in spatial distribution is reflected in a shortening of the nearest neighbour distances (NNDs). Centre-to-centre NND histograms were created for clusters after the ORR experiments and in nearby, pristine areas for both low density samples using 2 M magnification images. Histograms corresponding to each of the images in figure 3.11 (A)-(C) are shown below the respective STEM image: figures 3.11 (D)-(F) show the "inside" NNDs and figures 3.11 (G)-(I) the "outside" results; cumulative NND histograms for both LD

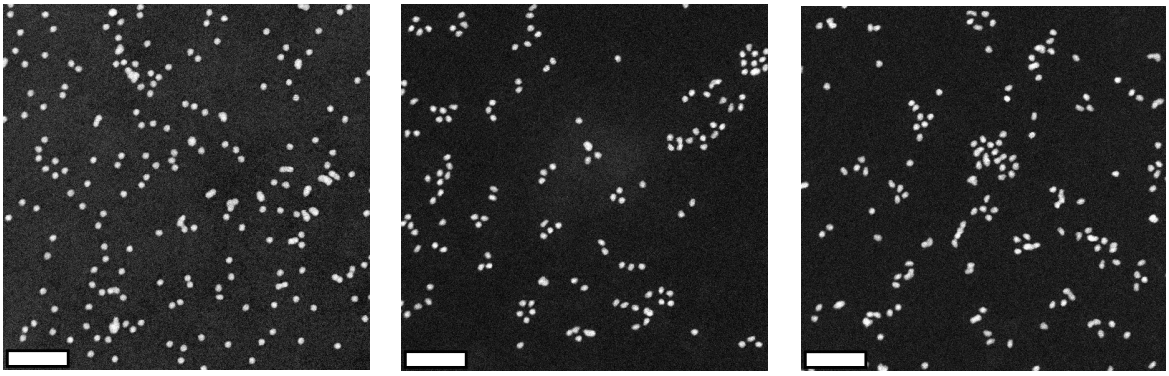

(A) LD-HIE; 15 cycles, $\nu = 10\,\mathrm{mV\,s^{-1}}$, $t_{\mathrm{tot}} = 3300\,\mathrm{s}$.

(B) LD-LIE; 20 cycles, $\nu = 50\,\mathrm{mV\,s^{-1}}$, $t_{\mathrm{tot}} = 880\,\mathrm{s}$.

(C) LD-LIE; 50 cycles, $\nu = 100\,\mathrm{mV\,s^{-1}}$, $t_{\mathrm{tot}} = 1100\,\mathrm{s}$.

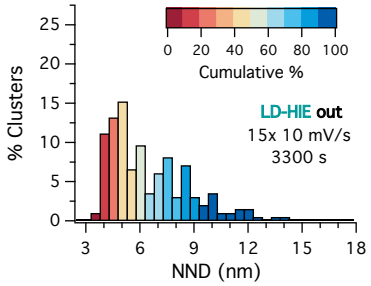

(D) Outside.

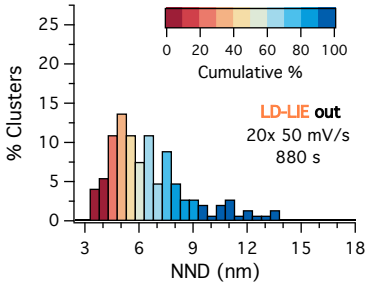

(E) Outside.

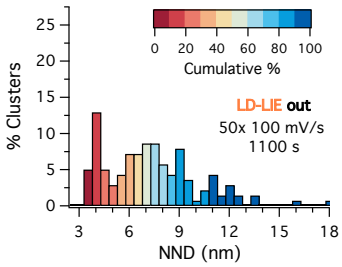

(F) Outside.

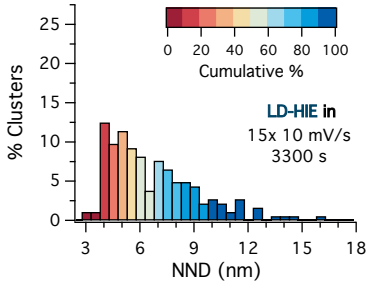

(G) Inside.

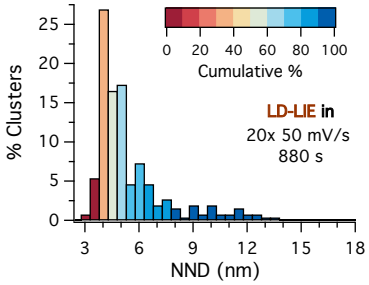

(H) Inside.

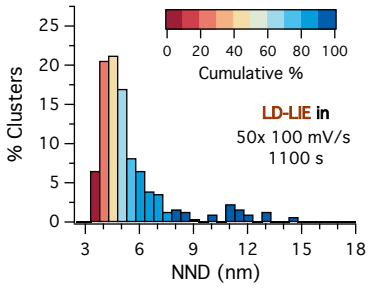

(I) Inside.

FIGURE 3.11: **(A)-(C)** HAADF-STEM images of areas of the LD samples where CVs were performed. The scalebars indicate 25 nm; t_{tot} is the total CV duration. **(D)-(I)** Centre-to-centre nearest neighbour distance histograms of areas **(D)-(F)** outside and **(G)-(I)** inside the droplet footprint.

samples and all ORR tests discussed in this work can be found in the appendix, in section A.1, figures A.1 (LD-HIE) and A.2 (LD-LIE sample).

Analysis of the NND histograms revealed a shift to shorter distances for the LD-LIE sample (compare figures 3.11(E) *vs.* 3.11(H) and 3.11(F) *vs.* 3.11(I)), which was observed for all "inside" areas (*vide* figure A.2). The same was not observed for LD-HIE (figures 3.11(D) *vs.* 3.11(D) and figure A.1), nor for the HD-HIE sample, which did not reveal significant changes in particle spatial distribution.

In pristine areas of the LD samples, there is a continuous distribution of the centre-to-centre NND between ≈3.5 nm and ≈13 nm, with a maximum at the shorter lengths and a gradual decrease as the distance increases. This arrangement remains unchanged for the LD-HIE sample even after executing consecutive CVs for almost 1 hour (3300 s; figure 3.11(G)). In contrast, the nearest neighbour distances for the LD-HIE sample, a shift to shorter cluster separation can be seen for all experiments: the NND histograms reveal increased frequency at ≈4-6 nm and only very small percentages beyond *ca.* 7 nm.

An additional set of experiments were performed, where a SECCM probe was landed on the LD-LIE sample and held there for times comparable to those used to investigate the ORR. No potential was applied during this waiting time, and the probe was lifted, removing the droplet from the substrate. No changes in the spatial arrangement or size of clusters were detected in those cases. This indicates that the cluster movement and "clustering" is promoted by the potential cycling and/or the ORR.

Something similar to this characteristic arrangement of the NCs into groups has been observed for Pt NCs soft-landed on HOPG, with very low impact energies (0.1 eV per atom).[177–179] These patterns formed by Pt clusters have been attributed to small amounts of lightweight species, probably CO,[179] which readily adsorb on the platinum surface even under ultra-high vacuum (UHV) conditions. In the LD-LIE sample, the nearest neigh-

bour edge-to-edge distance is *ca.* 1.5 nm, which is close to the ≈1.2 nm identified in the UHV/HOPG studies. This supports the proposition that the loss in the Pt catalysts is caused to poisoning by small organic species, resulting from degradation/corrosion of the amorphous carbon support due to attack by reactive intermediates generated during the ORR. Such small chemical species would act to both block catalytic surface sites on the carbon, and protect the clusters from aggregation. HAADF-STEM cannot detect or identify such small, lightweight species. However, the brightening of the carbon support in areas where the droplet probe was landed and where ORR was driven is reminiscent of the contamination build-up which can occur during STEM imaging. This contamination is generated by the polymerisation of carbonaceous species, induced by the electron beam. [180, 181] Changes in the chemical environment of carbon (from the support) were confirmed by XPS (this will be explored in section 3.6). It is not unreasonable to speculate that, in the case of the samples studied in this work, the brightening of the background may be caused by a similar process, but induced electrochemically rather than by the electron beam.

Particle size was also compared in areas where the ORR was driven and in the vicinity of each droplet footprint. Although there is a slight shift to smaller NC sizes in some "inside areas", as illustrated in figure 3.12(B), this was not always the case (e.g. figure 3.12(A)), and no correlation could be found between experimental parameters during the CVs and the resulting histograms. Instead, the differences are more likely to be due to the manual thresholding step, which determines the carbon-platinum boundaries. A threshold was set manually for each image, which necessarily introduces some error. In this case, this problem is exacerbated by the changes in the background brightness, which varied even within the same footpring and must influence the thresholding process. In fact, there is a greater size (diameter) dispersion between different "outside" areas (or between different "inside" areas, as well) than between "inside" and "outside", as is exemplified in table 3.3. The same pattern was found for the other samples. Furthermore, where there is a change (mainly in

the LD-LIE sample), the difference between outside and inside is always smaller than the standard deviation, which is especially large in the "inside" areas of the LD-LIE sample. However, even if there is a small degree of platinum loss (Pt dissolution from the clusters), the extent to which this occurs is minimal and cannot explain the loss of electrocatalytic activity observed during the voltammetric experiments.

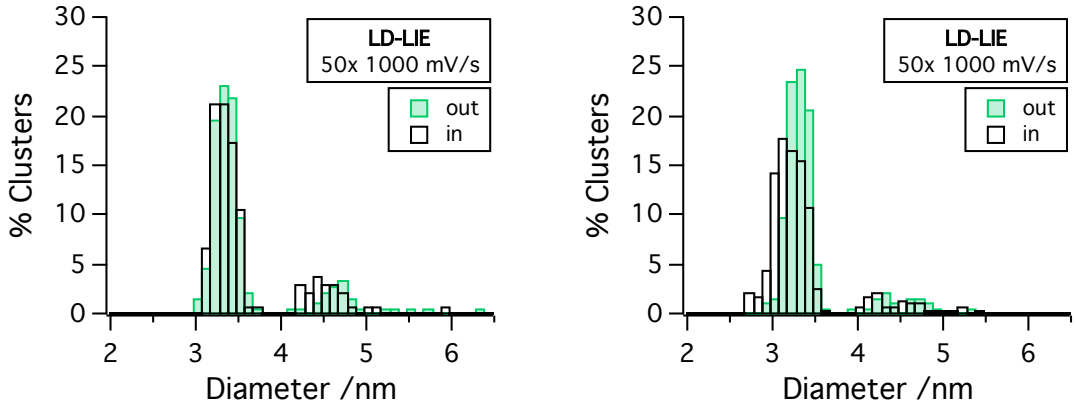

(A) (B)

FIGURE 3.12: Particle diameter histograms obtained before and after the same procedure (50 CV cycles, $\nu = 1\,\mathrm{V\,s^{-1}}$) on two distinct locations of the LD-LIE sample.

Further evidence against platinum dissolution is found when comparing the diameters in tables 3.3 and 3.4 with those in table 2.2. The average diameters for the LD-HIE sample are $d_{(\text{LD-HIE, out})} = 3.23 \pm 0.05$ nm and $d_{(\text{LD-HIE, in})} = 3.12 \pm 0.09$ nm, and for the LD-LIE sample, $d_{(\text{LD-LIE, out})} = 3.11 \pm 0.10$ nm (outside) and $d_{(\text{LD-LIE, in})} = 3.14 \pm 0.07$ nm. The values for $d_{(\text{LD-HIE, in})}$, $d_{(\text{LD-LIE, out})}$ and $d_{(\text{LD-LIE, in})}$ are very close to each other, and consistent with thresholding at 20% of the background-corrected maximum cluster intensity (for a cluster imaged at a very high magnification and clean background). The average for $d_{(\text{LD-HIE, out})}$ is slightly higher, similar to the $d_{15\%}$ in table 2.2, and it is very probable that the discrepancy is due to manual threshold setting step.

TABLE 3.3: Singlet diameter (average and standard deviation) and particle density before and after driving the ORR on the LD-LIE sample employing different number of scans and scanning rates. All the CVs were performed from $E = 1.1$ V to $E = 0$ V *vs.* Pd/H.

EC Experiment	Total Duration	d_{out} (nm)	d_{in} (nm)	N_{out} (10^{11} cm^{-2})	N_{in} (10^{11} cm^{-2})
15 x 10 mV s^{-1}	3300 s	3.22 ± 0.09	3.23 ± 0.16	6.8	6.3
50 x 50 mV s^{-1}	2200 s	3.07 ± 0.15	3.09 ± 0.11	6.4	6.3
50 x 100 mV s^{-1}	1100 s	3.02 ± 0.11	3.10 ± 0.10	6.4	6.4
50 x 500 mV s^{-1}	220 s	3.20 ± 0.10	3.19 ± 0.10	6.6	6.4
50 x 1000 mV s^{-1}	110 s	3.02 ± 0.11	3.07 ± 0.14	6.6	6.4

TABLE 3.4: Singlet diameter (average and standard deviation) and particle density before and after driving the ORR on the LD-HIE sample employing different number of scans and scanning rates. All the CVs were performed from $E = 1.1$ V to $E = 0$ V *vs.* Pd/H.

EC Experiment	Total Duration	d_{out} (nm)	d_{in} (nm)	N_{out} (10^{11} cm^{-2})	N_{in} (10^{11} cm^{-2})
10 x 10 mV s^{-1}	2200 s	3.29 ± 0.12	3.14 ± 0.30	5.6	5.1
50 x 100 mV s^{-1}	1100 s	3.16 ± 0.15	3.09 ± 0.15	5.5	5.6
20 x 50 mV s^{-1}	880 s	3.22 ± 0.14	2.98 ± 0.26	6.0	5.7
50 x 500 mV s^{-1}	220 s	3.22 ± 0.12	3.11 ± 0.14	6.1	6.0
50 x 1000 mV s^{-1}	110 s	3.27 ± 0.12	3.26 ± 0.12	6.1	6.0
50 x 1000 mV s^{-1}	110 s	3.22 ± 0.16	3.11 ± 0.19	6.1	6.1

Finally, figure 3.13 summarises the results from a coalescence analysis, showing that there is no significant change in the relative amounts of "singlet" or merged particles. Looking at each ORR spot individually (not depicted), no correlation was found between the number of cycles, scan rate, or CV total duration and changes to the NC population. These results confirm that no significant coalescence of clusters occurs in any of the studied samples, as was intuited from visual inspection of the STEM images.

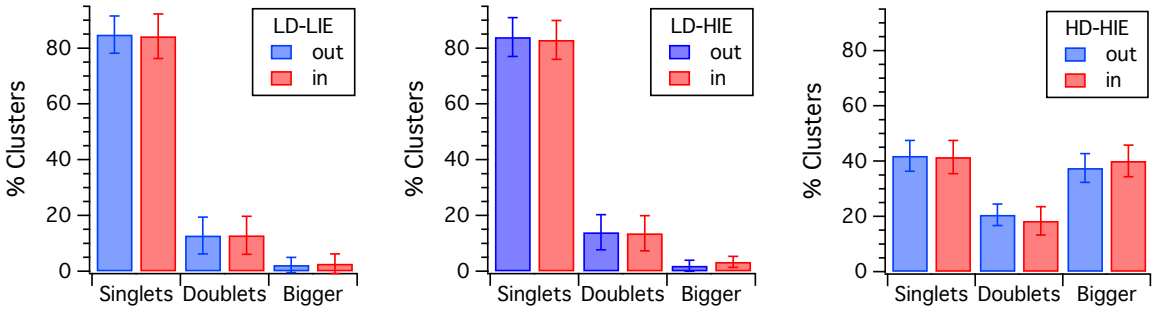

(A) LD-LIE (B) LD-HIE (C) HD-HIE

FIGURE 3.13: Relative quantities of singlets, doublets and larger particles for areas where ORR was driven ("inside") and pristine nearby areas ("outside") of the samples investigated in this work.

The results from the STEM analysis reveal that there is no significant platinum loss or coalescence of the NCs, allowing Ostwald ripening, migration-aggregation, and Pt dissolution or detachment to be excluded as causes for the loss of electrocatalytic activity of the Pt clusters in this study.

3.6 Changes in the Chemical Environments of Pt and C

X-ray photoelectron spectroscopy (XPS) was employed to identify changes in the chemical bonds of the species in the samples (carbon and platinum [182]), before and after a series of 200 voltammetric scans, performed at 0.2 V s^{-1}, from $E = 0$ V to $E = 1.1$ V *vs.* Pd/H. It should be noted that the CVs ended at $E = 1$ V, and it is expected that the Pt clusters will be partially oxidised. LD-HIE and HD-HIE samples were used for these tests, as well as a bare (as received) TEM grid. The XPS spectra can be found in the annex, in section A.2.

Table 3.5 shows the relative quantities (in atomic %) of carbon and platinum for the two samples, before and after electrochemical cycling. The remaining elements detected in the survey spectra (not included in this table) are oxygen (including atmospheric O, H_2O and

oxygen bound to Si, C or a metal), Au (from the metal frame of the TEM grid), Si, N, and very small percentages of Sn, F, and Cl.

An uncertainty of $\pm 2\%$ must be taken into account when considering the XPS results presented here, however, it is interesting to notice that the loss of platinum is much stronger ($\approx$80%) for the LD sample than for the HD sample ($\approx$34%). The changes in composition of these elements will be explored in more detail in the subsequent subsections.

TABLE 3.5: Relative amounts (in atomic %) of carbon, platinum and oxygen before and after ORR, obtained from XPS survey spectra.

	LD				HD			
Element	Before	After	Change		Before	After	Change	
C	80.18	63.51	-16.67	(-20.8%)	64.58	67.40	+2.82	(+4.4%)
Pt	0.82	0.16	-0.66	(-80.5%)	8.16	5.38	-2.78	(-34.1%)

3.6.1 Platinum

Table 3.6 presents the relative atomic amounts of metallic Pt and platinum oxide (PtO) in the LD-HIE and HD-HIE samples. The results show that the as-deposited platinum is fully reduced (100% metallic). After driving the ORR, the ratios of Pt oxide to metallic platinum are 14.6% and 6.1% for the LD and HD samples, respectively, indicating that the surface of the NCs are oxidised more extensively when their density is lower. This again shows that the damage done to the carbon/Pt_{923} system is more severe with a low Pt loading.

TABLE 3.6: Relative amount (RA, in atomic %) of of metallic and oxidised platinum based on fitting the Pt $4f_{7/2}$ spectra before and after ORR in the LD-HIE and HD-HIE samples.

	LD		HD	
Environment	Before	After	Before	After
metallic Pt	100	87.27	100	94.26
Platinum oxide	0	12.73	0	5.74
PtO/Pt ratio	0	14.6%	0	6.1%

STEM images were used to estimate the surface area to volume ratio of the platinum deposited at high and low densities (*vide* section 3.5). Singlets were assumed to be spheres (with $V = 4/3\pi r^3$ and $A_s = 4\pi r^2 = 4A_p$), whereas larger particles, due to their more irregular shapes, were approximated as having the shape of their 2D projection and a uniform height equivalent to the average diameter of a singlet, so that their volume and surface area were calculated according to the following relations:

$$V = A_p \cdot d_{sing} \tag{3.1}$$

$$A_s = 2A_p + P \cdot d_{sing} \tag{3.2}$$

where A_p is the projected (2D) area, A_s is the (3D) surface area, d_{sing} is the average diameter for a singlet cluster, and P is the particle's perimeter.

The results of this analysis for the LD-HIE and HD-HIE samples, which were also used for the XPS studies, are presented in table 3.7. It is interesting to note that, although the values of the surface area and volume for these samples was estimated using a simple model, the ratio of total volumes for the LD and HD sample obtained in this manner ($V_{LD}/V_{HD} = 11\%$) is in good agreement with the relative amounts of Pt obtained from the XPS analysis (8.16% for the high density and 0.82% for the low density samples, *vide* table 3.5). This agreement validates the methodology used to estimate the parameters presented in table 3.7.

As expected, the A_s/V ratio is higher for the low density sample because of the higher proportion of singlets. However, the ratios of the surface area to volume ratios of these samples (HD/LD) is low, *ca.* 1.2, only about half of the ratios of platinum oxide to metallic platinum obtained from the XPS analysis (*vide* table 3.6, $14.6/6.1 = 2.4$). Instead, the higher extent of the oxidation of the platinum surface in the LD samples corroborates a mechanism in which the low density of Pt catalysts allows RIs to travel from the site where they are formed before being fully reduced and to attack the carbon, forming carbon oxides which can then poison the platinum surface. When the platinum coverage is higher, there is a greater probability of the RIs from the ORR process to meet another platinum catalytic site, decreasing the concentration of such poisonous species.

TABLE 3.7: Surface area and volume densities for the HD-HIE and LD-HIE samples.

Sample	A_s $\mathrm{nm^2_{Pt}\,\mu m^{-2}}$	V $\mathrm{nm^3_{Pt}\,\mu m^{-2}}$	A_s/V $\mathrm{nm^{-1}}$	V/V_{HD}
HD-HIE	1.91×10^6	1.29×10^6	1.48	100 %
LD-HIE	2.56×10^5	1.40×10^5	1.82	11%

It is also interesting to note that the binding energies corresponding to oxidised platinum have different energies in the LD ($E_{bind} = 73.6\,\mathrm{eV}$) and HD ($E_{bind} = 74.2\,\mathrm{eV}$) samples after ORR. Due to the low Pt density in the LD sample and consequent noise in the Pt $4f_{7/2}$ spectrum (shown in section A.2.1, figure A.3), no definitive conclusions can be drawn from this. However, it implies that the oxidation of the platinum surface does not differ just in degree depending on the Pt loading, the Pt surfaces are very probably also chemically distinct.

3.6.2 Carbon

The results obtained from the carbon 1s XPS spectra are summarised in tables 3.8 (LD-HIE), 3.9 (HD-HIE) and 3.10 (bare grid), and the experimental spectra and their deconvolution into the contributions of the different carbon bonds can be found in the annex section A.2.2, figure A.4.

For the LD sample, the XPS results reveal significant changes to carbon's chemical environment (*vide* table 3.8), with a decrease in the graphitic carbon content from ≈53% to ≈22%, accompanied by a comparable increase in the C−C and C−H (≈34% to ≈53.5%). The amount of C−OH/C−N bonds increased by *ca.* 1.3, O−C=O by 1.5, and there was a small decrease in C=O.

The changes in the chemical environment of C werenot as drastic in the HD sample, as shown in table 3.9. The C−C/ C−H content remained almost unchanged, there was a ≈17% decrease in the proportion of graphitic carbon, and the remaining bonds species increased by ≈40-50% each. Interestingly, the changes observed for the HD-HIE sample (table 3.9) are comparable to those undergone by the bare TEM grid, with no platinum (table 3.10).

TABLE 3.8: Relative amount (RA, in atomic %) of the different chemical environments for C based on fitting the C 1s spectra and changes in RA (ΔRA) due to ORR in the LD-HIE sample.

LD-HIE sample				
Environment	Before	After	ΔRA (abs.)	ΔRA (rel.)
Graphitic C	52.94	22.42	−30.52	−57.7%
C−C or C−H	34.12	53.52	+19.40	+56.9%
C−OH or C−N	5.97	13.91	+7.94	+133%
C=O	4.22	3.30	−0.92	−21.8%
O−C=O	2.75	6.85	+4.10	+149%

TABLE 3.9: Relative amount (RA, in atomic %) of the different chemical environments for C based on fitting the C 1s spectra and changes in RA (ΔRA) due to ORR in the HD-HIE sample.

HD-HIE sample				
Environment	Before	After	ΔRA (abs.)	ΔRA (rel.)
Graphitic C	47.76	39.44	−8.32	−17.4%
C−C or C−H	33.08	32.95	−0.13	−0.4%
C−OH or C−N	11.84	16.85	+5.01	+42.3%
C=O	3.71	5.32	+1.61	+43.4%
O−C=O	3.62	5.44	+1.82	+50.3%

TABLE 3.10: Relative amount (RA, in atomic %) of the different chemical environments for C based on fitting the C 1s spectra and changes in RA (ΔRA) due to ORR in a bare (no Pt) TEM grid.

bare TEM grid (no Pt)				
Environment	Before	After	ΔRA (abs.)	ΔRA (rel.)
Graphitic C	53.13	41.13	−12.00	−22.6%
C−C or C−H	31.64	36.29	−0.13	−0.4%
C−OH or C−N	9.11	11.12	+2.01	+22.1%
C=O	4.22	7.59	+3.37	+79.9%
O−C=O	1.90	3.87	+1.97	+103.7%

The differences in the integrity of the carbon films in the samples with a low and higher platinum loads, after undergoing the same ageing procedure, indicate that a greater amount of platinum protects the carbon from degradation, in agreement with the electrochemical evidence discussed in section 3.3.1. This is further supported by the comparable changes recorded for the carbon on the TEM grid in the absence of platinum.

Overall, the XPS results support a mechanism in which damage is caused by reactive species generated during the Pt-catalysed ORR, possibly $^{\bullet}$OH and $^{\bullet}$OOH radicals.[153, 162] At low loading, these species can escape the platinum surface and reach the carbon to react

and generate small organic molecules, which can adsorb on the Pt surface, blocking it. On the other hand, with higher Pt densities, there is a higher probability of such RIs being electrochemically reduced on NCs to H_2O_2 or H_2O, mitigating the corrosive consequences of driving the ORR.

3.7 Summary and Conclusions

Model catalyst systems for the ORR were prepared by depositing mass-selected platinum nanoclusters (Pt_{923}, having 923 constituent atoms and $d \approx 3$ nm) with a very narrow size dispersion (*ca.* 4 %) onto gold TEM grids which were covered by thin amorphous carbon films. The cluster source employed to generate and deposit the Pt NCs allows for independent control of cluster size (number of constituent atoms), density and deposition energy, allowing the preparation of well-defined systems.

Two NC densities, "low" (LD, *ca.* 6% surface coverage) and "high" (HD, ≈37% surface coverage) were chosen and two impact energies were employed to soft-land the clusters onto the substrate (0.54 and 1.6 eV per atom; LIE and HIE, respectively), allowing the effects of Pt loading and adherence of the NCs to the carbon support to be investigated. Table 3.1 summarises the characteristics of each of the samples used in this chapter, and representative STEM images and particle size (projected area) histograms are presented in figure 3.1.

It is customary to clean platinum catalyst surfaces before electrochemical tests, usually employing cyclic voltammetry, but it was found that extensive potential cycling lead to drastic changes to the Pt NCs in the samples utilised herein, as evidenced by the STEM images presented in figure 3.4. Strong evidence was found for cluster migration-aggregation and platinum loss (*vide* figures 3.4 and 3.5 and table 3.2). Cyclic voltammograms obtained before and after this procedure employing the SECCM setup (shown in figure 3.3(A)) revealed a shift of +0.1 V for the ORR onset potential, but no significant change to the apparent

diffusion-limited current. CVs recorded on the HD sample after cleaning revealed a large variation in the currents obtained from different locations on the grid, probably due to the irregular distribution of the aggregated platinum NCs (*vide* figure 3.3(**B**)). Further tests were therefore carried out on as-deposited samples.

Linear sweep voltammograms, obtained with a SECCM setup (pipette tip with $d \approx 1\,\mu m$) from a 0.1 M $HClO_4$ solution, revealed ORR onset potentials of 0.7 V for the HD-HIE sample and 0.6 V *vs.* Pd/H for the LD-HIE and LD-LIE samples, and a HER onset potential of 0.05 V *vs.* Pd/H in all cases. All samples had broad kinetic or mixed control regions, due to the high mass transport rates for O_2. For the specimen with the high Pt loading, a plateau is reached at $E \approx 0.2\,V$, possibly due to blocking of active sites by adsorbed hydrogen. The apparent limiting current densities (normalised by the area of the SECCM tip) were *ca.* $2.7\,mA\,cm^{-2}$ and $0.3\,mA\,cm^{-2}$ for the HD and LD samples, respectively. This value is below the theoretical diffusion limited current density ($\approx 6\,mA\,cm^{-2}$) for a $4e^-$ process, indicating that ORR occurs *via* a $2e^-$ mechanism for the HD sample, and is kinetically limited for the LD samples. Further evidence for different mechanisms for the substrates with different platinum loadings is found when the currents are normalised by the Pt surface area (figure 3.6(**B**)), which shows that the current density obtained with the HD sample remained significantly higher than those obtained on the low density samples. The activities of the two LD samples were however very similar, confirming that the impact energy during deposition (i.e. strength of the adhesion of the clusters to the substrate) and the slightly different shapes (see figure 3.2) of the NCs donot have a significant effect on the catalysts' activity.

Repeat voltammetric scans revealed a degradation of the catalytic activity of the Pt NCs for all densities. This process was found to occur more rapidly when the Pt loading was lower (*vide* figure 3.7). Several degradation mechanisms were considered as reasons the decreasing catalytic performance: Pt dissolution, cluster migration-aggregation, Ostwald ripening, Pt surface poisoning, and carbon corrosion.

The effect of hydrogen peroxide was assessed by bringing droplets of 0.1 M $HClO_4$ solutions containing 1 mM and 5 mM H_2O_2 into contact with the surface of the LD-HIE sample and running CVs before and after a holding period, where the droplet was kept in contact with the substrate but without driving electrochemical reactions. Figure 3.9 shows that, after a 3 min contact period, no significant activity loss was found. However, when consecutive CVs were executed immediately after landing the tip, the apparent limiting current was reduced by $\approx$50% after $<$2 min, providing strong evidence that the loss of catalytic activity was not due to H_2O_2.

A statistical analysis of the samples using STEM images provided no evidence for significant particle coalescence (*vide* figure 3.13), platinum dissolution or NC detachment, even after extensive electrochemical cycling, suggesting that the degradation of the catalyst system must be caused by poisoning of the Pt surface.

Interestingly, significant particle movement was observed for the HIE sample (see figure 3.11). This was evidenced by a change in the spatial arrangement of the NCs, which aggregated to form groups up to more than 15 clusters. The NCs in such aggregates didnot touch, exhibiting instead centre-to-centre separations of *ca*. 4 - 5 nm, equivalent to $\approx$1.5 nm edge-to-edge distances. Similar patterns had been reported for soft-landed (0.1 eV per atom) Pt NCs on HOPG substrates in UHV. The most likely cause for such aggregates was found to be adsorbed lightweight species, most probably CO, in the HOPG/UHV study.

Finally, X-ray photoelectron spectroscopy was utilised to assess the changes to the chemical environment of carbon and platinum in the LD-HIE and HD-HIE samples, with the same procedures being performed on a bare TEM grid as a control. XPS spectra were recorded before and after carrying out 200 CVs at a scan rate $\nu = 0.2\,\mathrm{V\,s^{-1}}$ between $E_{cat} = 0\,\mathrm{V}$ and $E_{an} = 1.1\,\mathrm{V}$ *vs*. Pd/H, ending at the anodic potential.

Survey XPS spectra revealed platinum losses of *ca.* -80% and -34% for the LD and HD samples, respectively, as well as loss of carbon to a smaller extend, with accompanying increase in the oxygen content (*vide* table 3.5). The platinum was partially oxidised in both cases, but to a higher extent for the LD-HIE sample (table 3.6). This difference could not be explained solely by the different surface area to volume ratios of the two samples (due to the higher degree of merged Pt_{923} NCs at higher Pt loading - see table 3.7). Instead, this result indicates that the degradation of the platinum clusters is more severe at lower NC densities.

The carbon 1s spectra also provided evidence for more severe corrosion in the LD sample (see table 3.8), whereas the changes observed for the HD sample (listed in table 3.9) were comparable to those suffered by the control grid (table 3.10), with no platinum.

Overall, the evidence provided in this work strongly points to poisoning of the platinum surface as the cause for the decrease in the NC electrocatalytic activity toward the ORR. The degradation is worse for the samples with a very low Pt content ($\approx$5 - 6% surface coverage). The results presented in this chapter are in agreement with a mechanism in which reactive oxygen intermediates (ROIs), such as $^{\bullet}$OH and $^{\bullet}$OOH radicals, are formed as products of the ORR and attack the carbon substrate. This is promoted by the high mass transport rates and asymmetric flux of reactants and products (due to the increased O_2 flux from the liquid/air interface) in the SECCM setup. The corrosion of the carbon support results in the formation of carbon/oxygen groups (e.g. CO) which can be adsorbed on the platinum surface, poisoning the catalysts.

Chapter 4

Electrodeposition of Pt

The work presented in this chapter was done in collaboration with Dr. Cameron Bentley under the supervision of Prof. Pat Unwin of WEIG, University of Warwick, and it has been published in a peer-reviewed journal.[118] Dr. Cameron Bentley performed all electrochemistry experiments discussed in this chapter and prepared figure 4.1. All STEM imaging and analysis was carried out by the author.

Although the processes involved in nucleation and growth of metal nanoparticles on low energy substrates have been increasingly investigated in the past decade, much is still not fully understood, especially at the atomic scale. The state of the art in this field was reviewed in section 1.3. In this work, the possibilities of combining two powerful techniques, SECCM (section 2.2) with atmospheric control and *ex situ* HAADF-STEM (section 2.3), are explored to develop a novel, high-throughput methodology to study and obtain new insights into the electrodeposition of metals (i.e. platinum) onto a low energy substrate (i.e. amorphous carbon) under different conditions (deposition potential) at the atomic scale.

4.1 Electrochemistry

4.1.1 Electrodeposition of platinum by cyclic voltammetry

Cyclic voltammetry was used to test the electrodeposition of platinum onto amorphous carbon-coated gold TEM grids in the SECCM configuration ($d_{tip} = 1.6\,\mu m$; CVs shown in figures 4.1(A) and 4.2) and compared to the same process (reduction of Pt(II) to Pt(0)) on a macroscale glassy carbon (GC) electrode ($d_{GCE} = 0.95\,cm$) in a conventional 3-electrode cell (figure 4.1(B)). Please note that in figures 4.1(A) and 4.1(B) the current is normalised by the tip area ($A_{tip} = 2.0\,\mu m^2$) and by the electrode's geometrical area ($A_{GCE} = 0.707\,cm^2$), respectively, for easier comparison, and that all electrodeposition experiments were performed in argon-saturated solutions (absence of oxygen).

On the GC electrode (figure 4.1(B)), the CV presents a classical shape, with 2 sets of redox peaks (centred around $E = -0.49$ and $-0.58\,V$) which can be attributed to the reversible adsorption and desorption of hydrogen onto the platinum surface, and a reduction peak at $E = -0.67\,V$ corresponding to the reduction of Pt(II) to Pt(0). The current at the cathodic limit of the CVs, which is due to the evolution of hydrogen catalysed by Pt, grows strongly with each cycle in an initial phase (*ca.* first 4 cycles), and slows down with later cycles, reflecting the evolution of the platinum electroactive surface area.

In the case of the CCTG substrate and employing the SECCM technique (figures 4.1(A) and 4.2), the resulting CV lacks these classical elements: it can be seen in the inset of figure 4.2 that these characteristic platinum electrodeposition features (platinum reduction and hydrogen adsorprion/desorption) are absent. Instead, the only feature in these cyclic voltammograms is the reduction peak at $E \leq -0.6\,V$ *vs.* Pt(II)/Pt(0), which corresponds to the hydrogen evolution reaction (HER). Despite the lack of the characteristic features of an electrodeposition of a metal onto a low energy (i.e. carbon) support, the consistent increase

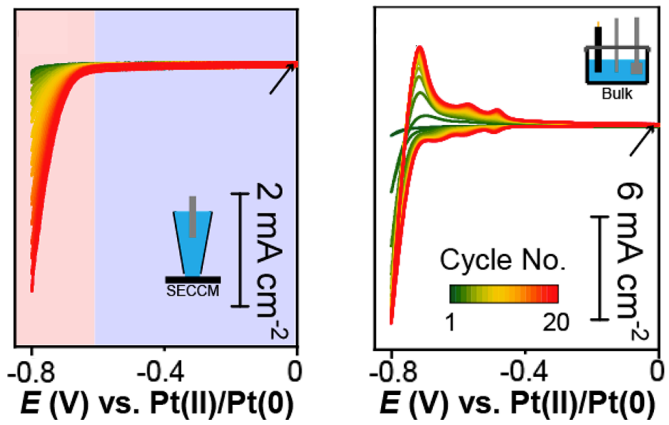

(A) CCTG, $d_{tip} = 1.6\,\mu m$. (B) GCE, $d = 0.95\,cm$.

FIGURE 4.1: CVs (20 cycles) recorded from an argon-saturated solution containing 1 mM $K_2[PtCl_4]$ in 0.1 M HCl at a scan rate $\nu = 0.5\,V\,s^{-1}$ on **(A)** carbon-covered TEM grids using a SECCM setup and on **(B)** a macroscale glassy carbon electrode. The pink ($E_{app} \leq -0.6\,V$) and purple ($E_{app} > -0.6\,V$) backgrounds in **(A)** indicate the potential region where HER does and does not take place. The arrows identify current density $J = 0$ and potential $E = 0$. Image adapted from [118].

in current magnitude with each cycle confirms that platinum is being deposited and that its surface area is growing with each CV cycle. The absence of the current peaks corresponding to hydrogen adsorption/desorption and platinum reduction is a consequence of the small quantities of deposited Pt on the TEM grid: the currents generated by these processes are too small relative to the nonfaradaic baseline current and are therefore indistinguishable from the background current on the CCTG electrode.

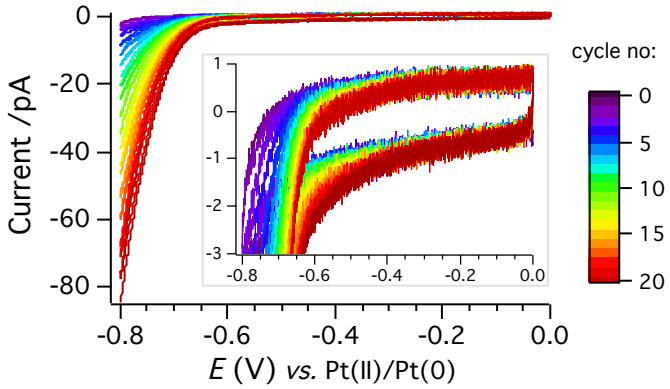

FIGURE 4.2: Representative CV obtained on CCTG from an Ar-saturated solution containing 1 mM $K_2[PtCl_4]$ in 0.1 M HCl at a scan rate $\nu = 0.5\,V\,s^{-1}$ with a SECCM tip with a 1.6 µm diameter. **Inset:** detail of the low current regions.

The slower growth rate on CCTG, evidenced by the much lower current density magnitudes obtained on this substrate, indicates that Pt nucleation kinetics is slower on this substrate than on GC. For example, after 2 cycles, the current density on the GC substrate at the cathodic limit, $J_{(-0.8V)}$ was $\approx$3.5 mA cm^{-2}. This current density is only reached on the TEM grid electrode after 18 cycles. Slower nucleation kinetics on CCTGs have been reported in the literature for Pt,[84] Pd[95] and Ag.[21]

4.1.2 Reproducibility of electrochemical experiments

A series of repeat cyclic voltammograms (CVs) were performed on the grid, in the vicinity of the potentiostatic electrodeposition experiments discussed in section 4.1.3 and in adjacent squares. This procedure was repeated 32 times in total. A representative CV is shown in figure 4.2. Initially, a potential of $E_{\text{tip}} = -0.5$ V was applied to the tip during approach ($E_{\text{app}} = +0.5$ V at the substrate upon contact), then the CV ran for 20 cycles between $E_{\text{cat}} = -0.8$ V and $E_{\text{an}} = 0$ V. Finally, the potential was ramped back to $E_{\text{surf}} = +0.5$ V ($E_{\text{tip}} = -0.5$ V) and the tip was retracted. An anodic value for E_{surf} during approach, $E_{\text{surf}} \geq +0.4$ V, was chosen to protect the electrode anodically and avoid the spontaneous deposition of platinum upon contact.[78].

In order to assess the reproducibility of the SECCM experiments on the TEM grid, the current at the cathodic limit for each cycle was compared for all repetitions. Figure 4.3**(A)** shows the average current at $E_{\text{cat}} = -0.8$ V ($I_{(-0.8\text{V})}$) for each cycle. For the last cycle, the sample standard deviation for the current represents 18% of the average current, showing good reproducibility of results using this methodology.

Figure 4.3**(B)** shows the *I-t* transients recorded at $E_{app} = -0.9$ V during three distinct potentiostatic electrodeposition experiments, revealing excellent agreement for these curves. A comparable similarity between CAs was found for every studied electrodeposition potential.

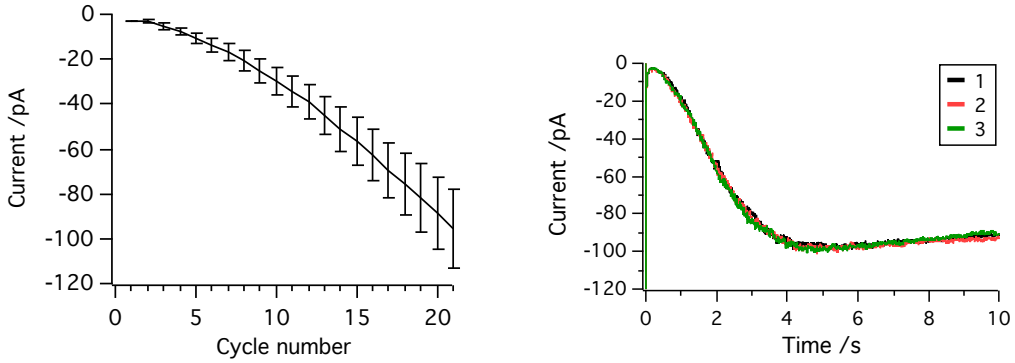

(A) Current at the cathodic limit for each CV cycle; average of 32 CVs.

(B) Potentiostatic electrodepositions.

FIGURE 4.3: (A) Average current at the cathodic limit ($E_{\text{cat}} = -0.8$ V *vs.* Pt(II)/Pt(0)) of the CVs for each cycle. The error bars indicate the sample standard deviation. (B) *I-t* transients obtained during 3 distinct chronoamperometric electrodepositions (t = 10s, $E_{app} = -0.9$ V).

4.1.3 Potentiostatic Electrodeposition

The electrodeposition of platinum was explored in more detail by chronoamperometry through a series of experiments where the potential was varied (from 0 V to –0.9 V, in 0.1 V steps) and the duration was held constant ($t = 10$ s). A hopping programme was employed for these experiments, where the depositions were performed in the pattern shown in figure 4.4. The resulting chronoamperograms (starting at $E_{app} = -0.3$ V) are depicted in figure 4.5. (The CAs for $E_{app} < -0.3$ V are very similar to that for $E_{app} = -0.3$ V.) Generally, for all *I-t* transients, there is a current spike as soon as contact is established, which lasts $\leq$12 ms. Such a current spike has often been attributed in the literature to the charging of the electrochemical double layer.[80, 82] When comparing the CAs, it can be seen that the current magnitude increases with overpotential, η (decreasing E_{app}).

For low overpotentials, $E_{app} > -0.6$ V (figure 4.5(A)), the current magnitude decreases with time, and the *I-t* transients stabilise at $I \approx 0$ after *ca.* 0.5 s

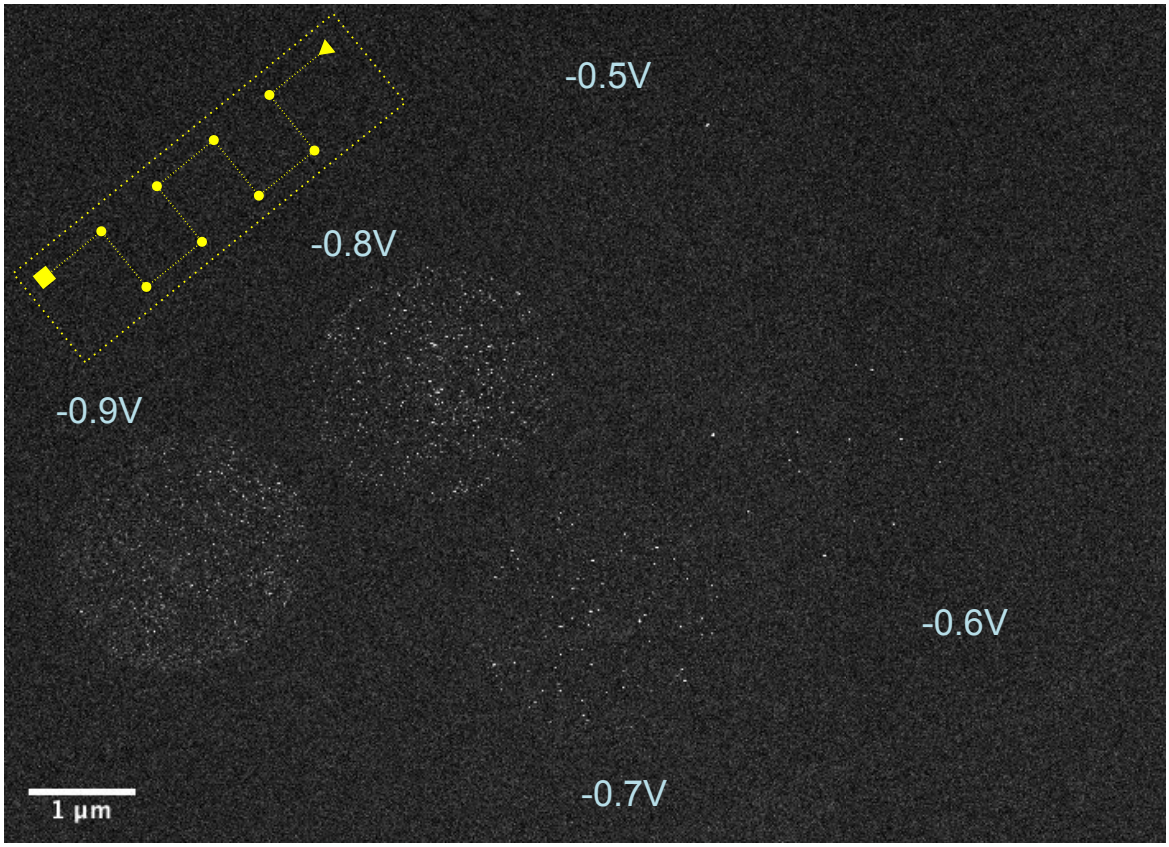

FIGURE 4.4: Low magnification (20k) HAADF-STEM images showing the landing areas for the 10 s potentiostatic EDs of platinum. Only $E_{app} \leq -0.6$ V generated platinum deposits that were visible at a low magnification. The yellow inset represents the pattern that the tip followed during the hopping programme; the triangle and square mark $E_{app} =$ 0 and –0.9 V, respectively.

The higher overpotentials are presented in figure 4.5(B). For $E_{app} = -0.6$ and –0.7 V, after the initial spike, the current increases with time for the duration of the applied pulse. For E_{app} -0.8 and –0.9 V, the current increase is stronger, and it reaches a plateau. For –0.8 V, this occurs at about 8 s, for –0.9 V, at *ca.* 4 s.

The current registered at potentials $E_{app} \leq -0.6$ V can be attributed to the hydrogen evolution reaction (HER) and the contribution of platinum reduction can be assumed to be negligible relative to I_{HER}, as evidenced by the CV (*vide* discussion around figure 4.2 in section 4.1.1), which lacks features other than HER.

Although the currents obtained during chronoamperograms with $E_{app} \leq -0.6\,\mathrm{V}$ cannot be used to quantify the electrodeposited platinum (by integrating the current relative to the pulse duration to calculate the charge) due to being predominantly generated by the hydrogen evolution reaction, it can be used as a reflection of the evolution of the electrochemically active platinum area, because HER is primarily a surface controlled process. Therefore, the behaviour of the *I-t* transients at the highest overpotentials studied in this work indicates that, as Pt is deposited, the electrochemically active surface area grows up to a limit, remains stable for a short time, and, in the case of the highest overpotential studied here, finally decreases very slowly.

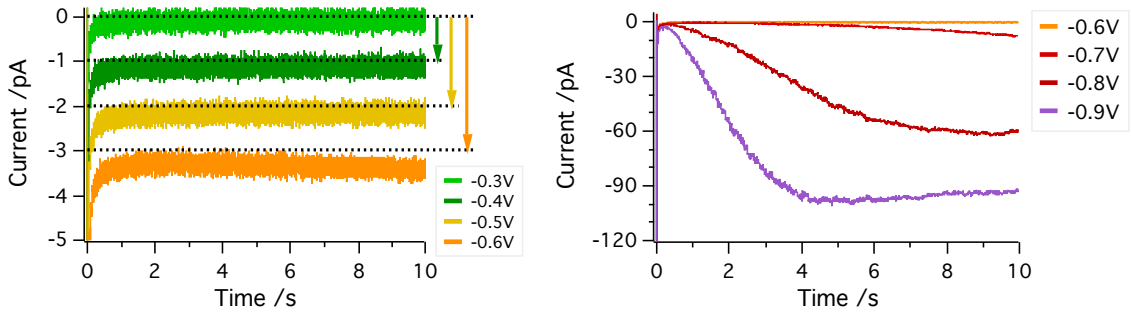

(A) ED at low overpotentials. Please note that the *I-t* transients are offset in the *y* direction, as indicated by the arrows.

(B) ED at high overpotentials.

FIGURE 4.5: Chronoamperograms corresponding to the potentiostatic electrodeposition of platinum at different potentials ($t_{app} = 10\mathrm{s}$).

The plateauing of the current at $E_{app} = -0.8$ and $-0.9\,\mathrm{V}$, which reflects a stalling in the growth of the available platinum surface area, could be caused by the blocking of nucleation sites by adsorbed hydrogen (H_{ads}) or by H_2 nanobubbles, or due to the decrease in the (platinum) surface area despite continued growth of the platinum deposits. Hydrogen is known to adsorb onto platinum surfaces, and has been shown to impede the addition of Pt onto Pt structures (self-terminating growth)[183] however, classical nucleation and growth theory predicts that metal nuclei will grow for as long as a driving force (i.e. negative

overpotential) is applied and H_{ads} would not prevent the deposition of Pt onto the carbon support. Hydrogen nanobubble nucleation,[184] generated during the HER, is also unlikely to block the electrode's surface in this case (the carbon film and deposited Pt particles) due to the fast gas exchange across the gas-liquid interface that occurs in the droplet-cell configuration,[137, 185] which encourages detachment. Furthermore, STEM imaging suggests that platinum nucleation and growth occurs throughout the duration of the applied pulse (*vide* section 4.2). Instead, it is more plausible that, after a certain quantity or concentration of platinum is reached on the substrate, aggregation processes,[78, 84] leading to a decrease in Pt surface area, become dominant relative to parallel nucleation and growth. This proposition is supported by the STEM data, which will be explored in the following section.

4.2 STEM imaging and analysis

STEM is a powerful tool to investigate the characteristics of electrodeposited metals due to its large dynamic magnification range, especially when combined with SECCM, where the contact area between the droplet and substrate encompasses only up to a few μm^2. At the lowest magnification with our microscope (*vide* section 2.3.2), 20k, which records images with areas of $7.87 \times 7.87\,\mu m^2$, the entire droplet area can be imaged, providing a good overview of the area of interest, as shown in figure 4.4. At very high magnifications ($\geq$10 M) subatomic resolution is obtained, revealing the atomic structure of the deposited NPs and clusters, as well the presence of single atoms. Such images can be utilised to gain an atomistic view of electrochemical nucleation and growth.[84, 89, 186] Magnifications higher than 15 M are possible, but this increases undesirable beam effects such as contamination[187], damage to the integrity of the carbon film, changes to the morphology of deposits, and knocking out of atoms from clusters and NPs (*vide* section 4.2.1), and were therefore avoided in this work.

In this chapter, magnifications of 50 k and 20 k are referred to as "very low", 250 k and 500 k as "low", 1 M - 5 M as "high, and $\geq$10 M as "very high" magnification. Very low and very high magnification images were employed for the purposes stated above. Low magnifications (250 k - 500 k) were used to obtain statistical information on particles (particle number density, size distribution, spatial distribution on the substrate). High magnifications provide valuable structural information about medium-sized and larger NPs.

Furthermore, the intensity in HAADF-STEM (also known as *Z*-contrast) imaging, is dependent on the atomic number and thickness of the species being investigated, and this allows the quantification of the deposited platinum, as described in section 2.4.1. All of these qualities of STEM will be made use of in this section in order to understand the processes that govern the electrodeposition of platinum under different conditions.

4.2.1 Effect of the electron beam

It is possible for the highly focused electron beam during STEM imaging to damage samples. In metal specimens, the irradiation can cause single atoms to be knocked out of their atomic site.[127] This effect is stronger for higher magnifications. In order to assess the effect of the electron beam of our STEM on platinum NCs, a cluster was continuously imaged, at 15 M magnification, during, approximately, 35 min.

The background-corrected integrated intensity of this cluster was calculated for each of the images in this sequence. In order to do this, first, the background intensity was measured in platinum-free areas of each image and normalised by the sampled area to obtain an intensity density ($\text{IntDen}_{\text{BG}}$). The average of all $\text{IntDen}_{\text{BG}}$ values was used for further calculations in this subsection. Then, the boundaries of the cluster were defined for each image by manual thresholding, excluding adjacent atoms from the cluster area. Finally, the

background-corrected cluster intensity was obtained from the following equation:

$$I_{\mathrm{cl}} = I_{\mathrm{cl,\ raw}} - A_{\mathrm{cl}} \times \mathrm{IntDen_{BG}} \tag{4.1}$$

where I_{cl} is the cluster's background corrected integrated intensity, $I_{\mathrm{cl,\ raw}}$ is the cluster's "raw" (as extracted from the image) integrated intensity, and A_{cl} is the cluster's projected (2D) area.

Figures 4.6 (A) - (D) display a sequence of images that were taken during this experiment and illustrate the changes that the cluster undergoes due the highly focused irradiation. Figure 4.6(**E**) shows the evolution of the cluster background-corrected integrated intensity with time.

I_{cl} is proportional to the number of atoms (i.e. volume) of the cluster, and was therefore used as a measure for the total amount of platinum and its evolution with irradiation duration. The graph in figure 4.6(**E**) reveals that the cluster's intensity decreases with irradiation time: I_{cl} (i.e. mass) loss for the NC happens at a rate of ≈0.43% per minute. After 35 min of being exposed to the highly focused electron beam, the cluster has lost ≈14.5% of its volume, and an increased number of single Pt atoms can be seen surrounding it.

Typically, images used for the work presented in this thesis were recorded with a dwell time of 38 µs, and a very high magnification image (10 M - 15 M) is taken right after the beam's focus has been optimised (generally only a few seconds in areas of interest), in order to minimise both beam effects on the platinum and contamination build-up. It is therefore reasonable to assume that some of the single atoms surrounding Pt NPs and clusters are knocked out of the NP due to the e-beam. However, even after an extremely long time (35 min, over 50 times longer than under "normal" imaging conditions, assuming a 30 s "re-focus time" and taking the imaging time (10 s) into account), most of the single Pt atoms can be found within a ≈5 nm radius from the edge of the cluster (*vide* figures 4.6(**F**) and 4.6(**G**)). In contrast, for the images with the electrodeposited platinum, single atoms can be

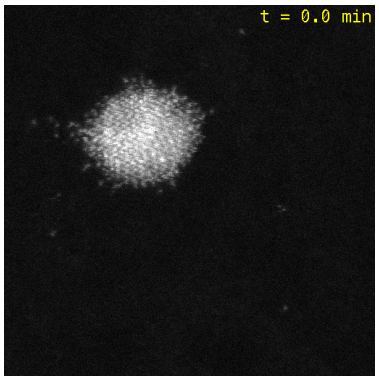

(A) $t = 0$ min, 100% Pt.

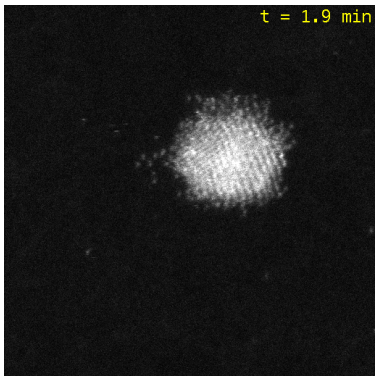

(B) $t = 2$ min, 98.6% Pt.

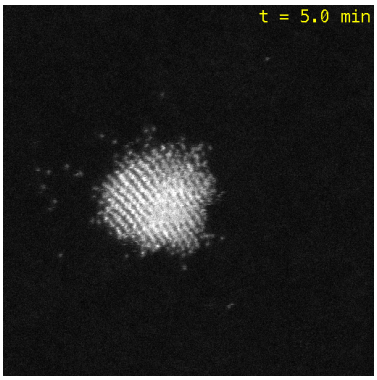

(C) $t = 5$ min, 96.3% Pt.

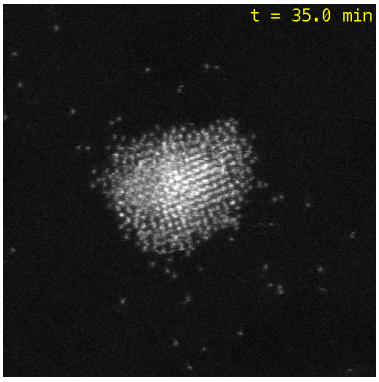

(D) $t = 35$ min, 85.5% Pt.

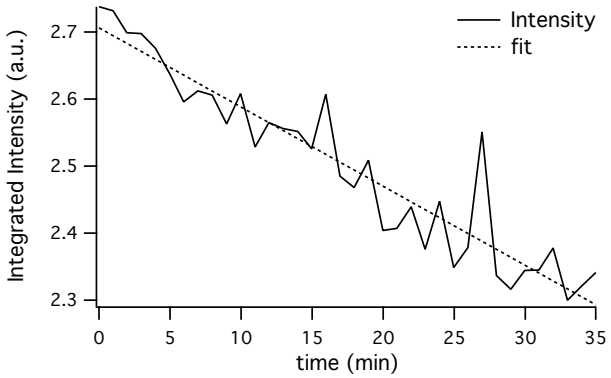

(E) Cluster integrated intensity *vs.* time.

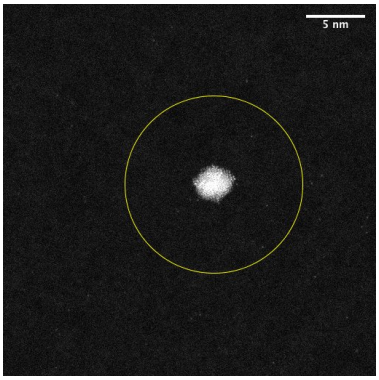

(F) Before.

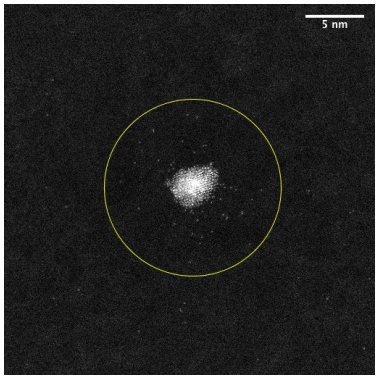

(G) After.

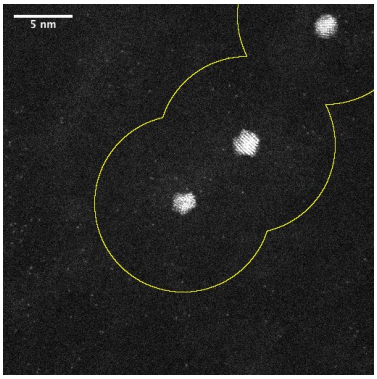

(H) Control.

FIGURE 4.6: (A) - (D): Sequence of images taken of the same cluster as it was exposed to the highly focused electron beam, at 15 M magnification, for *ca.* 35 min. **(E):** Evolution of the cluster integrated intensity with time during continuous imaging at 15 M magnification. **(F) - (H):** High (5 M) magnification images of the same cluster taken before **(F)** and after **(G)** the continuous imaging at 15 M, and of control clusters **(H)** from a different area on the grid, not exposed to prolonged e-beam irradiation. The yellow shapes delimit an area with a ≈15 nm diameter surrounding each cluster.

found at greater distances than that around particles that were not irradiated for very long periods, as can be seen in figure 4.6(H).

4.2.2 Quantification of the electrodeposited platinum

Low magnification images (250 k) were used to carry out a statistical analysis of the particle size. This will be discussed in more detail in section 4.2.4, and representative low magnification images are shown in figure 4.8. Due to the irregular shapes and spatial distribution of the deposited NPs, it was impossible to extract an intensity for the background (BG) surrounding each particle, and the value calculated from high magnification images, as described in chapter 2, section 2.4.1, was utilised.

A threshold was set manually for each 250 k image to distinguish the carbon from the platinum, and the integrated intensity, area, location and shape parameters were extracted from each particle (or object). Objects touching the edges of the images were excluded for the purposes of particle size analysis but included to estimate the total Pt mass in each meniscus footprint (*vide infra*). The number of platinum atoms in each particle, N_{Pt}, was estimated according to the following equation:

$$N_{\mathrm{Pt}} = \frac{II_{\mathrm{NP}} - ID_{\mathrm{BG}} \cdot A_{\mathrm{NP}}}{II_{\mathrm{Pt}}} \tag{4.2}$$

where N is the number of atoms, II is the integrated intensity, ID the integrated intensity density, and A the area. The subscripts NP, BG and Pt denote "nanoparticle", "background" and "platinum", respectively. The integrated intensity of single Pt atoms, II_{Pt} was calculated as described in section 2.4.1.

The mass of each particle was calculated using the estimated number of atoms in each NP and the mass of a single platinum atom (3.24×10^{-22} g). The size distribution and particle density obtained from the 250 k images was assumed to be representative of the whole

meniscus area, and the total deposited Pt mass was calculated using the droplet area obtained as described in section 2.4.3.

The estimated total platinum mass for the footprints left behind by the SECCM droplet for each of the studied electrodeposition potentials is given in table 4.1, page 130.

4.2.3 Morphology

Figure 4.7 shows high magnification images which are representative of the full range of morphologies that were observed after 10 s electrodepositions. Ustarroz and coworkers[78, 84] have reported differences in morphology for platinum deposited at lower and higher overpotentials, with the latter being smoother and the former more porous (*vide* subsection 1.3.2.2, figure 1.9). However, no obvious trends in particle morphology could be identified in this work, probably because of the shorter electrodeposition time.

Independently of E_{app}, high magnification STEM images reveal that generally, the smallest clusters ($d \lessapprox 2$ nm) lack a well-defined structure (e.g. cluster 1 in figure 4.7**(A)**, $d =$ 2.0 nm) , medium sized clusters tend to be monocrystalline (such as cluster 2 in 4.7**(A)**, $d =$ 2.4 nm, and the smallest cluster in figure 4.7**(B)**), and, starting at about $d \gtrapprox 4$ nm, one or more grain boundaries become apparent within the same particle (figures 4.7**(B)**-4.7**(D)**). A particle's morphology seems to become more irregular and complex, with higher porosity, the larger its size. Based on their structure, larger particles seem to be constructed through the aggregation of smaller clusters, in agreement with an aggregative growth mechanism.[78, 84]

Interestingly, single Pt atoms were found surrounding all NPs, indenpendently of size or electrodeposition potential, as exemplified in the images shown in figure 4.7. The frequency of these atoms doesnot seem to depend on their vicinity to larger structures and can be seen at distances $\gg$5 nm, indicating that they must have been generated during the electrodeposition

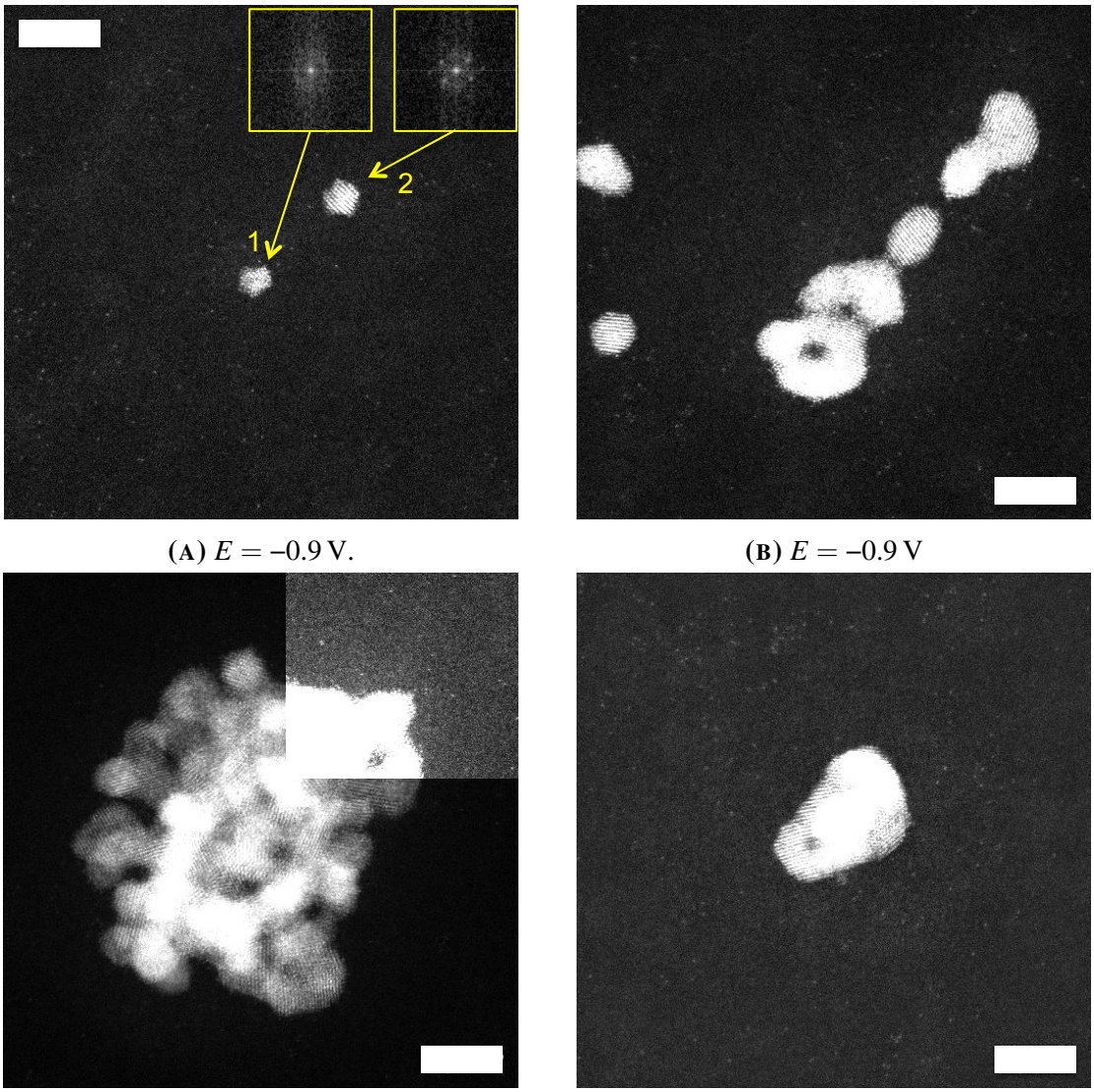

(A) $E = -0.9\,\mathrm{V}$. **(B)** $E = -0.9\,\mathrm{V}$

(C) $E = -0.6\,\mathrm{V}$ **(D)** $E = -0.5\,\mathrm{V}$

FIGURE 4.7: Representative images of the range of morphologies found after 10 s electrodepositions. Images taken at (A) $E = -0.9\,\mathrm{V}$ (insets: FFT of the indicated clusters), (B) $E = -0.9\,\mathrm{V}$, (C) $E = -0.6\,\mathrm{V}$ (upper right corner: overlay of the same image, but with different brightness and contrast settings), (D) $E = -0.5\,\mathrm{V}$; all images were taken at 5M magnification. The scale bars indicate 5 nm.

process, as opposed to being a product of beam damage to nearby clusters. Again, this finding is consistent with a nucleation-aggregative growth mechanism in which the direct addition of atoms onto growing nuclei is disfavoured. In such a scenario,[84] the reduction and adsorption of Pt atoms on the carbon substrate would be encouraged, leading to their presence throughout the meniscus contact area, as has been observed here.

4.2.4 Size Distribution

The particle size analyses were performed using data extracted from images recorded at a low magnification (250 k), in order to include a large enough number of particles to obtain statistically-relevant information. At this magnification, each image encompasses an area of *ca.* 0.4 μm^2, and at least 3 images were used for each potential for this analysis, so that the total analysed area was at least 28% of the total droplet footprint. Figure 4.8 shows examples of the images utilised for each electrodeposition potential.

Due to the lower amount of Pt NPs deposited at $E_{app} < -0.6$ V, the resulting particles could not be resolved at a low magnification. Consequently, no statistical information could be extracted from electrodepositions carried out at low overpotentials.

Visual inspection of figure 4.8 reveals that the total amount of deposited platinum increases with overpotential, strongly from $E_{app} = -0.6$ V to −0.8 V, then only weakly from $E_{app} = -0.8$ V to $E_{app} = -0.9$ V. This is in good agreement with the electrochemical data, considering the current registered at the end of the chronoamperograms as a measure of the available platinum area. At $t = 10$ s, the currents are ≈ -0.3, -10, -60 and −90 pA for $E_{app} = -0.6$, -0.7, -0.8 and -0.9 V, respectively (*vide* figure 4.5 and table 4.1). The images also show that the projected area of the largest particles decreases with increasing η, while the number of small particles increases.

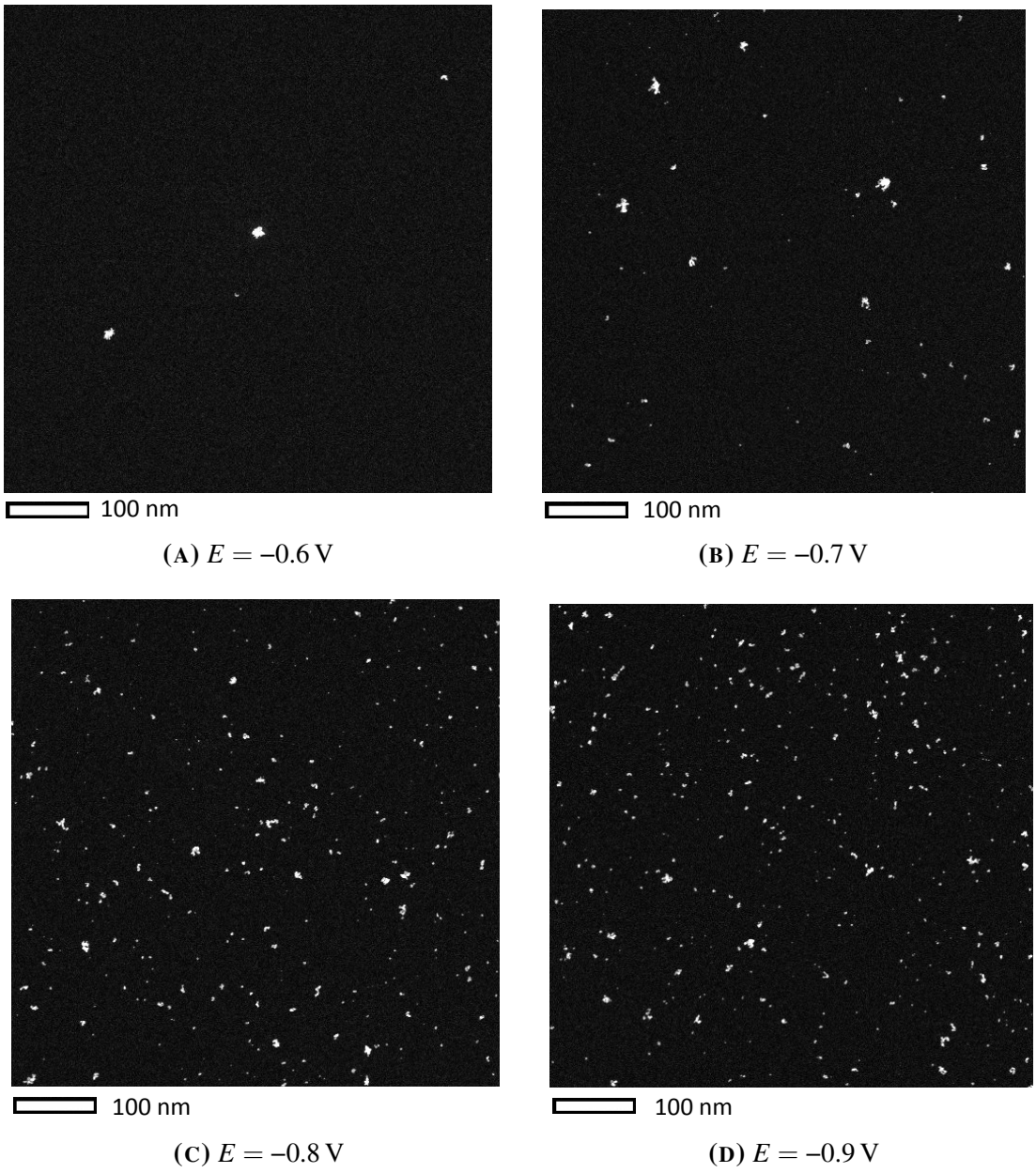

(A) $E = -0.6\,\mathrm{V}$ (B) $E = -0.7\,\mathrm{V}$

(C) $E = -0.8\,\mathrm{V}$ (D) $E = -0.9\,\mathrm{V}$

FIGURE 4.8: Representative images, taken at 250k magnification, of platinum electrodeposited for $t = 10\,\mathrm{s}$ at different potentials.

In order to verify these observations, the size of the deposited particles was analysed statistically. Two parameters were studied as a function of the applied electrodeposition potential: particle diameter (calculated from the projected area and assuming spherical particles),* and the number of platinum atoms per particle (calculated as described in section 4.2.2).

The statistical analysis of these images confirm the observations noted above, and are summarised in the graphs presented in figure 4.9 and in table 4.1 - figures 4.9**(A)** and 4.9**(C)** show a breakdown of the relative abundance of particles of different sizes (expressed as particle diameter and constituent atoms, respectively), figure 4.9**(B)** displays the average particle diameter and its dispersion, and figure 4.9**(D)** shows the cumulative histogram of the number of platinum atoms per particle. It is worth noting that there isnot a linear relationship between a particle's cubed diameter (or radius) and its number of constituent atoms ($\propto$ volume) because the particle shapes are irregular (i.e. not spherical). Consequently, the information that can be obtained from the histograms in figures 4.9**(A)** and 4.9**(C)** isnot identical.

The graph in figure 4.9**(B)**, which depicts the average particle diameter as a function of deposition potential, confirms the observation made above, that, overall, the particle size decreases with increasing overpotential. It also reveals that the size dispersion decreases as well, resulting in a narrower size distribution at $E_{app} = -0.9$ V than at -0.6 V *vs.* Pt(II)/Pt(0).

Inspecting the breakdown of relative frequency of each size (figure 4.9**(A)**), it can be seen that, at every analysed electrodeposition potential, there is a bimodal size distribution, with a narrow peak at small particle sizes ($d \leq 2$ nm), and a broad wave at larger sizes. This is consistent with the literature.[84] At the lowest overpotential, the majority of particles (*ca.* 60%) belongs to the smallest size category. The broad wave peaks at 4.5 nm, and about 10% of all particles have diameters larger than 10 nm. At the other end of the E_{app} range,

*Although the electrodeposited Pt NPs and NCs are not spheres, especially at larger sizes, the particle diameter was chosen to illustrate the size distribution because it is more commonly used in the relevant literature. Reporting size in this manner makes it easier to compare these results with those reported elsewhere.

for −0.9 V, only approximately 30% of all particles belong to the smallest category, and the broad peak in the histogram (for the larger sizes) is asymmetrical, peaking at 3.5 nm and decaying slowly at larger sizes. The percentage of particles with diameters greater than 10 nm is negligible. The size distribution for −0.8 V is very similar to that for −0.9 V; the shape of the histogram for −0.7 V is intermediate between those obtained for higher and lower overpotentials. This is most obvious in the cumulative histogram depicted in figure 4.9**(D)**. The largest particle diameters observed were 21.3, 21.0, 13.8, and 13.4 nm for $E_{app} = -0.6$, -0.7, -0.8 and −0.9 V, respectively (see table 4.1).

The distributions of number of platinum atoms per particle (figures 4.9**(C)** and 4.9**(D)**) follow the same patterns as those for particle diameter. It is interesting to note that the overwhelming majority of "small" particles has only up to 200 constituent atoms, while the frequency of particles with 200 to 500 atoms is comparatively low (only up to 5% for each additional 100 atoms). This suggests that the Pt growth inhibition (self-limiting mechanism) becomes dominant once Pt particles reach $\leq$ 200 atoms, especially at lower overpotentials.

The bimodal size distribution of the platinum particles, observed for all deposition potentials studied here, and the broader size distribution for larger ($d \gtrapprox 2$ nm) NPs for higher overpotentials are in good agreement with an aggregative growth mechanism, first reported by Ustarroz and collaborators[78, 84]. Furthermore, it is shown that the small, "primary" clusters, are limited to ≈200 constituent atoms in the case of platinum. Taking the morphological information obtained from high magnification images (4.7) into account, which revealed that a diameter of $d \approx 2$ nm is a critical size at which amorphous clusters change into a monocrystalline structure, it is reasonable to assume that the self-limiting growth mechanism is related to this size-dependent structural transition.

The effect of E_{app} on the Faradaic efficiency is sometimes analysed in electrodeposition studies. Unfortunately, this analysis could not be performed in this case because reliable data about the Pt deposits could only be extracted from the STEM images for high overpotentials

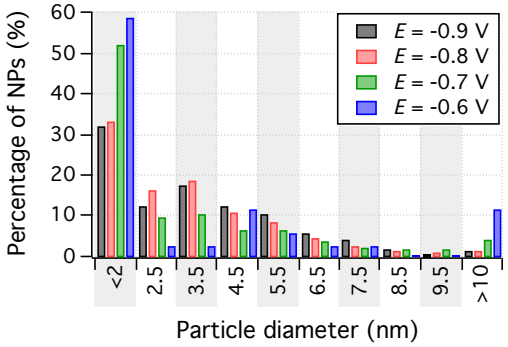

(A) Particle diameter histograms.

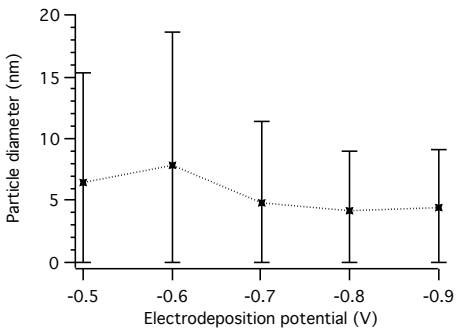

(B) Average particle diametre.

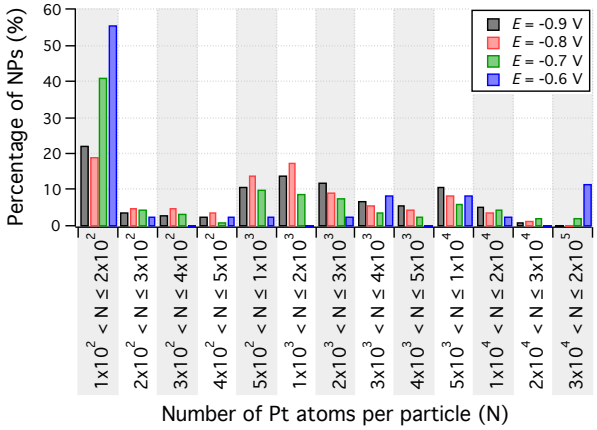

(C) Histograms of number of platinum atoms per particle.

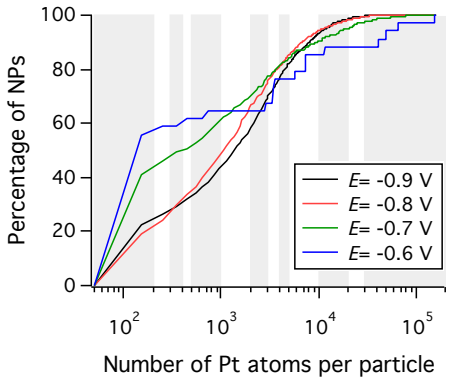

(D) Cumulative size (number of Pt atoms per particle) histogram. The grey and white areas in the background coincide with the bins in **(C)**.

FIGURE 4.9: Size distribution of the electrodeposited platinum at different applied potentials ($t = 10$ s).

($E_{app} \leq -0.6$ V), and a charge for the electrodeposition of platinum cannot be calculated from the chronoamperograms recorded at $E_{app} \leq -0.7$ V because of the current contribution from the hydrogen evolution reaction.

Table 4.1 summarises the results presented in this chapter, listing the particle number density, average and maximum particle diameter, estimated total platinum mass deposited at each potential, and the current measured at $t = 10$ s for every chronoamperogram. It also includes data obtained from two distinct droplet areas where electrodepositions were performed at $E_{app} = -0.6$ V (experiments A and B). Although the NP density for droplet B

is 30% higher than that of A, the values are within one standard deviation of each other, and all other parameters are in good agreement (the average particle size is ≈7% larger for A than B, resulting in a very close value for m_{Pt}.)

TABLE 4.1: Particle number density, average and maximum diameter (d), total estimated deposited platinum mass (m_{Pt}) and current at the end of the electrodeposition CA ($I_{10\,\mathrm{s}}$) for each of the studied deposition potentials (E_{app}).

E_{app} (V)	NP density (μm^{-2})	average d (nm)	maximum d (nm)	m_{Pt} (10^{-15} g)	$I_{10\,\mathrm{s}}$ (pA)
-0.9	1236 ± 20	4.4 ± 7.8	13.4	5.4 ± 0.4	-90
-0.8	978 ± 26	4.2 ± 7.3	13.8	3.9 ± 0.4	-60
-0.7	264 ± 11	4.8 ± 10.7	21.0	1.6 ± 0.2	-10
-0.6 (A)	20 ± 11	7.8 ± 10.7	21.0	0.41 ± 0.17	-0.3
-0.6 (B)	26 ± 9	7.3 ± 6.4	21.3	0.42 ± 0.23	-0.3

4.3 Summary and Conclusions

In this chapter, a novel methodology was presented, which allows the performance of series of localised electrochemical (i.e. SECCM) experiments, where several experimental parameters can be varied to be studied systematically, and under environmental control (i.e. inert gas atmosphere). The locations of these experiments can then be identified by *ex situ* high resolution microscopy (i.e. HAADF-STEM) and electrochemical parameters can be correlated with characteristics, depending on the experiments and materials, such as particle number density, size distribution, spatial distribution of specific species, particle morphology or change in total (estimated) mass. The electrodeposition of platinum from an acid solution under different potentials was chosen as a model system for this work, but other experiments and additional parameters could be investigated using this methodology.

Cyclic voltammetric experiments performed employing the CCTG/SECCM configuration revealed sluggish kinetics relative to the same reaction on a macroscale GC electrode (figure 4.1). The CVs lacked the classical features (a reduction wave due to the reduction of Pt(II) and pairs of redox peaks corresponding to the reversible adsorption/desorption of hydrogen onto the surface of deposited platinum) usually registered during the electrochemical deposition of this metal, but the growth of Pt deposits was evidenced by the steady increase in the current magnitude at $E_{app} \leq -0.6$ V *vs.* Pt(II)/Pt(0) due to the HER (figure 4.2).

The deposition of platinum was investigated in more detail by chronoamperometry. A "hopping" programme was employed to perform electrodeposition experiments in a sequence of 3 µm "hops", where the applied potential was varied between 0 and −0.9 V *vs.* Pt(II)/Pt(0) in −0.1 V steps, following the pattern shown in figure 4.4.

Comparison of repeat experiments, voltammetric (figure 4.3**(A)**) and chronoamperometric (figure 4.3**(B)**), revealed good to excellent reproducibility of the electrochemical response obtained with this system.

The *I-t* transients registered during the electrodeposition experiments had nonclassical shapes. At low overpotentials ($E_{app} > -0.6$ V; figure 4.5**(A)**) the current decreased sharply after an initial peak, attributed to double layer charging, and reached $I = 0$ after ≈0.5 s. At higher overpotentials (figure 4.5**(B)**), $E_{app} \leq -0.6$ V, the current can predominantly be attributed to HER. For −0.6 and −0.7 V, there is a steady increase of I with time for the entire duration of the experiment (after the initial peak). For the highest overpotentials, the current plateaus after ≈4 s and ≈8 s for −0.8 and −0.9 V, respectively. The most probable cause for this behaviour is the dominance of an aggregative mechanism (in parallel with continued nucleation of new clusters) after a certain quantity or density of deposits is reached, in agreement with the general nucleation and aggregative growth model first proposed by Ustarroz and coworkers.[78, 84]

HAADF-STEM images provided further evidence for parallel nucleation and aggregative growth processes. High magnification images (figure 4.7) revealed the coexistence of single Pt atoms, small ($d \leq 2\,\text{nm}$) amorphous clusters, monocrystalline NCs ($2\,\text{nm} \leq d \leq 4\,\text{nm}$), and polycrystalline NPs ($d > 4\,\text{nm}$) at all studied electrodeposition potentials. The single atoms were observed throughout the meniscus contact area, and no correlation could be established between their presence and that of NCs, and it was shown that these atoms could not have been generated by the electron beam (section 2.2.1). Interestingly, the presence of single atoms (along with amorphous and structured clusters) was also reported for the potentiostatic electrodeposition of gold at short ED times ($t \leq 30\,\text{ms}$).[186] It is possible that atoms are deposited onto the carbon substrate due to the self-limiting mechanism that prevents the direct addition of atoms onto clusters after a critical size.

A statistical analysis of the size distribution of particles deposited at $E_{app} \leq -0.6\,\text{V}$ *vs.* Pt(II)/Pt(0) revealed bimodal size distributions for all potentials, with a sharper peak (in the histograms) for "small clusters" with $d < 2\,\text{nm}$ ($N < 200$) and a broader one for larger species. The separation between these two size groups was stronger for $E_{app} = -0.6\,\text{V}$ and softer for the highest overpotentials.

A bimodal distribution has also been reported by Ustarroz *et al.*[78, 84] and is indicative of a mechanism where initially, nucleation and growth by direct incorporation of new atoms takes place. Once these small clusters reach a certain size ($d \approx 2\,\text{nm}$ or $N \approx 200$ atoms for Pt), further growth by direct addition is inhibited (self-limiting growth mechanism)[183] and can only occur through aggregation.

In this work, it was possible to correlate the diameter of the "small" clusters ($d \leq 2\,\text{nm}$) with the number of constituent atoms (up to ≈200 atoms) and with a structural transition from amorphous to structured. This implies that the self-limiting mechanism, which prevents the growth of such small particles by direct addition, must be tied to the cluster's atomic structure.

The lower percentage of small clusters and the broader wave for larger particles at higher overpotentials (figures 4.9(A) and 4.9(C)) suggests that the aggregation of primary clusters is accelerated at more cathodic potentials. This could be due to the greater concentration of primary clusters, higher mobility, faster recrystallisation,[84] or a combination of these factors. Pt NPs deposited at higher overpotentials also have a narrower size dispersion (4.9(B)) than those resulting from lower overpotentials. In part, this is due to the smaller proportion of "small" NCs, but also, the largest NPs generated at $E_{app} = -0.8$ and -0.9 V are significantly smaller ($<$14 nm) than those originating with lower overpotentials ($\approx$21 nm; see table 4.1). The narrower size distribution under high overpotentials may be due to faster aggregation of clusters.

Particle number density and total deposited Pt mass were also extracted from the STEM images (see table 4.1). These results are in good agreement with the relative magnitudes of the currents at the end of the electrodeposition pulse, which reflects the electrochemically active (Pt) surface area.

In conclusion, the work presented in this chapter has shown the feasibility of a new methodology to combine environmentally-controlled SECCM with HAADF-STEM, and has provided new insights into the atomistic processes which dominate the nucleation and growth processes during the electrodeposition of platinum. Notably, it has allowed a correlation to be established between cluster size, number of constituent atoms and structure to a self-limiting growth mechanism which sets in once NCs reach $d \approx 2$ nm. Furthermore, this combination of techniques offers the possibility to systematically study the effects of several electrochemical parameters (e.g. applied potential, time, combination of pulses in chronoamperometry or potential range, scan rate and number of cycles in voltammetry) and to correlate electrochemical data with statistical (i.e. particle size and spatial distribution), structural (i.e. particle morphology) and quantitative (i.e. atom counting) information obtained at the nano- and subatomic scale.

Chapter 5

Conclusions

Platinum electrocatalysts are vital to green and energy-related technologies. Because this metal is so rare and costly, there is a drive to understand the mechanisms of the reactions which it catalyses, as well as to develop methods of generating Pt nanoparticles with good control over size, shape, and NP density, so that the platinum mass activity can be optimised, reducing costs.

With the development of more refined techniques in electrochemistry, microscopy and NP synthesis, discrepancies have been found between traditional models and experimental outcomes. For example, in studies of Pt NPs as a catalysts for the ORR, the effect of the particle size for small Pt clusters ($d \lessapprox 5\,\text{nm}$) and the role of the interparticle distance are still not fully understood. In electrodeposition studies, contradictions between the classical nucleation and growth theories and experimental results, especially in the early stages, have lead to the proposal of new models, which are still under debate.

The work in this thesis aims to gain a better understanding of Pt at the nanoscale through the study of well-defined and well-characterised systems. For that reason, carbon-coated gold TEM grids (CCTGs) have been employed as supports for localised electrochemical

experiments, performed in a SECCM configuration, and correlated with aberration-corrected HAADF-STEM imaging. The objective was twofold: to obtain new insights into the relation between structure and electrochemical properties of platinum nanostructures through the combination of these two techniques, and to demonstrate the potential of the SECCM/STEM platform to acquire information about the studied systems at the nano and subatomic scale.

SECCM can use any semiconducting or conducting surface as a working electrode, however, for STEM, the material must be transparent to the electron beam, which limits its thickness. Commercially available TEM grid coating materials include formvar (a polymer), different types of carbon (lacey, holey, or continuous amorphous carbon films), silicon monoxide, dioxide, and nitride, graphene oxide and metallic thin films (Au, Pt, Pd). Usually, such films have thicknesses around $30-50\,\text{nm}$, however, films as thin as $3\,\text{nm}$ (e.g. ultra-thin carbon support films and metallic thin films) and as thick as $500\,\text{nm}$ (e.g. silicon nitride) are also available.[188, 189] Each film material and thickness has advantages and disadvantages, which must be weighed when designing experiments, e.g. resistance to being manipulated, stability under the electron beam (depending on the beam acceleration), thickness of the film relative to that of the materials being studied, and hydrophilicity. For the grid itself, considerations include resistance to chemicals and mesh size, which can also affect the stability of the coating.

CCTGs present some challenges, especially related to their fragility and cleaning before experiments. For example, ozone/UV TEM cleaners can affect the film's hydrophilicity, which affects the size and stability of the droplet during SECCM experiments, and electrochemical cleaning can corrode the film, making it less resistant to manipulation. However, amorphous carbon films were selected for this work due to their relevance to fuel cells, which usually employ high surface area carbon supports, and for consistency with studies about electrodeposition of Pt, which tend to employ carbon supports as well.

Two systems were investigated in detail in this thesis: the degradation of platinum catalysts after driving the ORR (chapter 3), and the electrodeposition of Pt (chapter 4).

In chapter 3, well-defined and characterised ensembles of mass-selected Pt_{923} ($d \approx 3$ nm) were employed to study the ORR under high mass transport rates and low platinum loadings, comparable to those found in fuel cell cathodes. The catalytic activity of the samples was found to degrade with consecutive voltammetric scans, and the effect was worse for the samples with lower platinum loading. No significant differences were observed between the LD-HIE and LD-LIE samples, indicating that the strength of adherence of the clusters to the substrate had no influence in their catalytic activity. The causes for the loss in performance were explored employing STEM and XPS. Several mechanisms were considered, including platinum loss, NC detachment, migration-aggregation, Ostwald ripening and poisoning of the Pt surface. HAADF-STEM imaging exposed an increase in brightness in the meniscus-substrate contact areas, indicating changes to the carbon film after ORR. A thorough statistical analysis of the clusters in areas where the ORR had been driven and in nearby, pristine areas (equivalent to "before" ORR) revealed mostly unchanged size and spatial distribution for the clusters deposited at a high impact energy (LD-HIE and HD-HIE, i.e. stronger adherence to the substrate). Interestingly, in the LD-LIE sample, the clusters had migrated, forming characteristic groups of non-touching NCs, with a median edge-to-edge nearest neighbour distance of $\approx$1.5 nm. No concrete evidence was found for platinum loss (dissolution or detachment) or cluster coalescence in any of the samples. The lack of loss of platinum surface area, the increase in the HAADF intensity of the carbon substrate and the characteristic separation of the NCs in the groups in the LD-LIE sample indicate that the degradation of the platinum catalysts was caused by poisoning. Further evidence for this was found in the XPS spectra, which confirmed that changes in the chemical environment had occured for both the platinum and carbon in the analysed samples (LD-HIE and HD-HIE), with the alterations being more severe for the lower platinum loading.

In chapter 4, the electrodeposition of platinum onto an amorphous carbon-covered TEM grid substrate, from an acidic Pt(II) solution and in an inert atmosphere, was investigated using a new methodology in which a series of "hops" of the SECCM probe was employed to perform the potentiostatic deposition of Pt at different potentials in sequence. The resulting ensemble of "footprints" was located and characterised utilising aberration-corrected HAADF-STEM. Information about droplet-substrate contact area, particle size and spatial distribution, and NP morphology was obtained employing the full range of magnifications of the microscope. It was found that the *I-t* transients recorded during deposition had non-classical shapes, indicating that the platinum active surface area started to decrease after a time at high overpotentials. STEM images revealed the coexistence of single atoms, small clusters, and larger particles. Analysis of the morphologies of the Pt deposits as a function of size revealed that NCs with $\lesssim$2 nm tended to be amorphous, clusters from *ca*. 2 to 4 nm monocrystalline, and larger particles polycrystalline. A statistical analysis of the particle size distribution was carried out for $E_{app} \leq -0.6$ V. The resulting histograms presented bimodal size distributions, with a sharper peak for small species ($d \leq 2$ nm or $\approx$200 constituent atoms) and a broader one for larger sizes. The evidence obtained in this work is in good agreement with a mechanism in which growth occurs initially by direct incorporation of atoms into small clusters, up to a certain size. At $\approx$2 nm, there is a transition in the clusters' morphology from amorphous to structured, and a self-limiting growth mechanism becomes dominant. After this size, further growth must proceed by the aggregation of particles. Growth is facilitated at higher overpotentials (more negative E_{app}), resulting in a narrower size distribution.

In conclusion, the new methodologies utilised in this work have been successfully employed to obtain new insights into the degradation processes that occur for carbon/platinum catalyst systems under high mass transport rate conditions, and into the atomic scale mechanisms of the nucleation and growth of platinum during potentiostatic electrodeposition.

Correlative SECCM/STEM has been demonstrated as a powerful tool to gain new knowledge about the structure-function relationship of NPs at the nano and atomic scales.

The work presented in this thesis can be considered as a starting point from which to expand the study of a variety of metal NP systems. The combination of SECCM and HAADF-STEM, on bare TEM grids or using samples with pre-deposited size-selected clusters, is ideal for the investigation of electrocatalytic activity of arrays of highly dispersed nanoclusters, with controlled particle densities and narrow size distribution. Electrodeposition studies can be carried out employing a hopping programme, allowing several experiments to be run on the same TEM grid. Time and potentials can easily be varied with such a methodology.

Future work employing correlative SECCM and STEM studies could explore different combinations of TEM grid materials and mesh sizes, and both bigger and smaller SECCM tips. For example, different substrates could be employed, which might help overcome some of the difficulties encountered during this work, mentioned above. A smaller working electrode area would make it easier and faster to analyse the entire droplet area at higher magnifications. The main challenge in this case would be locating the areas where the electrochemical experiments were carried out for *ex situ* imaging. TEM grids with smaller mesh sizes might be useful for such experiments. Smaller mesh pitch sizes in TEM grids could also be helpful in locating areas where SECCM experiments do not lead to obvious alterations to the substrate or deposited particles.

References

[1] R.L. Rudnick and S. Gao. “Composition of the Continental Crust”. In: *Treatise on Geochemistry*. Elsevier, 2003, pp. 1–64. DOI: 10.1016/B0-08-043751-6/03016-4.

[2] Johnson Matthey. “Pgm Market Report May 2019”. In: (2019), p. 56.

[3] Haigang Dong et al. “Recovery of platinum group metals from spent catalysts: A review”. In: *International Journal of Mineral Processing* 145 (Dec. 10, 2015), pp. 108–113. DOI: 10.1016/j.minpro.2015.06.009.

[4] Gavin M. Mudd, Simon M. Jowitt, and Timothy T. Werner. “Global platinum group element resources, reserves and mining – A critical assessment”. In: *Science of The Total Environment* 622-623 (May 1, 2018), pp. 614–625. DOI: 10.1016/j.scitotenv.2017.11.350.

[5] Pramod Thakur. “Diesel Exhaust Control”. In: *Advanced Mine Ventilation*. Elsevier, 2019, pp. 157–187. DOI: 10.1016/B978-0-08-100457-9.00011-0.

[6] Chang Hwan Kim et al. “Strontium-Doped Perovskites Rival Platinum Catalysts for Treating NOx in Simulated Diesel Exhaust”. In: *Science* 327.5973 (Mar. 26, 2010), pp. 1624–1627. DOI: 10.1126/science.1184087.

[7] Michael Faraday. “X. The Bakerian Lecture. —Experimental relations of gold (and other metals) to light”. In: *Philosophical Transactions of the Royal Society of London* 147 (Jan. 1857), pp. 145–181. DOI: 10.1098/rstl.1857.0011.

[8] Puru Jena. “Beyond the Periodic Table of Elements: The Role of Superatoms”. In: *The Journal of Physical Chemistry Letters* 4.9 (May 2, 2013), pp. 1432–1442. DOI: 10.1021/jz400156t.

[9] Francesca Baletto and Riccardo Ferrando. “Structural properties of nanoclusters: Energetic, thermodynamic, and kinetic effects”. In: *Reviews of Modern Physics* 77.1 (May 24, 2005), pp. 371–423. DOI: 10.1103/RevModPhys.77.371.

[10] Roy L. Johnston. “Chapter 1 - Metal Nanoparticles and Nanoalloys”. In: *Frontiers of Nanoscience*. Ed. by Roy L. Johnston and J. P. Wilcoxon. Vol. 3. Metal Nanoparticles and Nanoalloys. Elsevier, Jan. 1, 2012, pp. 1–42. DOI: 10.1016/B978-0-08-096357-0.00006-6.

[11] D. Zanchet et al. “Inter-atomic distance contraction in thiol-passivated gold nanoparticles”. In: *Chemical Physics Letters* 323.1 (June 9, 2000), pp. 167–172. DOI: 10.1016/S0009-2614(00)00424-3.

[12] Chang Q. Sun et al. “Bond-order bond-length bond-strength (bond-OLS) correlation mechanism for the shape-and-size dependence of a nanosolid”. In: *Journal of Physics: Condensed Matter* 14.34 (Aug. 2002), pp. 7781–7795. DOI: 10.1088/0953-8984/14/34/301.

[13] Ph. Buffat and J-P. Borel. “Size effect on the melting temperature of gold particles”. In: *Physical Review A* 13.6 (June 1, 1976), pp. 2287–2298. DOI: 10.1103/PhysRevA.13.2287.

[14] Joshua Jortner. “Cluster size effects”. In: *Zeitschrift für Physik D Atoms, Molecules and Clusters* 24.3 (Sept. 1, 1992), pp. 247–275. DOI: 10.1007/BF01425749.

[15] Alexandre A. Shvartsburg and Martin F. Jarrold. “Solid Clusters above the Bulk Melting Point”. In: *Physical Review Letters* 85.12 (Sept. 18, 2000), pp. 2530–2532. DOI: 10.1103/PhysRevLett.85.2530.

[16] Stephan Link and Mostafa A. El-Sayed. “Spectral Properties and Relaxation Dynamics of Surface Plasmon Electronic Oscillations in Gold and Silver Nanodots and Nanorods”. In: *The Journal of Physical Chemistry B* 103.40 (Oct. 1, 1999), pp. 8410–8426. DOI: 10.1021/jp9917648.

[17] Masatake Haruta. “When Gold Is Not Noble: Catalysis by Nanoparticles”. In: *The Chemical Record* 3.2 (2003), pp. 75–87. DOI: 10.1002/tcr.10053.

[18] Marc T. Koper. “Structure sensitivity and nanoscale effects in electrocatalysis”. In: *Nanoscale* 3.5 (2011), pp. 2054–2073. DOI: 10.1039/C0NR00857E.

[19] Man-Bo Li et al. “Cu^{2+} induced formation of $Au_{44}(SC_2H_4Ph)_{32}$ and its high catalytic activity for the reduction of 4-nitrophenol at low temperature”. In: *Chem. Commun.* 51.21 (2015), pp. 4433–4436. DOI: 10.1039/C4CC08830A.

[20] Shubo Tian et al. “Structural isomerism in gold nanoparticles revealed by X-ray crystallography”. In: *Nature Communications* 6.1 (Oct. 20, 2015), pp. 1–7. DOI: 10.1038/ncomms9667.

[21] Stanley C. S. Lai et al. “Nucleation, aggregative growth and detachment of metal nanoparticles during electrodeposition at electrode surfaces”. In: *Chemical Science* 6.2 (2015), pp. 1126–1138. DOI: 10.1039/C4SC02792B.

[22] Michael Walter et al. “A unified view of ligand-protected gold clusters as superatom complexes”. In: *Proceedings of the National Academy of Sciences* 105.27 (2008), pp. 9157–9162. DOI: 10.1073/pnas.0801001105.

[23] T.P. Martin et al. “Observation of electronic shells and shells of atoms in large Na clusters”. In: *Chemical Physics Letters* 172.3 (Sept. 1990), pp. 209–213. DOI: 10.1016/0009-2614(90)85389-T.

[24] C. Zeng et al. “Structural patterns at all scales in a nonmetallic chiral Au133(SR)52 nanoparticle”. In: *Science Advances* 1.2 (Mar. 20, 2015), e1500045–e1500045. DOI: 10.1126/sciadv.1500045.

[25] Yasuhiro Shirasaki et al. “Emergence of colloidal quantum-dot light-emitting technologies”. In: *Nature Photonics* 7.1 (Dec. 27, 2012), pp. 13–23. DOI: 10.1038/nphoton.2012.328.

[26] Lioz Etgar. “Semiconductor Nanocrystals as Light Harvesters in Solar Cells”. In: *Materials* 6.2 (Feb. 4, 2013), pp. 445–459. DOI: 10.3390/ma6020445.

[27] P. D. Howes, R. Chandrawati, and M. M. Stevens. “Colloidal nanoparticles as advanced biological sensors”. In: *Science* 346.6205 (Oct. 3, 2014), pp. 1247390–1247390. DOI: 10.1126/science.1247390.

[28] Yue Bing Zheng et al. “Molecular plasmonics for biology and nanomedicine”. In: *Nanomedicine* 7.5 (May 2012), pp. 751–770. DOI: 10.2217/nnm.12.30.

[29] Peng Huang et al. “Biodegradable Gold Nanovesicles with an Ultrastrong Plasmonic Coupling Effect for Photoacoustic Imaging and Photothermal Therapy”. In: *Angewandte Chemie International Edition* 52.52 (Dec. 23, 2013), pp. 13958–13964. DOI: 10.1002/anie.201308986.

[30] A. T. Bell. “The Impact of Nanoscience on Heterogeneous Catalysis”. In: *Science* 299.5613 (Mar. 14, 2003), pp. 1688–1691. DOI: 10.1126/science.1083671.

[31] Britt Hvolbaek et al. “Catalytic activity of Au nanoparticles”. In: *Nano Today* 2.4 (2007), pp. 14–18.

[32] Stephanie G. Lambie et al. “Contrasting motif preferences of platinum and gold nanoclusters between 55 and 309 atoms”. In: *Nanoscale Advances* 1.6 (2019), pp. 2416–2425. DOI: 10.1039/C9NA00122K.

[33] Vijay Kumar and Yoshiyuki Kawazoe. “Evolution of atomic and electronic structure of Pt clusters: Planar, layered, pyramidal, cage, cubic, and octahedral growth”. In: *Physical Review B* 77.20 (May 13, 2008), p. 205418. DOI: 10.1103/PhysRevB.77.205418.

[34] Mufan Li et al. “Single-atom tailoring of platinum nanocatalysts for high-performance multifunctional electrocatalysis”. In: *Nature Catalysis* 2.6 (June 2019), pp. 495–503. DOI: 10.1038/s41929-019-0279-6.

[35] S. Taylor et al. “The Effect of Platinum Loading and Surface Morphology on Oxygen Reduction Activity”. In: *Electrocatalysis* 7.4 (July 1, 2016), pp. 287–296. DOI: 10.1007/s12678-016-0304-3.

[36] Emiliana Fabbri et al. “The Effect of Platinum Nanoparticle Distribution on Oxygen Electroreduction Activity and Selectivity”. In: *ChemCatChem* 6.5 (May 1, 2014). Publisher: John Wiley & Sons, Ltd, pp. 1410–1418. DOI: 10.1002/cctc.201300987.

[37] Samina Akbar et al. “Platinum as an electrocatalyst: effect of morphological aspects of Pt/Pt-based materials”. In: *Materials Science and Technology* 35.1 (Jan. 2, 2019), pp. 1–11. DOI: 10.1080/02670836.2018.1495878.

[38] J.-M. Léger. “Mechanistic aspects of methanol oxidation on platinum-based electrocatalysts”. In: *Journal of Applied Electrochemistry* 31.7 (July 1, 2001), pp. 767–771. DOI: 10.1023/A:1017531225171.

[39] Oliver T. Holton and Joseph W. Stevenson. “The Role of Platinum in Proton Exchange Membrane Fuel Cells”. In: *Platinum Metals Review* 57.4 (Oct. 1, 2013), pp. 259–271. DOI: 10.1595/147106713X671222.

[40] Matthias Arenz et al. “The Effect of the Particle Size on the Kinetics of CO Electrooxidation on High Surface Area Pt Catalysts”. In: *Journal of the American Chemical Society* 127.18 (May 1, 2005). Publisher: American Chemical Society, pp. 6819–6829. DOI: 10.1021/ja043602h.

[41] Hongzhou Yang, Sachin Kumar, and Shouzhong Zou. “Electroreduction of O2 on uniform arrays of Pt nanoparticles”. In: *Journal of Electroanalytical Chemistry*. Special Issue in Honor of Professors Chuansin Cha and Zhaowu Tian 688 (Jan. 1, 2013), pp. 180–188. DOI: 10.1016/j.jelechem.2012.08.030.

[42] Hubert A. Gasteiger and Nenad M. Marković. “Just a Dream—or Future Reality?” In: *Science* 324.5923 (Apr. 3, 2009), pp. 48–49. DOI: 10.1126/science.1172083.

[43] Frederick T. Wagner, Balasubramanian Lakshmanan, and Mark F. Mathias. “Electrochemistry and the Future of the Automobile”. In: *The Journal of Physical Chemistry Letters* 1.14 (July 15, 2010), pp. 2204–2219. DOI: 10.1021/jz100553m.

[44] Meiling Liu et al. “Nanoscale Structure Design for High-Performance Pt-Based ORR Catalysts”. In: *Advanced Materials* 31.6 (2019), p. 1802234. DOI: 10.1002/adma.201802234.

[45] Annett Rabis, Paramaconi Rodriguez, and Thomas J. Schmidt. “Electrocatalysis for Polymer Electrolyte Fuel Cells: Recent Achievements and Future Challenges”. In: *ACS Catalysis* 2.5 (May 4, 2012), pp. 864–890. DOI: 10.1021/cs3000864.

[46] L. J. Bregoli. “The influence of platinum crystallite size on the electrochemical reduction of oxygen in phosphoric acid”. In: *Electrochimica Acta* 23.6 (June 1, 1978). Publisher: Pergamon, pp. 489–492. DOI: 10.1016/0013-4686(78)85025-7.

[47] M. Peuckert et al. “Oxygen Reduction on Small Supported Platinum Particles”. In: *Journal of The Electrochemical Society* 133.5 (1986), pp. 944–947. DOI: 10.1149/1.2108769.

[48] M. L. Sattler and P. N. Ross. “The surface structure of Pt crystallites supported on carbon black”. In: *Ultramicroscopy* 20.1 (Jan. 1, 1986). Publisher: North-Holland, pp. 21–28. DOI: 10.1016/0304-3991(86)90163-4.

[49] K. Kinoshita. “Particle Size Effects for Oxygen Reduction on Highly Dispersed Platinum in Acid Electrolytes”. In: *Journal of The Electrochemical Society* 137.3 (1990), pp. 845–848. DOI: 10.1149/1.2086566.

[50] Zhenmeng Peng and Hong Yang. “Designer platinum nanoparticles: Control of shape, composition in alloy, nanostructure and electrocatalytic property”. In: *Nano Today* 4.2 (Apr. 1, 2009), pp. 143–164. DOI: 10.1016/j.nantod.2008.10.010.

[51] Minhua Shao, Amra Peles, and Krista Shoemaker. “Electrocatalysis on Platinum Nanoparticles: Particle Size Effect on Oxygen Reduction Reaction Activity”. In: *Nano Letters* 11.9 (Sept. 14, 2011), pp. 3714–3719. DOI: 10.1021/nl2017459.

[52] Zhuang Xu et al. “Effect of particle size on the activity and durability of the Pt/C electrocatalyst for proton exchange membrane fuel cells”. In: *Applied Catalysis B: Environmental* 111-112 (Jan. 2012), pp. 264–270. DOI: 10.1016/j.apcatb.2011.10.007.

[53] Francisco J. Perez-Alonso et al. “The Effect of Size on the Oxygen Electroreduction Activity of Mass-Selected Platinum Nanoparticles”. In: *Angewandte Chemie International Edition* 51.19 (2012), pp. 4641–4643. DOI: 10.1002/anie.201200586.

[54] Markus Nesselberger et al. “The effect of particle proximity on the oxygen reduction rate of size-selected platinum clusters”. In: *Nature Materials* 12.10 (Oct. 2013), pp. 919–924. DOI: 10.1038/nmat3712.

[55] A. Gamez et al. “Oxygen reduction on well-defined platinum nanoparticles inside recast ionomer”. In: *Electrochimica Acta* 41.2 (Feb. 1996), pp. 307–314. DOI: 10.1016/0013-4686(95)00305-X.

[56] K. F. Blurton et al. “The Electrochemical Activity of Dispersed Platinum”. In: *Journal of The Electrochemical Society* 119.5 (May 1, 1972). Publisher: IOP Publishing, p. 559. DOI: 10.1149/1.2404260.

[57] Wenchao Sheng et al. “Size Influence on the Oxygen Reduction Reaction Activity and Instability of Supported Pt Nanoparticles”. In: *Journal of The Electrochemical Society* 159.2 (Dec. 15, 2011). Publisher: IOP Publishing, B96. DOI: 10.1149/2.009202jes.

[58] Bernhard Schwanitz et al. “Sputtered Cathodes for Polymer Electrolyte Fuel Cells: Insights into Potentials, Challenges and Limitations”. In: *CHIMIA International Journal for Chemistry* 66.3 (Mar. 28, 2012), pp. 110–119. DOI: 10.2533/chimia.2012.110.

[59] Markus Nesselberger et al. “The Particle Size Effect on the Oxygen Reduction Reaction Activity of Pt Catalysts: Influence of Electrolyte and Relation to Single Crystal Models”. In: *Journal of the American Chemical Society* 133.43 (Nov. 2, 2011), pp. 17428–17433. DOI: 10.1021/ja207016u.

[60] K. J. J. Mayrhofer et al. “The Impact of Geometric and Surface Electronic Properties of Pt-Catalysts on the Particle Size Effect in Electrocatalysis”. In: *The Journal of Physical Chemistry B* 109.30 (Aug. 1, 2005). Publisher: American Chemical Society, pp. 14433–14440. DOI: 10.1021/jp051735z.

[61] Alok S. Tayi et al. “Supramolecular ferroelectrics”. In: *Nature Chemistry* 7.4 (Mar. 24, 2015), pp. 281–294. DOI: 10.1038/nchem.2206.

[62] Minoru Inaba et al. “Effect of Agglomeration of Pt/C Catalyst on Hydrogen Peroxide Formation”. In: *Electrochemical and Solid State Letters* 7.12 (Oct. 25, 2004). Publisher: IOP Publishing, A474. DOI: 10.1149/1.1814595.

[63] Masahiro Watanabe, Haruhiko Sei, and Paul Stonehart. “The influence of platinum crystallite size on the electroreduction of oxygen”. In: *Journal of Electroanalytical Chemistry and Interfacial Electrochemistry* 261.2 (Apr. 15, 1989), pp. 375–387. DOI: 10.1016/0022-0728(89)85006-5.

[64] Y. E. Seidel et al. “Mesoscopic mass transport effects in electrocatalytic processes”. In: *Faraday Discussions* 140.0 (2009), pp. 167–184. DOI: 10.1039/B806437G.

[65] Laure Timperman and Nicolas Alonso-Vante. “Oxide Substrate Effect Toward Electrocatalytic Enhancement of Platinum and Ruthenium–Selenium Catalysts”. In: *Electrocatalysis* 2.3 (Sept. 1, 2011), pp. 181–191. DOI: 10.1007/s12678-011-0052-3.

[66] Ifan E. L. Stephens and Ib Chorkendorff. “Minimizing the Use of Platinum in Hydrogen-Evolving Electrodes”. In: *Angewandte Chemie International Edition* 50.7 (2011), pp. 1476–1477. DOI: 10.1002/anie.201005921.

[67] Southampton Electrochemistry Group et al., eds. *Instrumental methods in electrochemistry*. Chichester: Horwood Publishing, 2001.

[68] Michael E. Hyde and Richard G. Compton. “A review of the analysis of multiple nucleation with diffusion controlled growth”. In: *Journal of Electroanalytical Chemistry* 549 (June 5, 2003), pp. 1–12. DOI: 10.1016/S0022-0728(03)00250-X.

[69] N. Tian et al. “Synthesis of Tetrahexahedral Platinum Nanocrystals with High-Index Facets and High Electro-Oxidation Activity”. In: *Science* 316.5825 (May 4, 2007), pp. 732–735. DOI: 10.1126/science.1140484.

[70] Thomas M. Day, Patrick R. Unwin, and Julie V. Macpherson. “Factors Controlling the Electrodeposition of Metal Nanoparticles on Pristine Single Walled Carbon Nanotubes”. In: *Nano Letters* 7.1 (Jan. 1, 2007), pp. 51–57. DOI: 10.1021/nl061974d.

[71] Fallyn W. Campbell and Richard G. Compton. “The use of nanoparticles in electroanalysis: an updated review”. In: *Analytical and Bioanalytical Chemistry* 396.1 (Jan. 1, 2010), pp. 241–259. DOI: 10.1007/s00216-009-3063-7.

[72] H Liu et al. “Size-selective electrodeposition of meso-scale metal particles: a general method”. In: *Electrochimica Acta* 47.5 (Dec. 3, 2001), pp. 671–677. DOI: 10.1016/S0013-4686(01)00747-2.

[73] Reginald M. Penner. “Mesoscopic Metal Particles and Wires by Electrodeposition”. In: *The Journal of Physical Chemistry B* 106.13 (Apr. 2002), pp. 3339–3353. DOI: 10.1021/jp013219o.

[74] G. Oskam et al. “Electrochemical deposition of metals onto silicon”. In: *Journal of Physics D: Applied Physics* 31.16 (Aug. 1998), pp. 1927–1949. DOI: 10.1088/0022-3727/31/16/001.

[75] R. M. Stiger et al. “Investigations of Electrochemical Silver Nanocrystal Growth on Hydrogen-Terminated Silicon(100)”. In: *Langmuir* 15.3 (Feb. 1, 1999), pp. 790–798. DOI: 10.1021/la980800b.

[76] Dennis W. Dees and Charles W. Tobias. “Mass Transfer at Gas Evolving Surfaces A Microscopic Study”. In: *Journal of The Electrochemical Society* 134.7 (Jan. 7, 1987), pp. 1702–1713. DOI: 10.1149/1.2100740.

[77] Davor P. Sutija and Charles W. Tobias. “Mass-Transport Enhancement by Rising Bubble Curtains”. In: *Journal of The Electrochemical Society* 141.10 (Jan. 10, 1994), pp. 2599–2607. DOI: 10.1149/1.2059128.

[78] Jon Ustarroz et al. “The Role of Nanocluster Aggregation, Coalescence, and Recrystallization in the Electrochemical Deposition of Platinum Nanostructures”. In: *Chemistry of Materials* 26.7 (Apr. 8, 2014), pp. 2396–2406. DOI: 10.1021/cm403178b.

[79] M. Fleischmann and H. R. Thirsk. “An investigation of electrochemical kinetics at constant overvoltage. The behaviour of the lead dioxide electrode. Part 5.—The formation of lead sulphate and the phase change to lead dioxide”. In: *Transactions of the Faraday Society* 51.0 (Jan. 1, 1955), pp. 71–95. DOI: 10.1039/TF9555100071.

[80] Benjamin Scharifker and Graham Hills. “Theoretical and experimental studies of multiple nucleation”. In: *Electrochimica Acta* 28.7 (July 1, 1983), pp. 879–889. DOI: 10.1016/0013-4686(83)85163-9.

[81] B. R. Scharifker and J. Mostany. “Three-dimensional nucleation with diffusion controlled growth: Part I. Number density of active sites and nucleation rates per site”. In: *Journal of Electroanalytical Chemistry and Interfacial Electrochemistry* 177.1 (Oct. 10, 1984), pp. 13–23. DOI: 10.1016/0022-0728(84)80207-7.

[82] Manuel Palomar-Pardavé et al. “Detailed characterization of potentiostatic current transients with 2D-2D and 2D-3D nucleation transitions”. In: *Surface Science* 399.1 (Mar. 1, 1998), pp. 80–95. DOI: 10.1016/S0039-6028(97)00813-3.

[83] H. Liu and R. M. Penner. "Size-Selective Electrodeposition of Mesoscale Metal Particles in the Uncoupled Limit". In: *The Journal of Physical Chemistry B* 104.39 (Oct. 2000), pp. 9131–9139. DOI: 10.1021/jp0017902.

[84] Jon Ustarroz et al. "A Generalized Electrochemical Aggregative Growth Mechanism". In: *Journal of the American Chemical Society* 135.31 (Aug. 7, 2013), pp. 11550–11561. DOI: 10.1021/ja402598k.

[85] Jon Ustarroz et al. "New Insights into the Early Stages of Nanoparticle Electrodeposition". In: *The Journal of Physical Chemistry C* 116.3 (Jan. 26, 2012), pp. 2322–2329. DOI: 10.1021/jp210276z.

[86] Eoin Sheridan, Johan Hjelm, and Robert J. Forster. "Electrodeposition of gold nanoparticles on fluorine-doped tin oxide: Control of particle density and size distribution". In: *Journal of Electroanalytical Chemistry* 608.1 (Sept. 15, 2007), pp. 1–7. DOI: 10.1016/j.jelechem.2006.11.015.

[87] Aleksandar Radisic et al. "Quantifying Electrochemical Nucleation and Growth of Nanoscale Clusters Using Real-Time Kinetic Data". In: *Nano Letters* 6.2 (Feb. 2006), pp. 238–242. DOI: 10.1021/nl052175i.

[88] Manoj Tripathi et al. "Controlled AFM detachments and movement of nanoparticles: gold clusters on HOPG at different temperatures". In: *Nanotechnology* 23.24 (May 2012), p. 245706. DOI: 10.1088/0957-4484/23/24/245706.

[89] Jon Ustarroz et al. "Electrodeposition of Ag nanoparticles onto carbon coated TEM grids: A direct approach to study early stages of nucleation". In: *Electrochemistry Communications* 12.12 (Dec. 2010), pp. 1706–1709. DOI: 10.1016/j.elecom.2010.10.002.

[90] Aleksandar Radisic et al. "Nucleation and Growth of Copper on TiN from Pyrophosphate Solution". In: *Journal of The Electrochemical Society* 148.1 (2001), p. C41. DOI: 10.1149/1.1344539.

[91] Milad Rezaei, Seyed Hadi Tabaian, and Davoud Fatmehsari Haghshenas. "Electrochemical nucleation of palladium on graphene: A kinetic study with an emphasis on hydrogen co-reduction". In: *Electrochimica Acta* 87 (Jan. 1, 2013), pp. 381–387. DOI: 10.1016/j.electacta.2012.09.092.

[92] F Gloaguen et al. "Platinum electrodeposition on graphite: electrochemical study and STM imaging". In: *Electrochimica Acta* 44.11 (Jan. 1, 1999), pp. 1805–1816. DOI: 10.1016/S0013-4686(98)00332-6.

[93] A. Radisic, F. M. Ross, and P. C. Searson. "In Situ Study of the Growth Kinetics of Individual Island Electrodeposition of Copper". In: *The Journal of Physical Chemistry B* 110.15 (Apr. 1, 2006). Publisher: American Chemical Society, pp. 7862–7868. DOI: 10.1021/jp057549a.

[94] A. Radisic et al. "The morphology and nucleation kinetics of copper islands during electrodeposition". In: *Surface Science* 600.9 (May 1, 2006), pp. 1817–1826. DOI: 10.1016/j.susc.2006.02.025.

[95] Yang-Rae Kim et al. "Nucleation and Aggregative Growth of Palladium Nanoparticles on Carbon Electrodes: Experiment and Kinetic Model". In: *The Journal of Physical Chemistry C* 119.30 (July 30, 2015), pp. 17389–17397. DOI: 10.1021/acs.jpcc.5b03513.

[96] Katrin Hartl et al. “Electrochemically induced nanocluster migration”. In: *Electrochimica Acta* 56.2 (Dec. 30, 2010), pp. 810–816. DOI: 10.1016/j.electacta.2010.10.005.

[97] Eirini Zagoraiou et al. “Highly dispersed platinum supported catalysts – Effect of properties on the electrocatalytic activity”. In: *Applied Catalysis B: Environmental* 259 (Dec. 15, 2019), p. 118050. DOI: 10.1016/j.apcatb.2019.118050.

[98] S. Pratontep et al. “Size-selected cluster beam source based on radio frequency magnetron plasma sputtering and gas condensation”. In: *Review of Scientific Instruments* 76.4 (2005), p. 045103. DOI: 10.1063/1.1869332.

[99] B. von Issendorff and R. E. Palmer. “A new high transmission infinite range mass selector for cluster and nanoparticle beams”. In: *Review of Scientific Instruments* 70.12 (1999), p. 4497. DOI: 10.1063/1.1150102.

[100] Richard E. Palmer and Carl Leung. “Immobilisation of proteins by atomic clusters on surfaces”. In: *Trends in Biotechnology* 25.2 (Feb. 2007), pp. 48–55. DOI: 10.1016/j.tibtech.2006.12.004.

[101] J. M. Soler et al. “Microcluster Growth: Transition from Successive Monomer Addition to Coagulation”. In: *Physical Review Letters* 49.25 (Dec. 20, 1982), pp. 1857–1860. DOI: 10.1103/PhysRevLett.49.1857.

[102] Takehiko Hihara and Kenji Sumiyama. “Formation and size control of a Ni cluster by plasma gas condensation”. In: *Journal of Applied Physics* 84.9 (Oct. 14, 1998), pp. 5270–5276. DOI: 10.1063/1.368776.

[103] Hellmut Haberland et al. “Thin films from energetic cluster impact: A feasibility study”. In: *Journal of Vacuum Science & Technology A* 10.5 (Sept. 1, 1992), pp. 3266–3271. DOI: 10.1116/1.577853.

[104] Simon R. Plant, Lu Cao, and Richard E. Palmer. “Atomic Structure Control of Size-Selected Gold Nanoclusters during Formation”. In: *Journal of the American Chemical Society* 136.21 (May 28, 2014), pp. 7559–7562. DOI: 10.1021/ja502769v.

[105] Feng Yin, Zhi Wei Wang, and Richard E. Palmer. “Controlled Formation of Mass-Selected Cu–Au Core–Shell Cluster Beams”. In: *Journal of the American Chemical Society* 133.27 (July 13, 2011), pp. 10325–10327. DOI: 10.1021/ja201218n.

[106] Carl Leung and Richard E. Palmer. “Interfacing Cluster Physics with Biology at the Nanoscale”. In: *Science and Technology of Atomic, Molecular, Condensed Matter & Biological Systems*. Vol. 1. Elsevier, 2010, pp. 517–556.

[107] H. Hartmann et al. “Design and capabilities of an experimental setup based on magnetron sputtering for formation and deposition of size-selected metal clusters on ultra-clean surfaces”. In: *Review of Scientific Instruments* 83.7 (July 1, 2012), p. 073304. DOI: 10.1063/1.4732821.

[108] S. J. Carroll et al. “Pinning of size-selected Ag clusters on graphite surfaces”. In: *The Journal of Chemical Physics* 113.18 (2000), p. 7723. DOI: 10.1063/1.1322657.

[109] S. J. Carroll et al. “Shallow Implantation of “Size-Selected” Ag Clusters into Graphite”. In: *Physical Review Letters* 84.12 (Mar. 20, 2000), pp. 2654–2657. DOI: 10.1103/PhysRevLett.84.2654.

[110] Cameron L. Bentley, Minkyung Kang, and Patrick R. Unwin. "Nanoscale Structure Dynamics within Electrocatalytic Materials". In: *Journal of the American Chemical Society* 139.46 (Nov. 22, 2017), pp. 16813–16821. DOI: 10.1021/jacs.7b09355.

[111] Cameron L. Bentley and Patrick R. Unwin. "Nanoscale electrochemical movies and synchronous topographical mapping of electrocatalytic materials". In: *Faraday Discussions* 210.0 (Oct. 9, 2018), pp. 365–379. DOI: 10.1039/C8FD00028J.

[112] Neil Ebejer et al. "Scanning Electrochemical Cell Microscopy: A Versatile Technique for Nanoscale Electrochemistry and Functional Imaging". In: *Annual Review of Analytical Chemistry* 6.1 (June 12, 2013), pp. 329–351. DOI: 10.1146/annurev-anchem-062012-092650.

[113] Cameron L. Bentley et al. "Nanoscale Electrochemical Mapping". In: *Analytical Chemistry* 91.1 (Jan. 2, 2019), pp. 84–108. DOI: 10.1021/acs.analchem.8b05235.

[114] Barak D. B. Aaronson et al. "Mapping, Measuring, and Modifying Surfaces and Interfaces at the Nanoscale". In: *Nanoelectrochemistry*. Ed. by Shigeru Amemiya and Michael V. Mirkin. Boca Raton: CRC Press, Taylor & Francis Group, 2015, pp. 655–693.

[115] Neil Ebejer et al. "Localized High Resolution Electrochemistry and Multifunctional Imaging: Scanning Electrochemical Cell Microscopy". In: *Analytical Chemistry* 82.22 (Nov. 15, 2010), pp. 9141–9145. DOI: 10.1021/ac102191u.

[116] Dmitry Momotenko et al. "High-Speed Electrochemical Imaging". In: *ACS Nano* 9.9 (Sept. 22, 2015), pp. 8942–8952. DOI: 10.1021/acsnano.5b02792.

[117] Kit T. Rodolfa et al. "Two-Component Graded Deposition of Biomolecules with a Double-Barreled Nanopipette". In: *Angewandte Chemie International Edition* 44.42 (2005), pp. 6854–6859. DOI: 10.1002/anie.200502338.

[118] Isabel M. Ornelas, Patrick R. Unwin, and Cameron L. Bentley. "High-Throughput Correlative Electrochemistry–Microscopy at a Transmission Electron Microscopy Grid Electrode". In: *Analytical Chemistry* 91.23 (Dec. 3, 2019), pp. 14854–14859. DOI: 10.1021/acs.analchem.9b04028.

[119] Cara G. Williams et al. "Scanning Micropipet Contact Method for High-Resolution Imaging of Electrode Surface Redox Activity". In: *Analytical Chemistry* 81.7 (Apr. 2009), pp. 2486–2495. DOI: 10.1021/ac802114r.

[120] Michael E. Snowden et al. "Scanning Electrochemical Cell Microscopy: Theory and Experiment for Quantitative High Resolution Spatially-Resolved Voltammetry and Simultaneous Ion-Conductance Measurements". In: *Analytical Chemistry* 84.5 (Mar. 6, 2012), pp. 2483–2491. DOI: 10.1021/ac203195h.

[121] Cameron L. Bentley, Minkyung Kang, and Patrick R. Unwin. "Scanning electrochemical cell microscopy: New perspectives on electrode processes in action". In: *Current Opinion in Electrochemistry* 6.1 (Dec. 1, 2017), pp. 23–30. DOI: 10.1016/j.coelec.2017.06.011.

[122] Minkyung Kang et al. "Frontiers in Nanoscale Electrochemical Imaging: Faster, Multifunctional, and Ultrasensitive". In: *Langmuir* 32.32 (Aug. 16, 2016), pp. 7993–8008. DOI: 10.1021/acs.langmuir.6b01932.

[123] Jon Ustarroz et al. “Mobility and Poisoning of Mass-Selected Platinum Nanoclusters during the Oxygen Reduction Reaction”. In: *ACS Catalysis* 8.8 (Aug. 3, 2018), pp. 6775–6790. DOI: 10.1021/acscatal.8b00553.

[124] A. V. Crewe, J. Wall, and J. Langmore. “Visibility of Single Atoms”. In: *Science* 168.3937 (June 12, 1970), pp. 1338–1340. DOI: 10.1126/science.168.3937.1338.

[125] S. J. Pennycook et al. “Scanning transmission electron microscopy for nanostructure characterization”. In: *Scanning Microscopy for Nanotechnology*. Springer, 2007, pp. 152–191.

[126] M. Varela et al. “Materials characterization in the aberration-corrected scanning transmission electron microscope”. In: *Annual Review of Materials Research* 35.1 (Aug. 4, 2005), pp. 539–569. DOI: 10.1146/annurev.matsci.35.102103.090513.

[127] David B. Williams and C. Barry Carter. *Transmission electron microscopy: a textbook for materials science*. 2. ed. New York: Springer, 2009. 760 pp.

[128] P. E. Batson, N. Dellby, and O. L. Krivanek. “Sub-ångstrom resolution using aberration corrected electron optics”. In: *Nature* 418.6898 (Aug. 8, 2002), pp. 617–620. DOI: 10.1038/nature00972.

[129] Max Haider et al. “A spherical-aberration-corrected 200kV transmission electron microscope”. In: *Ultramicroscopy* 75.1 (Oct. 1998), pp. 53–60. DOI: 10.1016/S0304-3991(98)00048-5.

[130] Z. Y. Li et al. “Three-dimensional atomic-scale structure of size-selected gold nanoclusters”. In: *Nature* 451.7174 (Jan. 3, 2008), pp. 46–48. DOI: 10.1038/nature06470.

[131] Z W Wang and R E Palmer. “Intensity calibration and atomic imaging of size-selected Au and Pd clusters in aberration-corrected HAADF-STEM”. In: *Journal of Physics: Conference Series* 371 (July 2, 2012), p. 012010. DOI: 10.1088/1742-6596/371/1/012010.

[132] *Gatan Microscopy Suite Software*.

[133] Johannes Schindelin et al. “Fiji: an open-source platform for biological-image analysis”. In: *Nature Methods* 9.7 (July 2012), pp. 676–682. DOI: 10.1038/nmeth.2019.

[134] Ioannis Katsounaros et al. “Oxygen Electrochemistry as a Cornerstone for Sustainable Energy Conversion”. In: *Angewandte Chemie International Edition* 53.1 (2014), pp. 102–121. DOI: 10.1002/anie.201306588.

[135] J. K. Nørskov et al. “Origin of the Overpotential for Oxygen Reduction at a Fuel-Cell Cathode”. In: *The Journal of Physical Chemistry B* 108.46 (Nov. 2004), pp. 17886–17892. DOI: 10.1021/jp047349j.

[136] Minhua Shao et al. “Recent Advances in Electrocatalysts for Oxygen Reduction Reaction”. In: *Chemical Reviews* 116.6 (Mar. 23, 2016), pp. 3594–3657. DOI: 10.1021/acs.chemrev.5b00462.

[137] Chang-Hui Chen et al. “High resolution mapping of oxygen reduction reaction kinetics at polycrystalline platinum electrodes”. In: *Physical Chemistry Chemical Physics* 16.34 (July 8, 2014), p. 18545. DOI: 10.1039/C4CP01511H.

[138] A. M. Gómez-Marín, Rubén Rizo, and Juan M. Feliu. “Oxygen reduction reaction at Pt single crystals: a critical overview”. In: *Catalysis Science & Technology* 4.6 (2014), pp. 1685–1698. DOI: 10.1039/C3CY01049J.

[139] Josef C Meier et al. “Design criteria for stable Pt/C fuel cell catalysts”. In: *Beilstein Journal of Nanotechnology* 5 (Jan. 16, 2014), pp. 44–67. DOI: 10.3762/bjnano.5.5.

[140] Hemma Mistry et al. “Tuning Catalytic Selectivity at the Mesoscale via Interparticle Interactions”. In: *ACS Catalysis* 6.2 (Feb. 5, 2016), pp. 1075–1080. DOI: 10.1021/acscatal.5b02202.

[141] Chang Hyuck Choi et al. “Tuning selectivity of electrochemical reactions by atomically dispersed platinum catalyst”. In: *Nature Communications* 7.1 (Apr. 2016). DOI: 10.1038/ncomms10922.

[142] Shengli Chen and Anthony Kucernak. “Electrocatalysis under Conditions of High Mass Transport Rate: Oxygen Reduction on Single Submicrometer-Sized Pt Particles Supported on Carbon”. In: *The Journal of Physical Chemistry B* 108.10 (Mar. 1, 2004), pp. 3262–3276. DOI: 10.1021/jp036831j.

[143] Xi Lin et al. “Effect of Particle Size on the Adsorption of O and S Atoms on Pt: A Density-Functional Theory Study”. In: *The Journal of Physical Chemistry B* 105.32 (Aug. 1, 2001), pp. 7739–7747. DOI: 10.1021/jp011133p.

[144] Pablo S. Fernández et al. “Platinum nanoparticles produced by EG/PVP method: The effect of cleaning on the electro-oxidation of glycerol”. In: *Electrochimica Acta* 98 (May 30, 2013), pp. 25–31. DOI: 10.1016/j.electacta.2013.02.129.

[145] Christopher M. Zalitis, Denis Kramer, and Anthony R. Kucernak. “Electrocatalytic performance of fuel cell reactions at low catalyst loading and high mass transport”. In: *Physical Chemistry Chemical Physics* 15.12 (2013), pp. 4329–4340. DOI: 10.1039/C3CP44431G.

[146] Nenad M. Markovic, Hubert A. Gasteiger, and Philip N. Ross. “Oxygen Reduction on Platinum Low-Index Single-Crystal Surfaces in Sulfuric Acid Solution: Rotating Ring-Pt(hkl) Disk Studies”. In: *The Journal of Physical Chemistry* 99.11 (Mar. 1, 1995), pp. 3411–3415. DOI: 10.1021/j100011a001.

[147] U. A. Paulus et al. “Oxygen reduction on a high-surface area Pt/Vulcan carbon catalyst: a thin-film rotating ring-disk electrode study”. In: *Journal of Electroanalytical Chemistry* 495.2 (Jan. 5, 2001), pp. 134–145. DOI: 10.1016/S0022-0728(00)00407-1.

[148] Akiyoshi Kuzume, Enrique Herrero, and Juan M. Feliu. “Oxygen reduction on stepped platinum surfaces in acidic media”. In: *Journal of Electroanalytical Chemistry*. Special Issue In Honour of David Schiffrin 599.2 (Jan. 15, 2007), pp. 333–343. DOI: 10.1016/j.jelechem.2006.05.006.

[149] Ana M. Gómez-Marín and Juan M. Feliu. “New Insights into the Oxygen Reduction Reaction Mechanism on Pt (111): A Detailed Electrochemical Study”. In: *ChemSusChem* 6.6 (2013), pp. 1091–1100. DOI: 10.1002/cssc.201200847.

[150] Ana M. Gómez–Marín and Juan M. Feliu. “Role of oxygen-containing species at Pt(111) on the oxygen reduction reaction in acid media”. In: *Journal of Solid State Electrochemistry* 19.9 (Sept. 1, 2015), pp. 2831–2841. DOI: 10.1007/s10008-015-2850-7.

[151] Mohammad J. Eslamibidgoli and Michael H. Eikerling. “Electrochemical Formation of Reactive Oxygen Species at Pt (111)-A Density Functional Theory Study”. In: *ACS Catalysis* 5.10 (Oct. 2, 2015), pp. 6090–6098. DOI: 10.1021/acscatal.5b01154.

[152] A. M. Gómez-Marín et al. “Interaction of hydrogen peroxide with a Pt(111) electrode”. In: *Electrochemistry Communications* 22 (Aug. 1, 2012), pp. 153–156. DOI: 10.1016/j.elecom.2012.06.016.

[153] Laetitia Dubau et al. “A review of PEM fuel cell durability: materials degradation, local heterogeneities of aging and possible mitigation strategies”. In: *WIREs Energy and Environment* 3.6 (2014), pp. 540–560. DOI: 10.1002/wene.113.

[154] Matthias Arenz and Alessandro Zana. “Fuel cell catalyst degradation: Identical location electron microscopy and related methods”. In: *Nano Energy* 29 (Nov. 2016), pp. 299–313. DOI: 10.1016/j.nanoen.2016.04.027.

[155] Josef C Meier et al. “Stability investigations of electrocatalysts on the nanoscale”. In: *Energy & Environmental Science* 5.11 (2012), pp. 9319–9330. DOI: 10.1039/C2EE22550F.

[156] Shengsheng Zhang et al. “A review of platinum-based catalyst layer degradation in proton exchange membrane fuel cells”. In: *Journal of Power Sources* 194.2 (Dec. 1, 2009), pp. 588–600. DOI: 10.1016/j.jpowsour.2009.06.073.

[157] Sebastian Proch et al. “Strong Effects of Cluster Size and Air Exposure on Oxygen Reduction and Carbon Oxidation Electrocatalysis by Size-Selected Ptn (n <= 11) on Glassy Carbon Electrodes”. In: *Journal of the American Chemical Society* 135.8 (Feb. 27, 2013), pp. 3073–3086. DOI: 10.1021/ja309868z.

[158] Chih-Cheng Hung et al. “Corrosion of carbon support for PEM fuel cells by electrochemical quartz crystal microbalance”. In: *Journal of Power Sources* 196.1 (Jan. 1, 2011), pp. 140–146. DOI: 10.1016/j.jpowsour.2010.07.015.

[159] K. H. Kangasniemi, D. A. Condit, and T. D. Jarvi. “Characterization of Vulcan Electrochemically Oxidized under Simulated PEM Fuel Cell Conditions”. In: *Journal of The Electrochemical Society* 151.4 (Jan. 4, 2004), E125–E132. DOI: 10.1149/1.1649756.

[160] J. Willsau and J. Heitbaum. “The influence of Pt-activation on the corrosion of carbon in gas diffusion electrodes—A dems study”. In: *Journal of Electroanalytical Chemistry and Interfacial Electrochemistry* 161.1 (Feb. 1984), pp. 93–101. DOI: 10.1016/S0022-0728(84)80252-1.

[161] Wei Li and Alan M. Lane. “Investigation of Pt catalytic effects on carbon support corrosion of the cathode catalyst in PEM fuel cells using DEMS spectra”. In: *Electrochemistry Communications* 11.6 (June 1, 2009), pp. 1187–1190. DOI: 10.1016/j.elecom.2009.04.001.

[162] Tomasz Rapecki et al. “Activity changes of glassy carbon electrodes caused by their exposure to OH• radicals”. In: *Electrochemistry Communications* 12.11 (Nov. 1, 2010), pp. 1531–1534. DOI: 10.1016/j.elecom.2010.08.026.

[163] S. Maass et al. “Carbon support oxidation in PEM fuel cell cathodes”. In: *Journal of Power Sources*. Selected Papers presented at the10th ULM ElectroChemical Days 176.2 (Feb. 1, 2008), pp. 444–451. DOI: 10.1016/j.jpowsour.2007.08.053.

[164] Mei Cai et al. “Investigation of thermal and electrochemical degradation of fuel cell catalysts”. In: *Journal of Power Sources*. Special issue including selected papers presented at the International Workshop on Molten Carbonate Fuel Cells and Related Science and Technology 2005 together with regular papers 160.2 (Oct. 6, 2006), pp. 977–986. DOI: 10.1016/j.jpowsour.2006.03.033.

[165] Zhangquan Peng et al. “Direct Detection of the Superoxide Anion as a Stable Intermediate in the Electroreduction of Oxygen in a Non-Aqueous Electrolyte Containing Phenol as a Proton Source”. In: *Angewandte Chemie International Edition* 54.28 (2015), pp. 8165–8168. DOI: 10.1002/anie.201502039.

[166] Xiao Li and Andrew A. Gewirth. “Oxygen Electroreduction through a Superoxide Intermediate on Bi-Modified Au Surfaces”. In: *Journal of the American Chemical Society* 127.14 (Apr. 1, 2005), pp. 5252–5260. DOI: 10.1021/ja043170a.

[167] Min-hua Shao, Ping Liu, and Radoslav R. Adzic. “Superoxide Anion is the Intermediate in the Oxygen Reduction Reaction on Platinum Electrodes”. In: *Journal of the American Chemical Society* 128.23 (June 1, 2006), pp. 7408–7409. DOI: 10.1021/ja061246s.

[168] Cunzhong Zhang, Fu-Ren F. Fan, and Allen J. Bard. “Electrochemistry of Oxygen in Concentrated NaOH Solutions: Solubility, Diffusion Coefficients, and Superoxide Formation”. In: *Journal of the American Chemical Society* 131.1 (Jan. 14, 2009), pp. 177–181. DOI: 10.1021/ja8064254.

[169] Nobuaki Ohguri, Atsuko Y. Nosaka, and Yoshio Nosaka. “Detection of OH radicals as the effect of Pt particles in the membrane of polymer electrolyte fuel cells”. In: *Journal of Power Sources* 195.15 (Aug. 1, 2010), pp. 4647–4652. DOI: 10.1016/j.jpowsour.2010.02.010.

[170] Jean-Marc Noël et al. “Evidence for OH Radical Production during Electrocatalysis of Oxygen Reduction on Pt Surfaces: Consequences and Application”. In: *Journal of the American Chemical Society* 134.5 (Feb. 8, 2012), pp. 2835–2841. DOI: 10.1021/ja211663t.

[171] Jean-Marc Noël, Yun Yu, and Michael V. Mirkin. “Dissolution of Pt at Moderately Negative Potentials during Oxygen Reduction in Water and Organic Media”. In: *Langmuir* 29.5 (Feb. 5, 2013), pp. 1346–1350. DOI: 10.1021/la304694d.

[172] M. H. Shao and R. R. Adzic. “Spectroscopic Identification of the Reaction Intermediates in Oxygen Reduction on Gold in Alkaline Solutions”. In: *The Journal of Physical Chemistry B* 109.35 (Sept. 1, 2005), pp. 16563–16566. DOI: 10.1021/jp053450s.

[173] Alexander Panchenko et al. “In-situ spin trap electron paramagnetic resonance study of fuel cell processes”. In: *Physical Chemistry Chemical Physics* 6.11 (2004), pp. 2891–2894. DOI: 10.1039/B404253K.

[174] M. Zatoń, J. Rozière, and D. J. Jones. “Current understanding of chemical degradation mechanisms of perfluorosulfonic acid membranes and their mitigation strategies: a review”. In: *Sustainable Energy & Fuels* 1.3 (2017), pp. 409–438. DOI: 10.1039/C7SE00038C.

[175] Stephen J. Percival, Jeffrey E. Dick, and Allen J. Bard. “Cathodically Dissolved Platinum Resulting from the O2 and H2O2 Reduction Reactions on Platinum Ultramicroelectrodes”. In: *Analytical Chemistry* 89.5 (Mar. 7, 2017), pp. 3087–3092. DOI: 10.1021/acs.analchem.6b04832.

[176] Valentín Briega-Martos, Enrique Herrero, and Juan M. Feliu. "Effect of pH and Water Structure on the Oxygen Reduction Reaction on platinum electrodes". In: *Electrochimica Acta* 241 (July 1, 2017), pp. 497–509. DOI: 10.1016/j.electacta.2017.04.162.

[177] R. Alayan et al. "Organization of size-selected platinum and indium clusters soft-landed on surfaces". In: *Physical Review B* 76.7 (Aug. 17, 2007), p. 075424. DOI: 10.1103/PhysRevB.76.075424.

[178] D. Tainoff et al. "Self-Organization of Size-Selected Bare Platinum Nanoclusters: Toward Ultra-dense Catalytic Systems". In: *The Journal of Physical Chemistry C* 112.17 (May 1, 2008), pp. 6842–6849. DOI: 10.1021/jp710216s.

[179] L. Bardotti et al. "Mass-selected clusters deposited on graphite: Spontaneous organization controlled by cluster surface reaction". In: *Physical Review B* 83.3 (Jan. 24, 2011), p. 035425. DOI: 10.1103/PhysRevB.83.035425.

[180] W. Ding et al. "Mechanics of hydrogenated amorphous carbon deposits from electron-beam-induced deposition of a paraffin precursor". In: *Journal of Applied Physics* 98.1 (July 1, 2005), p. 014905. DOI: 10.1063/1.1940138.

[181] A. J. V. Griffiths and T. Walther. "Quantification of carbon contamination under electron beam irradiation in a scanning transmission electron microscope and its suppression by plasma cleaning". In: *Journal of Physics: Conference Series* 241 (July 2010), p. 012017. DOI: 10.1088/1742-6596/241/1/012017.

[182] C. R Parkinson, M Walker, and C. F McConville. "Reaction of atomic oxygen with a Pt(111) surface: chemical and structural determination using XPS, CAICISS and LEED". In: *Surface Science* 545.1 (Nov. 1, 2003), pp. 19–33. DOI: 10.1016/j.susc.2003.08.029.

[183] Yihua Liu et al. "Self-Terminating Growth of Platinum Films by Electrochemical Deposition". In: *Science* 338.6112 (Dec. 7, 2012), pp. 1327–1330. DOI: 10.1126/science.1228925.

[184] Xu Zhao, Hang Ren, and Long Luo. "Gas Bubbles in Electrochemical Gas Evolution Reactions". In: *Langmuir* 35.16 (Apr. 23, 2019), pp. 5392–5408. DOI: 10.1021/acs.langmuir.9b00119.

[185] Yufei Wang, Emma Gordon, and Hang Ren. "Mapping the Nucleation of H2 Bubbles on Polycrystalline Pt via Scanning Electrochemical Cell Microscopy". In: *The Journal of Physical Chemistry Letters* 10.14 (July 18, 2019), pp. 3887–3892. DOI: 10.1021/acs.jpclett.9b01414.

[186] Haytham E. M. Hussein et al. "Tracking Metal Electrodeposition Dynamics from Nucleation and Growth of a Single Atom to a Crystalline Nanoparticle". In: *ACS Nano* 12.7 (July 24, 2018), pp. 7388–7396. DOI: 10.1021/acsnano.8b04089.

[187] D.R.G. Mitchell. "Contamination mitigation strategies for scanning transmission electron microscopy". In: *Micron* 73 (June 2015), pp. 36–46. DOI: 10.1016/j.micron.2015.03.013.

[188] *Support Film Grids, Substrate Grids for Electron Microscopy*. URL: https://www.tedpella.com/Support_Films_html/Support_Films_and_Substrates_Overview.htm (visited on 09/04/2020).

[189] *Download Agar Scientific Catalogue No.8*. URL: https://www.agarscientific.com/catalogue-download (visited on 09/04/2020).

Appendix A

Additional Figures for Chapter 3

A.1 Cumulative Nearest Neighbour Distance Histogram for the LD Samples

Cumulative NND histograms for the LD samples. Discussion of these results can be found in section 3.5.

A.1.1 Low Density, High Impact Energy Sample

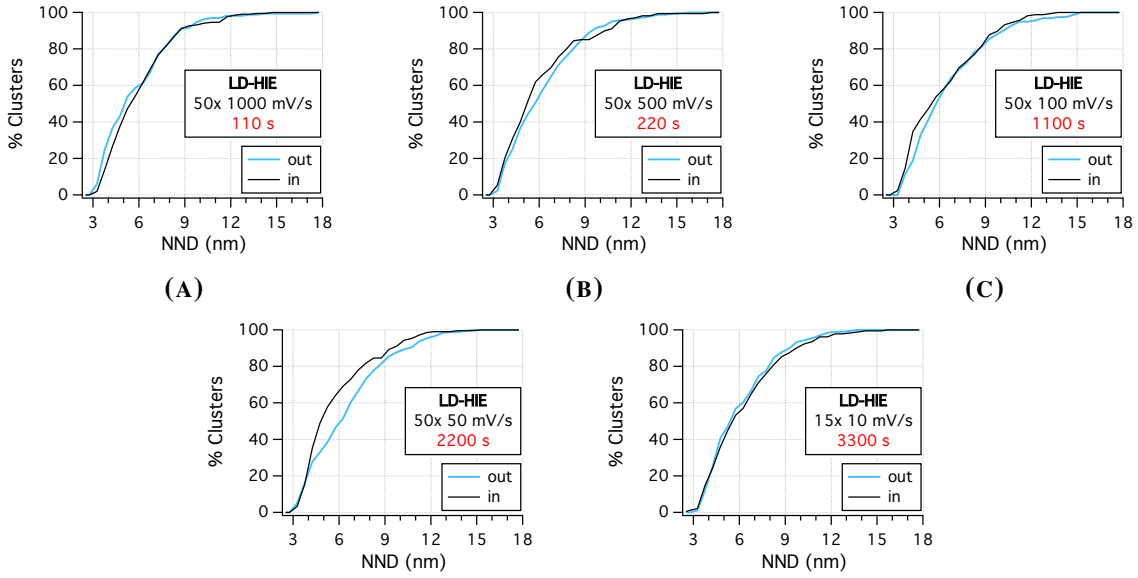

FIGURE A.1: Nearest neighbour distance (NND) cumulative histograms for the LD-HIE sample for areas where ORR was executed ("inside") and in neighbouring, pristine areas ("outside"). Experimental conditions are given inside each graph.

A.1.2 Low Density, Low Impact Energy Sample

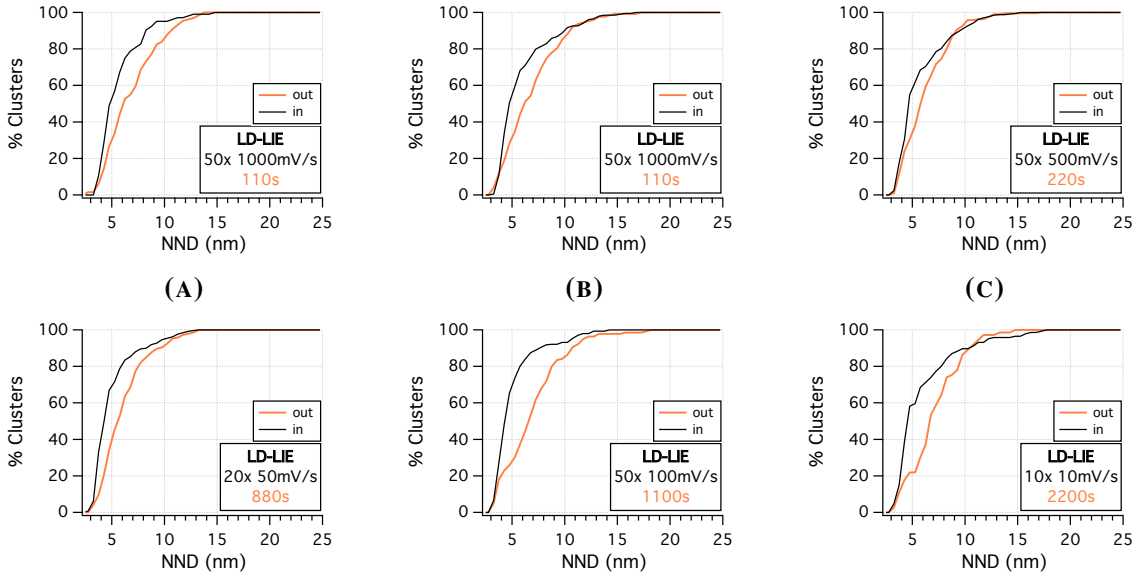

FIGURE A.2: Nearest neighbour distance (NND) cumulative histograms for the LD-LIE sample for areas where ORR was executed ("inside") and in neighbouring, pristine areas ("outside"). Experimental conditions are given inside each graph.

A.2 XPS Spectra

A.2.1 Pt 4f Spectra

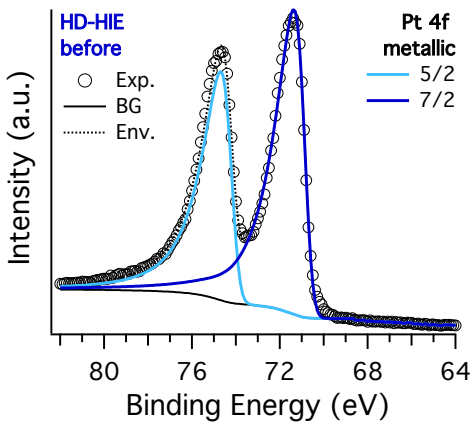

(A) HD-HIE before.

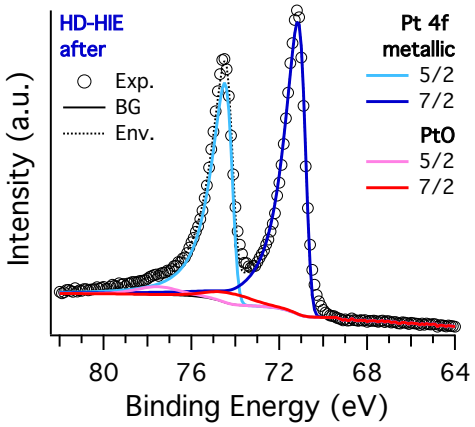

(B) HD-HIE after.

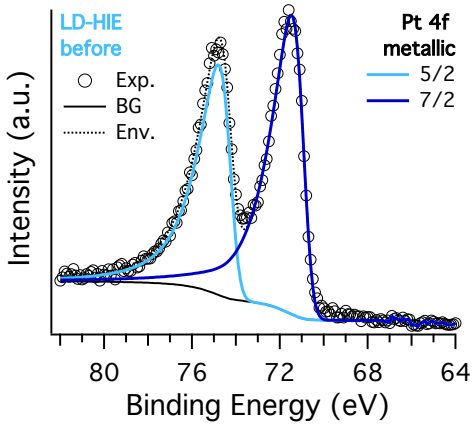

(C) LD-HIE before.

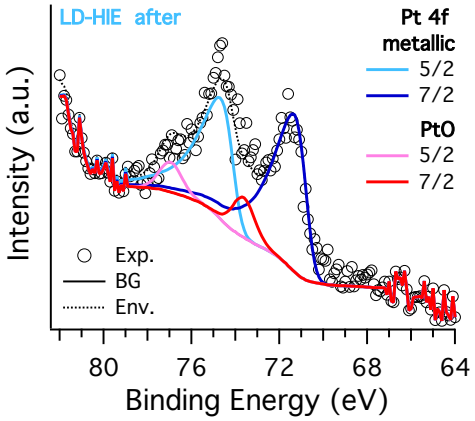

(D) LD-HIE after.

FIGURE A.3: XPS spectra of the Pt 4f peaks for **(A)-(B)** a HD-HIE and **(C)-(D)** a LD-HIE sample. **(A)** and **(C)** were obtained before, and **(B)** and **(D)** after 200 CVs at 0.2 V s^{-1} between $E = 0$ V and 1.1 V. Exp, BG and Env indicate the experimental curve, background and envelope, respectively.

A.2.2 Carbon 1s Spectra

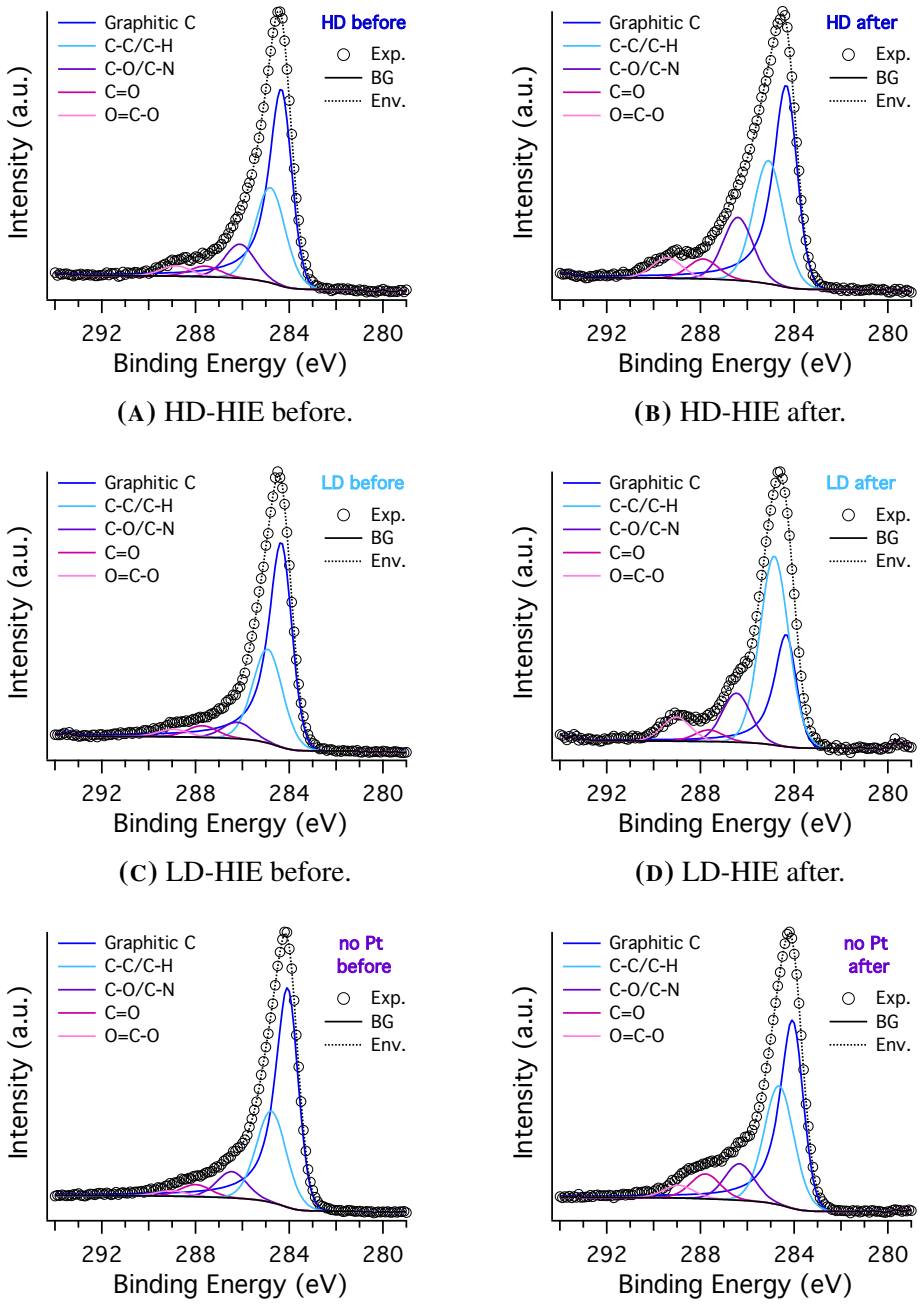

(A) HD-HIE before.

(B) HD-HIE after.

(C) LD-HIE before.

(D) LD-HIE after.

(E) No Pt before.

(F) Np Pt after.

FIGURE A.4: XPS spectra of the C 1s peak for **(A)-(B)** a HD-HIE sample, **(C)-(D)** a LD-HIE sample, and **(E)-(F)** a bare TEM grid (no platinum). **(A)**, **(C)** and **(E)** were obtained before, and **(B)**, **(D)** and **(F)** after 200 CVs at 0.2 V s^{-1} between $E = 0$ V and 1.1 V. Exp, BG and Env indicate the experimental curve, background and envelope, respectively.